MAGNETO–OPTICAL STUDIES OF STRONGLY CORRELATED MATERIALS

A DISSERTATION
SUBMITTED TO THE DEPARTMENT OF PHYSICS
AND THE COMMITTEE ON GRADUATE STUDIES
OF STANFORD UNIVERSITY
IN PARTIAL FULFILLMENT OF THE REQUIREMENTS
FOR THE DEGREE OF
DOCTOR OF PHILOSOPHY

David Saykin
July 2026

I certify that I have read this dissertation and that, in my opinion, it is fully adequate in scope and quality as a dissertation for the degree of Doctor of Philosophy.

(Aharon Kapitulnik) Principal Adviser

I certify that I have read this dissertation and that, in my opinion, it is fully adequate in scope and quality as a dissertation for the degree of Doctor of Philosophy.

(Ian Fisher)

I certify that I have read this dissertation and that, in my opinion, it is fully adequate in scope and quality as a dissertation for the degree of Doctor of Philosophy.

(Steven Kivelson)

Approved for the Stanford University Committee on Graduate Studies

Abstract

This thesis presents a series of magneto–optical investigations into strongly correlated quantum materials, focusing on the emergence of unconventional orders and their interplay with electronic structure. The magneto–optical Kerr effect (MOKE), implemented via a cryogenic Sagnac interferometer, serves as the primary probe, enabling the detection of time–reversal symmetry-breaking (TRSB) phenomena with state-of-the-art precision.

The first part of the work examines infinite–layer nickelate superconductors, a newly discovered class of high–temperature superconductors closely related to cuprates. We report the observation of a spin–glass state that onsets well above the superconducting transition temperature. This finding provides unambiguous evidence of a disordered magnetic phase embedded within the superconducting state, shedding light on the role of magnetic frustration in nickelates.

The second part addresses the ongoing debate over time–reversal symmetry breaking in the kagome charge–ordered superconductor CsV_3Sb_5. Using high–sensitivity MOKE at multiple wavelengths, we compile and analyze an extensive dataset obtained over several years. While the collective body of experimental evidence remains contradictory, our measurements enable us to present well–reasoned arguments against the presence of time–reversal symmetry breaking in this material.

By combining high–precision magneto–optical measurements with careful material–specific analysis, this work advances our understanding of how complex electronic orders emerge and coexist in strongly correlated systems. It highlights the unique power of MOKE as a probe of subtle broken symmetries.

Acknowledgments

This thesis is dedicated to everyone who spent time with me during my 6-year-long stay at Stanford University. I've really enjoyed spending nights in the lab, running as many measurements as possible before I run out of liquid helium, tinkering with optical and electronic instruments in hopes of slightly improving the signal-to-noise ratio, and engaging in full-hearted debates during the group meeting. I equally enjoyed playing volleyball with fellow Stanford students at a highly competitive level, perfecting the art of crashing free-food events with lab mates, and throwing social gatherings for the Russian-speaking student association.

I would like to thank my advisor, Aharon, for believing in me and providing me with the opportunity to prove to everyone that I can become a genuine scientist. When I first arrived at Stanford, I considered myself a theoretical physicist, but upon seeing the opportunity to learn the art of experimentation, I decided to switch gears and become an experimental physicist. Most professors I have spoken to were not eager to hire someone who doesn't even know how to solder, so it was a challenge to find a group in my position. Luckily, I found Aharon, who, being open-minded, offered to join his KGB group. Throughout my PhD, Aharon's office door was always open to me, both physically and metaphorically. He was never too busy to answer my questions, and gladly spent hours teaching me the basics of condensed matter physics: from how to use cigarette paper to glue the sample to the cold finger with good thermal anchoring but without an electrical short, to how to understand the intricacies of unconventional superconductivity.

I would like to thank my group members for creating a friendly and productive atmosphere in the lab. Without you, my PhD journey would have been much more complicated and less exciting. Thank you, Sejoon, for teaching me how to operate a cryostat. Thank you, DiDi, for showing me how to analyze data. Thank you, Erik, for showing me how to navigate the lab space. Thank you, Victor, for teaching me how instruments operate. Thank you, Tiffany, for showing me how to use the machines in the cleanroom. Thank you, Alan, for sharing your limitless knowledge with me about every instrument in the lab. Thank you, Eylon, for taking the time to help me debug my clumsy wiring mistakes. Thank you, Qianni, for working tirelessly to grow and characterize samples and then measure them together with me while teaching me about novel physical concepts. Thank you, Winslow, for taking the time to discuss how the Sagnac interferometer works with me. Thank

you, Jinze, for always knowing what to say to light up the room. Thank you, Isaiah, for your active management of the lab.

At the Stanford physics department, scientific interactions are not at all limited to our own lab. There is a spirit of camaraderie shared between all the groups, as if we're all working together on one big project. All professors are very friendly and are always willing to initiate inter-laboratory projects. Prof. Steven Kivelson never fails to come up with a quick-witted reply to any physics question I have and beyond. Prof. Ian Fisher is always happy to share his passion and motivation, energizing me with his exciting ideas. Prof. David Goldhaber-Gordon is always ready to carefully listen and share an incredibly thoughtful response to any question I have about physics, academia, or life in general. Prof. Ben Feldman, Harold Hwang, Sri Raghu, Marty Fejer, Robert Laughlin, Xiaoliang Qi, and David Schuster have always been ready to chat about any physics and non-physics related topics. I genuinely appreciate the opportunity to learn from distinguished Stanford faculty members throughout my PhD.

Probably, most of what I enjoyed was collaborating with students and postdoctoral researchers from other labs at Stanford and around the globe, as it was during these collaborations that I gained a new perspective on my own research and came to understand what is essential in the scientific community. I would like to thank the Feldman group members for teaching me about the intricacies of two-dimensional materials: Ben Foutty, Yifan Li, Yuwen Hu, Jesse Hoke, and Jinwoo Kim. I would like to thank Hwang group members for being my first experience working in the lab: Bai Wang, Shannon Harvey, Martin Gonzalez, Florian Theuss, Minyong Han, Jennifer Fowlie, and Varun Harbola. I would like to thank Fisher lab members for always being happy to lend a helping hand: Matthias Ikeda, Kaan Alp Yay, and Benito Gonzalez. I would like to thank Goldhaber-Gordon lab members for teaching me how to use a wire bonder: Aaron Sharpe, Steven Tran, Chaitrali Duse, and Joe Finney. I would like to thank Kent lab members for having so many fun lunch breaks filled with dark humor together: Jyotirmai Singh, Aya Keller, Maria Simanovskaia, Nicholas Rapidis, and Ameya Kunder. I would like to thank Andy Kent and Koral Aykin for teaching me about spintronics.

I would like to thank my dear friends with whom I spent so much time together playing volleyball, going on road trips, and celebrating holidays together: Artem Pashchinski, Anton Lykov, Daniil Eskoskin, Savelii Kholin, Sergey Klevtsov, Natalia Antonova, Maria Konakova, Mirella Vassilev, Tamra Nebabu, Viktor Krapivin, Stanislav Cherepanov, Pavel Nosov, Alina Tokmakova, Nikita Sopenko, Andrew Grekov, Alexander Avdoshkin, Pavel Kurilovich, Vlad Kurilovich, Daniil Antonenko, Anastasiia Sharipova, Viktoriia Baibakova, Artem Danielov, Elizaveta Tremsina, Vasily Tremsin, Petr Martynov, Vitaly Abdrashitov, Masha Gorshkova, Valeriia Pegushina, Julia Markel, Rishi Bommasani, Akshat Pandey, Aviv Simchony, Anastasiia Masaltseva, Alexander Frenkel, Rushana Galeeva, Gulia Ismagilova, Vasily Kruzhilin, Daniel Kharitonov, Anna Kalygina, Dan Ilyin, Artur Avkhadiev, Jim Dukhonvy, Nikolay Buravsky, Ekaterina Bogdanova, Dima Torba, David Gogokhiya, Kfir Dolev,

Caleb Koch, Maria Damian, Saranesh Prembabu, Timur Garipov, Hlib Razumkov, Vika Shautsova, Igor Molybog, Boris Sobolev, Dime Skvortsov, Daniil Matveev, Eugene Kegeles, Masha Karelina, Anastasia Koloskova, Vladimir Selivanov, Fedor Popov, Vlad Kozii, Manchen Hu, Artem Denisov. Without your friendship, my PhD journey would have been a much duller experience. Without a doubt, I am forgetting many important names, but I hope that you know how much I value our relationship, even though I forgot to mention you here!

I would like to especially thank my friend Vadim Khudyakov for always being happy to chat with me over Zoom and for providing help understanding physics when I need it the most.

I would like to thank my past research advisers, Konstantin Tikhonov and Igor Burmistrov, for teaching me to conduct science the right way. I would also like to thank many friends and teachers from the Moscow Institute of Physics and Technology, Skoltech, and the Landau Institute, for their contributions to shaping me into who I am today.

Last but not least, I would like to thank my parents, Rustam and Alfiia, for providing for and caring for me. I always feel like I can rely on you. I love you.

How to read this thesis

This thesis unfolds across six chapters, each contributing a distinct thread to the broader narrative. For the reader who seeks the essence of the work without venturing into the intricate terrain of theoretical derivations or the delicate machinery of the experimental setup, I recommend focusing on the *Introduction* and *Conclusions*.

Chapter 1, *Introduction*, raises the curtain on the stage where this scientific story takes place. Here, the central themes are introduced, the key players are cast, and the reader is offered a first taste of the questions, tensions, and discoveries that will shape the chapters to come.

Chapter 6, *Conclusions*, gathers the threads of the narrative into a concise yet complete tapestry. It distills years of research into their essential findings, leaving the reader with a clear view of what has been learned, what mysteries remain, and where the path may lead next.

Chapter 2 is intentionally pedagogical in nature, serving as a foundation for everything that follows. Here, I lay out the essential principles needed to develop an intuitive and rigorous way of thinking about magneto–optical probes and the interaction between light and matter. The ideas themselves are deceptively simple — yet, curiously, they have been the source of many spirited debates whenever I have presented my work. This only reinforced my conviction that it is worth assembling all the pieces clearly and deliberately before leading the reader into the complexities of the primary data, even if that means revisiting concepts that might seem elementary at first glance.

This chapter is designed as a compact but comprehensive reference for students embarking on the study of magneto–optical phenomena, bringing together in one place the theoretical tools they will need. It will also be valuable for any reader who has ever puzzled over how the microscopic electronic properties of a material leave their signature in the measured changes of light's polarization upon reflection, and who wishes to explore the more profound logic linking the two.

Chapter 3, *Sagnac interferometer*, offers an in–depth exploration of the principal instrument that underpinned my research—the Sagnac interferometer. While much of the system's foundation is not new, having been refined and employed for years by many students before me [1, 2, 3, 4, 5], this chapter approaches it with a fresh perspective. I revisit well–established concepts through the lens of my own experience, offering new strategies for extracting richer information from the device and proposing practical upgrades that expand its capabilities.

Beyond serving as a technical manual, this chapter is intended as both a guide and an inspiration for those who wish to construct a similar system themselves—or even design an entirely different probe using the same principles. By unpacking the key ideas behind the Sagnac interferometer's design and illustrating its remarkable versatility, the chapter aims to engage not only the builder seeking step–by–step insight but also the engineering–minded condensed–matter physicist who enjoys seeing elegant instrumentation pushed to its limits.

Chapters 4 and 5 form the heart of this thesis, containing its principal discoveries and most significant scientific contributions. Each chapter follows a parallel structure—Introduction, Results, and Discussion—allowing the reader to navigate according to interest. Those wishing first to grasp the overarching narrative may choose to skip the technicality-heavy 'results' section on the first read.

Chapter 4, *Spin–glass in nickelate superconductors*, begins with a gentle introduction to the concept of spin–glass state, and then briefly discusses most of the known studies of magnetism in nickelate superconductors to date. The magneto–optical Kerr effect measurements presented here constitute one of the two principal findings of this thesis. Our data provide compelling, irrefutable evidence for the existence of a spin–glass state in nickelate superconductors – remarkably, one that emerges at temperatures higher than the superconducting transition temperature and persists in coexistence with it. We further explore how the properties of this state depend on fabrication conditions, focusing in particular on the role of substrate engineering. The chapter concludes with a discussion of the broader implications of these findings for understanding the electronic structure and emergent order in infinite–layer nickelate superconductors.

Chapter 5, *Mystery of* CsV_3Sb_5, addresses a question that has stirred intense debate in the community: does the charge–density wave (CDW) order in this material spontaneously break time–reversal symmetry (TRS)? Here, we gather and synthesize all relevant experimental evidence, presenting it through the lens of this central question. The Kerr effect measurements reported in this chapter are the culmination of years of meticulous work, informed by countless discussions at conferences with many of the world's leading condensed–matter physicists, and represent the second principal finding of this thesis. While the existing body of data remains contradictory enough to resist a definitive verdict, we offer a carefully reasoned assessment of the evidence on both sides. We conclude the chapter by sharing our perspective on the most plausible resolution of this puzzle.

Contents

List of Tables

List of Figures

Chapter 1

Introduction

1.1 Strongly correlated materials

Strongly correlated materials are solids in which electron–electron interactions are so strong that they qualitatively reshape the electronic ground state and low-energy excitations. In weakly interacting metals, single-particle band theory and Landau's Fermi-liquid picture work remarkably well [6]. By contrast, in correlated systems, interactions lead to a cascade of unconventional ordered states: charge order, nematicity, topological magnetism, and superconductivity [7].

Interaction strength

Naively, one could characterize how strong interactions between electrons are by comparing the average kinetic energy of electron quasiparticles and the Coulomb electron energy. In atomic units where distance is measured in Bohr's radii $a_B^* = \hbar^2 \varepsilon_{\text{eff}} / m^* e^2$, and the energy unit is the Rydberg constant $\text{Ry}^* = e^2 / \varepsilon_{\text{eff}} a_B^*$, the ratio between potential and kinetic energy follows from typical inter-electron spacing.

$$\hat{H} = \sum_i \frac{\hat{p}_i^2}{2m^*} + \sum_{i \neq j} \frac{e^2}{2\varepsilon_{\text{eff}}} \frac{1}{|\mathbf{R}_i - \mathbf{R}_j|} = \frac{\text{Ry}^*}{2} \cdot \left[\sum_i \left(\frac{\partial}{\partial \mathbf{r}} \right)^2 + \sum_{i \neq j} \frac{1}{|\mathbf{r}_i - \mathbf{r}_j|} \right]$$

Typical (dimensionless) distance between electrons r_s can be estimated from carrier density as

$$r_s \sim \frac{1}{a_B^* n^{1/d}},$$

This parameter is sometimes called the dimensionless Wigner-Seitz radius, and it doubles as a parameter describing interaction strength since

$$\frac{U_{\text{potential}}}{E_{\text{kinetic}}} \simeq r_s \simeq \frac{e^2}{\hbar}\frac{m^*}{\varepsilon_{\text{eff}} n^{1/d}}.$$

We see that we would expect correlation to be strong in heavy–fermion $m^* \gg m_e$ or in low–carrier density $n \ll a_B^{-d}$ electronic systems; conversely, screening of Coulomb interaction $\varepsilon_{\text{eff}} \gg 1$ would lead to non–interacting Fermi gas–like behavior.

Plugging the numbers for typical metals such as aluminum and copper, we find a Wigner-Seitz radius of order one. It might be an indication that considering Coulomb interaction as a perturbation is not legitimate; however, we know from experience that in metals, the impact of electron–electron interactions is small and mainly shortens quasiparticles' lifetime. On the other hand, there exists a special family of materials where the parameter r_s could be much larger. In parent compounds of copper oxide superconductors we have $r_s \simeq 10$, in uranium based heavy–fermion superconductors $r_s \simeq 100$, and in van der Waals nanodevices depending on position of Fermi level controlled by voltage gates interaction strength could range from $r_s \simeq 1$ to $r_s \simeq 100$.

Hubbard model

A better way to get a sense of the physics of strongly correlated materials is to model them with the Hubbard model.

$$H = -t \sum_{\langle ij\rangle,\sigma} \left(\hat{c}^\dagger_{i,\sigma}\hat{c}_{j,\sigma} + \hat{c}^\dagger_{j,\sigma}\hat{c}_{i,\sigma}\right) + U\sum_i \hat{n}_{i,\uparrow}\hat{n}_{i,\downarrow}, \qquad \hat{n}_{i,\sigma} = \hat{c}^\dagger_{i,\sigma}\hat{c}_{i,\sigma}$$

The first term describes the kinetic energy of the system, parameterized by the hopping integral t. The second term is the on-site interaction of strength U that represents the electron repulsion.

In the non-interacting case $U = 0$, the Hubbard Hamiltonian reduces to the hopping Hamiltonian and can be diagonalized in Fourier space, for example, for a square lattice. $\varepsilon_{\sigma,\mathbf{k}} = -2t\sum_i \cos k_i a$. The ground state is a Fermi gas of itinerant electrons, which is metallic at half-filling. In the opposite case $t = 0$, all sites are decoupled and electrons are localized.

At the same time, the Hubbard model is also able to describe superexchange anti-ferromagnetism. In the strong coupling limit $U \gg t$, it can be shown that the low-energy effective theory of a Hubbard Hamiltonian at half-filling is the antiferromagnetic Heisenberg model

$$H_{\text{eff}} = \frac{4t^2}{U}\sum_{\langle ij\rangle} \mathbf{S}_i \cdot \mathbf{S}_j.$$

Next, let us provide short information about typical strongly correlated systems, and build some intuition based on examples.

1.1.1 Examples of strongly correlated materials

Cuprates

Cuprate superconductors are a prototypical example of strongly correlated materials, where electron–electron interactions dominate the low-energy physics and cannot be treated as small perturbations. Their parent compounds, such as La_2CuO_4 or $Bi_2Sr_2CaCu_2O_{8+\delta}$, are Mott insulators with long-range antiferromagnetic (AFM) order despite having partially filled Cu $3d$ bands. This insulating behavior arises because the strong on-site Coulomb repulsion in the CuO_2 planes localizes electrons, preventing metallic conduction predicted by simple band theory. These correlations set the stage for a rich phase diagram when carriers are introduced via chemical doping [8, 9, 10].

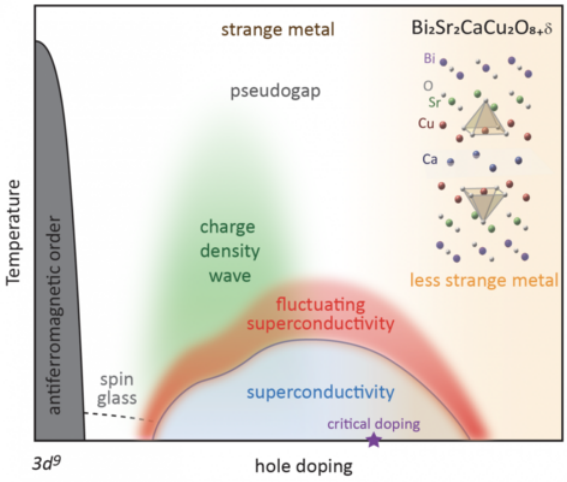

Figure 1.1: Phase diagram of BSCCO [Sobota *et al*, 2021]

The link between strong correlations and high-T_c superconductivity in cuprates is believed to lie in the magnetic exchange interactions inherited from the parent AFM phase. The superexchange interaction between neighboring Cu spins provides an effective attractive mechanism for electrons. This magnetic 'glue' enables unconventional pairing without the need for phonon-mediated interactions, allowing cuprates to reach T_c values far above those of conventional BCS superconductors.

Flat-band van der Waals materials

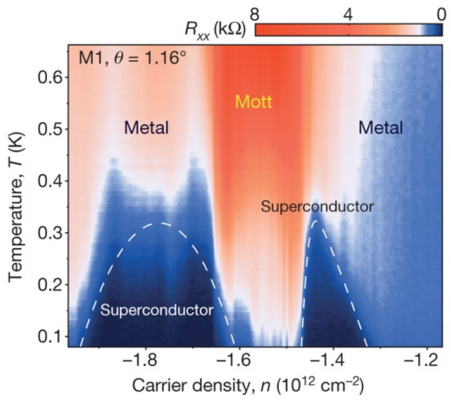

Figure 1.2: Phase diagram of MATBG [Cao *et al*, 2018]

Another famous example of strongly correlated systems is van der Waals (vdW) nanodevices: artificial heterostructures assembled from atomically thin crystals, such as graphene, hexagonal boron nitride (hBN), and transition metal dichalcogenides, stacked together using the weak interlayer van der Waals force.

Among the most striking examples of strongly correlated electronic behavior in such systems is magic-angle twisted bilayer graphene (MATBG) — two sheets of monolayer graphene stacked with a small relative "magic" twist angle of about 1.1°. At

the magic angle, moiré interference between the two layers' lattices produces a large-scale superlattice, which dramatically modifies the electronic band structure. In particular, the lowest-energy moiré bands become nearly flat, quenching the kinetic energy of electrons and enhancing the role of Coulomb interactions. This is analogous to the Mott insulating behavior of cuprates; however, in MATBG, the underlying mechanism is the band flattening from moiré superlattice effects rather than from narrow d-orbitals.

As a result, MATBG exhibits a rich set of correlation-driven phases: correlated insulators at certain fractional fillings and superconductivity at other filling factors, which can be swiftly controlled continuously via gate voltages, allowing for the traversal of the entire phase diagram in a single device without chemical doping [11, 12].

Heavy-fermion superconductors

Heavy-fermion unconventional superconductors are among the most striking examples of how strong electron–electron correlations can reshape the very notion of a quasiparticle. In Cerium and Uranium-based superconductors, conduction electrons hybridize with localized f-electron moments, producing a narrow band near the Fermi level with an effective mass m^* that can be hundreds of times the free electron mass m_e [13]. For example, effective electron masses in UPt_3 were estimated to be $100 - 200$ times larger than the bare electron mass using upper critical fields [14], far infrared absorptivity [15], and quantum oscillation studies [16, 17].

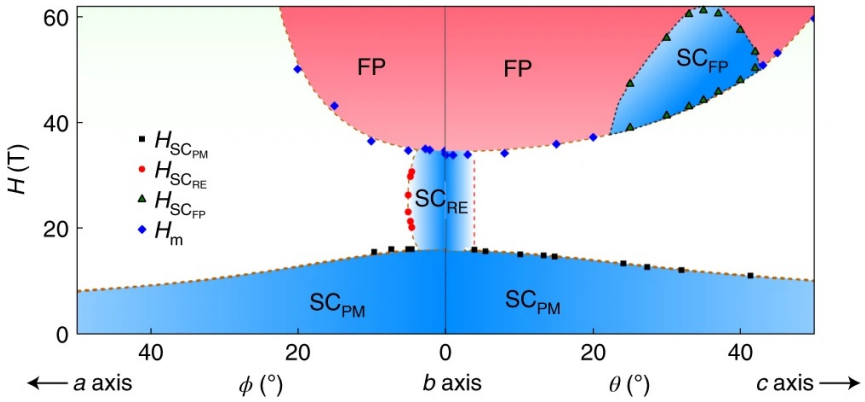

Figure 1.3: Re-entrant superconductivity in UTe_2 [Ran *et al*, 2019]

The interplay between magnetism and superconductivity is particularly rich in heavy-fermion systems. In UPt_3, superconductivity coexists with weak antiferromagnetic order, and the multiple superconducting phases in its temperature–field phase diagram reflect a highly anisotropic, possibly odd-parity pairing state.

UTe_2 offers a different twist: it is believed to host spin-triplet superconductivity and exhibits re-entrant superconductivity [18]: destroyed by moderate magnetic fields, the superconducting state

unexpectedly reappears at higher fields, possibly stabilized by field-induced magnetic fluctuations or changes in the Fermi surface topology.

Similar to copper-oxide high-T_c superconductors, these systems show that magnetism is not always an enemy of superconductivity; it can be its accomplice.

Iron–based superconductors

In iron-based superconductors (FeSCs), electronic correlations are "orbital-selective" rather than Mott-localizing, so magnetism, nematicity, and superconductivity are tightly intertwined and are believed to coexist in the vicinity of a quantum critical point. For example, in Co-doped $BaFe_2As_2$, electron doping suppresses the spin-density wave (SDW) and the nematic orders, producing a superconducting dome with a broad interplay regime between SDW and superconductivity [19]. The fluctuations near such a critical point are thought to play a key role in boosting superconductivity, making these materials prime examples of how strong electronic correlations can drive rich and tunable quantum phenomena.

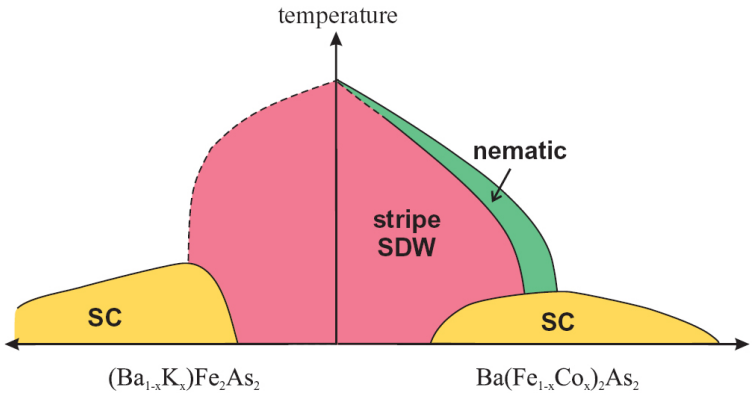

Figure 1.4: Phase diagram of $BaFe_2As_2$ [Fernandes *et al*, 2017]

1.1.2 Discussions

Across seemingly disparate families of unconventional superconductors—cuprates, magic-angle twisted bilayer graphene, heavy-fermion compounds, and iron-based materials — a unifying theme emerges: strong electronic correlations give rise to rich phase diagrams where superconductivity coexists and competes with other collective states. Magnetism, charge order, and nematicity often intertwine with the superconducting order, suggesting that these phenomena share a common microscopic origin.

Next, we describe in more detail two systems studied in the present thesis and show how they share many of the hallmarks of strongly correlated materials and provide insights into the physics of the interplay between different quantum orders.

1.2 Infinite-layer nickelate superconductors

The discovery of a novel family of superconductors $R_{1-x}Sr_xNiO_2$ (R = La, Nd, Pr) by Li *et al* in 2019 [20] was a significant milestone in the quest to understand unconventional superconductivity beyond the cuprates. Infinite-layer nickelates are in the same $P4/mmm$ structure as the prototypical parent cuprate $CaCuO_2$, and Ni^{1+} atoms have the same $3d^9$ electronic configuration as Cu^{2+} (see e.g. Ref. [21] for a review).

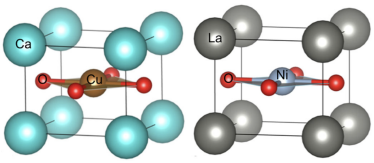

Figure 1.5: Crystal structure of (prototypical) $CaCuO_2$ and $LaNiO_2$ [Botana *et al*, 2020]

Like the cuprates, nickelates possess quasi-two-dimensional NiO_2 planes with a dominant $d_{x^2-y^2}$ orbital character at the Fermi level (see Fig. 1.5). Both families show unconventional superconductivity emerging upon hole doping, and similar to spin-fluctuations present in cuprates, there is evidence for long-range AFM fluctuations in nickelates revealed by RIXS and NMR studies [22, 23].

While the magnetic structure of infinite-layer nickelate superconductors is yet to be fully understood, particularly as it affects superconductivity, its most salient features are the absence of long-range AFM ordering and the freezing of spins into a glass phase even in the parent compound [24, 25, 26]. In the cuprates, magnetism originates from copper spins in the CuO_2 planes, which is also the starting point for models of the SG state [27]. By contrast, glassy dynamics observed in polycrystalline $LaNiO_2$ samples were attributed to the presence of subtle local oxygen disorder in the form of remaining apical oxygen [24].

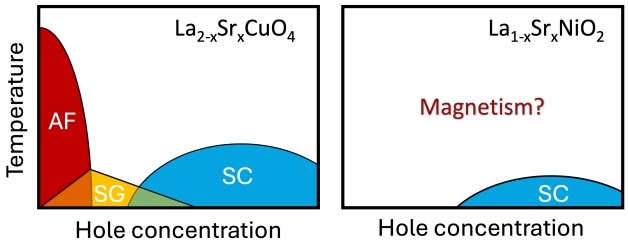

Figure 1.6: Magnetic state of nickelates remains largely unexplored

Because superconductivity has so far only been detected in thin-film nickelates [28], their associated magnetic states have not yet been established. A comprehensive muon spin-relaxation (μSR) study of $R_{1-x}Sr_xNiO_2$ by Fowlie *et al* [29] discovered intrinsic magnetism, which gradually onsets in the 100-150 K temperature range across the rare earth (R) series, and coexists with superconductivity. These authors speculated that the observed glassy magnetic phase is intrinsic in nature and reflects the AFM coupling between the Ni^+ spins. On the other hand, scanning superconducting quantum interference device (SQUID) microscopy has picked up an inhomogeneous ferromagnetic background in $La_{0.85}Sr_{0.15}NiO_2$ slightly above the superconducting temperature, which has been attributed to extrinsic NiO_x particles on the interface between the nickelate and the $SrTiO_3$ capping layer [30].

Ultimately, comparing nickelates and cuprates side by side sharpens our understanding of how strong correlations, magnetism, and band structure conspire to produce high-T_c superconductivity.

1.3 Charge–order in kagome superconductor CsV_3Sb_5

Recently discovered kagomé metal families AV_3Sb_5 (A = Cs, Rb, K) [31] and ScV_6Sn_6 [32] have attracted significant attention due to their intriguing electronic properties stemming from a kagomé lattice structure. In CsV_3Sb_5 the charge-density wave (CDW) state emerges below approximately T_{CDW} = 94 K, characterized by a lattice reconstruction within the vanadium plane [33]. The sister compound ScV_6Sn_6 exhibits a CDW state below T_{CDW} = 92 K, associated primarily with the modulation of Sn atoms along the c–axis. Notably, superconductivity has been observed in CsV_3Sb_5 below 3 K, further intertwining with its CDW order and adding complexity to its electronic phases. For comprehensive reviews on these materials and their associated electronic phenomena, we refer the reader to Ref. [34].

The CDW state in AV_3Sb_5 kagomé metals is theoretically predicted to exhibit a chiral flux phase, characterized by loop currents that break time-reversal symmetry (TRS) [35, 36, 37]. Such chiral flux phases represent an intriguing state of matter, potentially hosting exotic transport and optical responses due to nontrivial electronic topology and orbital magnetism.

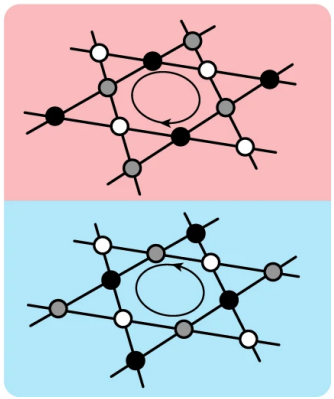

Figure 1.7: Orbital currents in chiral flux state [Guo *et al*, 2022]

Experimental evidence regarding time-reversal symmetry breaking (TRSB) in AV_3Sb_5 (A = Cs, Rb, K) metals has been controversial. Initial scanning tunneling microscopy (STM) studies reported chirality switching of CDW peaks under high applied magnetic field, indicative of a TRS-broken chiral state [38, 39, 40]. However, subsequent STM studies of CsV_3Sb_5 with spin-polarized tips found no evidence of chirality switching or local magnetic moments [41], challenging earlier interpretations. Similarly, an independent STM study of KV_3Sb_5 reported the absence of sensitivity of CDW peaks to magnetic field [42]. Still, at the same time, a recent report on RbV_3Sb_5 has confirmed the possibility of chirality flipping with the sign of the magnetic field [43].

Muon spin relaxation (μSR) experiments have also provided conflicting results. Studies of CsV_3Sb_5 observed enhanced internal magnetic fields below the CDW transition [44, 45] and interpreted it as evidence of TRSB. Similar μSR evidence for hidden magnetism was reported in ScV_6Sn_6 [46]. At the same time, μSR experiments on KV_3Sb_5 [47] attribute observed changes in relaxation rates at the CDW transition to nuclear rather than electronic fields, thus concluding that no evidence of TRSB is present.

Transport measurements have revealed an appearance of non-linear-in-H behavior below the CDW transition in CsV_3Sb_5 and related compounds, which was interpreted as a precursor to anomalous Hall effect indicative of spontaneous orbital magnetism [48, 49, 50, 51]. However, recent detailed studies of CsV_3Sb_5 propose an alternative explanation: these apparent anomalies could arise from

high-mobility low-density Fermi pockets opening below T_{CDW} and specific Fermi surface reconstructions rather than intrinsic TRSB phenomena [52, 53].

Magneto-optical Kerr effect (MOKE) experiments have provided some of the most contentious and intriguing results regarding TRSB. Initially large Kerr rotations ($\sim$ 1 mrad) concurrent with the CDW onset were reported, interpreted as strong evidence of TRSB [54, 55]. Contradicting these claims, Saykin *et al* found no observable spontaneous Kerr rotation within the 30 nrad noise floor over the $d = 10$ μm beam spot size [56]. Furthermore, Farhang *et al* demonstrated that the large optical rotations of linearly polarized light are isotropic and independent of magnetic fields, thus unrelated to TRSB [57].

In this work, we present comprehensive MOKE measurements on CsV_3Sb_5 and ScV_6Sn_6 at two wavelengths, 830 nm and 1550 nm. We report no observable spontaneous magnetization in either material at both wavelengths. Notably, Kerr susceptibility changes induced by the CDW transition are less sensitive at 830 nm compared to 1550 nm. Additionally, uniaxial strain of magnitude $\pm 0.1\%$ does not cause spontaneous Kerr signals in CsV_3Sb_5 , despite significant strain sensitivity previously reported in transport [58, 59] and STM measurements [43]. Our findings significantly constrain the potential magnitude of the orbital flux phase and challenge theoretical models that predict significant observable TRSB effects [60].

1.4 Magneto-optical probes

Optical and magneto-optical probes are potent because they directly access charge dynamics, spectral properties, and broken symmetries encoded in the optical conductivity.

By sweeping photon energy, you can isolate Berry-curvature "hot spots" tied to specific inter-band or excitonic transitions, and separate orbital from spin contributions — all information a DC Hall measurement integrates away. In the THz limit, Kerr rotations connect cleanly to the Hall conductance (enabling magneto-optical readout of QAH states). At the same time, in the visible/near-IR they highlight band- and exciton-selective responses, thereby probing quantum geometry beyond transport.

Pump–probe magneto-optics (TR-MOKE / TR-Faraday) resolves spin dynamics from femtoseconds to microseconds. A short "pump" perturbs the spin/electronic system—via ultrafast demagnetization, photo-doping, transient anisotropy, or the inverse Faraday effect—while a time-delayed, weak probe tracks Kerr/Faraday rotation. From the sub-100 fs drop and ps recovery, one can extract electron–spin–lattice coupling; from damped oscillations, one gets coherent paramagnon frequencies, g-factors, anisotropy fields, and lifetimes.

Imaging modes turn these dynamics and hysteresis into maps. Wide-field Kerr microscopy (including cryogenic, confocal implementations for 2D materials) records pixel-resolved data so one can

extract spatial distributions of coercive field, remanence, nucleation/propagation paths, and defect-controlled switching — all without contacts. Scanning variants push to diffraction-limited spots; near-field MOKE can reach 100 nm spot size, resolving moiré or granular textures.

Compared with transport, magneto-optics uniquely provides (i) spectral resolution — how σ_{xy} and circular dichroism evolve with frequency; (ii) ultrafast dynamics — pump and probe method; (iii) spatial resolution – scan over the sample surface; (iv) contact-free compatibility with gated devices and suspended heterostructures.

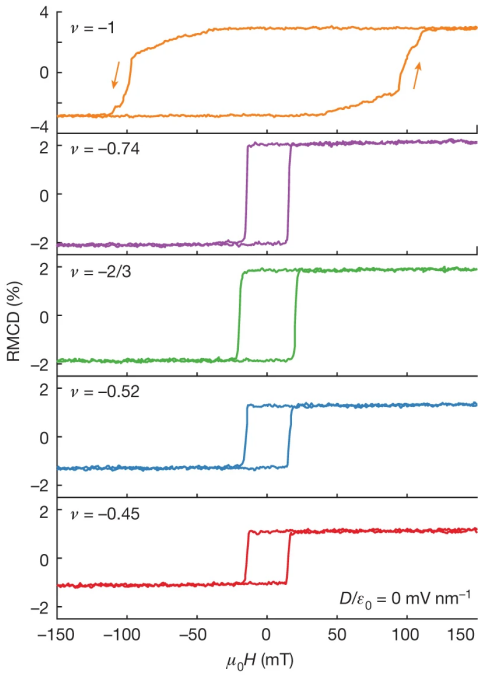

Figure 1.8: RMCD in twisted $MoTe_2$ [Cai *et al*, 2023]

A beautiful example of the successful application of a magneto-optical probe is the reflective magnetic circular dichroism (RMCD) measurement in twisted bilayer $MoTe_2$ moiré Chern insulators [61] (see Fig. 1.8). Photoluminescence (PL) was used to find resonant light frequency for different filling factors, and then circular dichroism measurements in a magnetic field were used to demonstrate the ferromagnetic nature of the electronic state at fractional filling. This demonstrated that optical probes alone can reveal topological invariants and spontaneous ferromagnetism, without relying on quantized DC Hall plateaus. Subsequent transport on the same platform observed both integer and fractional QAH, providing a cross-check. Thus, the first-ever fractional quantum anomalous Hall state was discovered.

Chapter 2

Basic notions from theory of gyrotropy

In this chapter, we review the electrodynamics concepts essential for describing the propagation of light in crystalline media. Although these topics are described in detail in textbooks [62, 63], they are generally omitted from a standard 'Electricity and Magnetism' course.

2.1 Electrodynamics of continuous media

Propagation of electromagnetic waves is described by Maxwell's equations, which for fields in vacuum are typically written as

$$\nabla \cdot \mathbf{E} = 4\pi\rho, \tag{2.1}$$

$$\nabla \cdot \mathbf{B} = 0, \tag{2.2}$$

$$\nabla \times \mathbf{E} = -\frac{1}{c}\frac{\partial}{\partial t}\mathbf{B}, \tag{2.3}$$

$$\nabla \times \mathbf{B} = \frac{1}{c}\frac{\partial}{\partial t}\mathbf{E} + \frac{4\pi}{c}\mathbf{j}. \tag{2.4}$$

In the electrodynamical problem, Gauss's laws for electricity and magnetism (2.1), (2.2) are usually considered as *initial conditions* for Faraday's and Ampere-Maxwell's laws (2.3), (2.4) since they don't govern the dynamics. Indeed, let us remember the continuity equation

$$\partial_t \rho + \nabla \cdot \mathbf{j} = 0 \tag{2.5}$$

and compute divergence of (2.3) and (2.4).

$$\nabla \times \mathbf{E} = -\frac{1}{c}\frac{\partial}{\partial t}\mathbf{B} \qquad \Rightarrow \qquad \frac{\partial}{\partial t}\nabla \cdot \mathbf{B} = 0$$
$$\nabla \times \mathbf{B} = \frac{1}{c}\frac{\partial}{\partial t}\mathbf{E} + \frac{4\pi}{c}\mathbf{j} \qquad \Rightarrow \qquad \frac{\partial}{\partial t}\left(\nabla \cdot \mathbf{E} - 4\pi\rho\right) = 0$$

We see that, up to a constant, Gauss's laws can be considered a consequence of Ampere-Maxwell's and Faraday's laws and the continuity equation.

Charge and current in equations (2.1), (2.4), (2.5) are describing *media* charges. There is typically a separation into *external* charges, which are assumed fixed, and charges bound to the media, which should be determined alongside electromagnetic vector fields[1].

$$\rho = \rho_{\text{ext}} + \rho_{\text{med}}, \qquad \mathbf{j} = \mathbf{j}_{\text{ext}} + \mathbf{j}_{\text{med}}$$

We will not introduce external charges, so we will always use ρ and $\mathbf{j}$ to denote media charges.

2.1.1 Constitutive relations at optical frequencies

When solving an electrostatic problem in dielectric media, in order to describe charges in media, it makes sense to introduce the concepts of polarization $\mathbf{P}$ and magnetization $\mathbf{M}$, defined as dipole moment and magnetic moment densities.

$$\int \mathbf{P}\, dV = \int \rho\mathbf{r}\, dV \tag{2.6}$$
$$\int \mathbf{M}\, dV = \frac{1}{2c}\int \left[\mathbf{r} \times \rho\mathbf{v}\right]\, dV \tag{2.7}$$

However, when considering *dynamics* of electromagnetic field inside a dielectric medium, such description breaks down at optical frequencies. As explained in [62, §79], if we assume that (2.6) is true, then from Ampére-Maxwell's law follows

$$\mathbf{j} = c\left[\nabla \times \mathbf{M}\right] + \partial_t \mathbf{P}$$

It can be further shown that (2.7) is only true when $\partial_t \mathbf{P} \ll c\left[\nabla \times \mathbf{M}\right]$, which is always true in electrostatics, but not so at optical frequencies.

Generally speaking, in the absence of (2.6) and (2.7), there exists an additional degree of freedom in choosing $\mathbf{P}$ and $\mathbf{M}$, akin to a gauge transformation of the electromagnetic potential $\mathbf{A}$. Indeed, charges and current in a material always satisfy the continuity equation (2.5). If we found some

[1] Sometimes fixed currents are called "free" and unknown currents are called "bound", but this terminology is confusing. This separation has nothing to do with whether electrons are itinerant or localized.

vector fields $\mathbf{P}$ and $\mathbf{M}$ that describe the media's response, i.e., such that

$$\rho = -\nabla \cdot \mathbf{P}, \qquad \mathbf{j} = \partial_t \mathbf{P} + c\,[\nabla \times \mathbf{M}] \tag{2.8}$$

then for arbitrary field $\mathbf{X}$, fields

$$\tilde{\mathbf{P}} = \mathbf{P} + [\nabla \times \mathbf{X}]\,, \qquad \tilde{\mathbf{M}} = \mathbf{M} - \frac{1}{c}\partial_t \mathbf{X}.$$

would correspond to the same distribution of charges and currents. To eliminate this ambiguity in the dynamical problem, one could demand (2.6) and then derive $\mathbf{M}$ according to (2.8). However, it turns out that in the presence of spatial dispersion [62, §103] (see also discussion in [64]), it is more convenient to instead postulate

$$\mathbf{M} = 0.$$

This convention is going to be used throughout this manuscript, i.e., we would always assume magnetic permeability to be $\mu = 1$ and $\mathbf{B} = \mathbf{H}$.

In other words, polarization vector is by definition

$$\mathbf{P}(t, \mathbf{r}) = \int_{-\infty}^{t} \mathbf{j}(t', \mathbf{r}) dt'. \tag{2.9}$$

We choose it in such form to satisfy $\mathbf{j} = \partial_t \mathbf{P}$, then from the continuity equation follows $\rho = -\nabla \cdot \mathbf{P}$. Just like we did in electrostatics, we introduce the electric displacement field vector

$$\mathbf{D} = \mathbf{E} + 4\pi \mathbf{P}. \tag{2.10}$$

This lets us rewrite Maxwell's equations in a form that contains $\mathbf{D}$ but does not have $\mathbf{j}$ or ρ.

$$\nabla \times \mathbf{E} = -\frac{1}{c}\frac{\partial}{\partial t}\mathbf{B} \qquad \nabla \cdot \mathbf{B} = 0$$
$$\nabla \times \mathbf{B} = \frac{1}{c}\frac{\partial}{\partial t}\mathbf{D} \qquad \nabla \cdot \mathbf{D} = 0$$

The first equation lets us express $\mathbf{B}$ through $\mathbf{E}$, and the second — $\mathbf{D}$ through $\mathbf{B}$; however, in order to complete this system of equations, we also need an additional relation between $\mathbf{D}$ and $\mathbf{E}$ (or equivalently $\mathbf{j}$ and $\mathbf{E}$).

This relation is given by Ohm's law $\mathbf{j} = \sigma \mathbf{E}$, which is always expected to hold for small enough values of electric field strength, and needs to be obtained from some microscopical model of the system. We would further always assume that the media is uniform in space and time, hence, in the

most general form, the relation between the current and the electric field is

$$\mathbf{j}(t,\mathbf{r}) = \int \sigma(\mathbf{r}-\mathbf{r}', t-t')E(t',\mathbf{r}')\,dt'd\mathbf{r}' \qquad \Leftrightarrow \qquad \mathbf{j}_{\omega,\mathbf{k}} = \sigma(\omega,\mathbf{k})\mathbf{E}_{\omega,\mathbf{k}}$$

From Ohm's law and (2.9), (2.10) we also immediately get an expression for permittivity tensor

$$\mathbf{D}_{\omega,\mathbf{k}} = \varepsilon(\omega,\mathbf{k})\mathbf{E}_{\omega,\mathbf{k}}, \qquad \varepsilon(\omega,\mathbf{k}) = 1 + \frac{4\pi i}{\omega}\sigma(\omega,\mathbf{k}) \tag{2.11}$$

The Drude–Lorentz model is the simplest classical framework that captures the main behavior of conductivity at optical frequencies; it is derived in Appendix A.

2.1.2 Structure of permittivity tensor for uniform media

Uniaxial crystal What possible form could the permittivity tensor ε have? If the crystal is isotropic, the only option is for ε to be a scalar $\varepsilon_{ij} = \varepsilon_0\delta_{ij}$. The simplest type of birefringent material is a *uniaxial crystal*, such as Iceland spar, meaning that there is a single direction $\mathbf{a}$ governing the optical anisotropy [62, §98]. In the basis consisting of $\mathbf{a}$ and its orthogonal complements,

$$\varepsilon = \begin{pmatrix} \varepsilon_x & & \\ & \varepsilon_y & \\ & & \varepsilon_y \end{pmatrix} \tag{2.12}$$

In an arbitrary system of coordinates, the same statement could be written as

$$\varepsilon_{ij} = \varepsilon_\perp(\delta_{ij} - a_i a_j) + \varepsilon_\parallel a_i a_j. \tag{2.13}$$

This expression follows from the fact that the identity matrix δ_{ij} and vector $\mathbf{a}$ are the only invariant objects present, so ε has to be a linear combination thereof.

Magneto–optical effects For isotropic media in the presence of magnetic field $\mathbf{H}$ [62, §101]

$$\varepsilon_{ij} = \varepsilon_0\delta_{ij} - ig\epsilon_{ijk}H_k \tag{2.14}$$

Since the magnetic field is a pseudo-vector, it needs to be multiplied by the Levi-Civita pseudo-tensor. For example, within the Drude model (A.1) without dissipation $\tau \to \infty$ permittivity tensor looks like

$$\varepsilon_{ij} = \left(1 - \frac{\omega_p^2}{\omega^2 - \Omega^2}\right)\delta_{ij} - \frac{i\omega_p^2}{\omega(\omega^2-\Omega^2)}\epsilon_{ijk}\Omega_k + \frac{\omega_p^2}{\omega^2(\omega^2-\Omega^2)}\Omega_i\Omega_j.$$

Here Ω is the cyclotron frequency and ω_p is the plasma frequency.

$$\mathbf{\Omega} = -\frac{|e|}{mc}\mathbf{H}, \qquad \omega_p^2 = \frac{4\pi n e^2}{m}.$$

In (2.14), higher order terms H^2 were neglected since cyclotron frequency is much smaller than any characteristic frequency, and also usually $\mathbf{E} \perp \mathbf{H}$.

For uniaxial material in magnetic field terms (2.13) and (2.14) are combined, and the coefficient g becomes a matrix.

$$\varepsilon_{ij} = \varepsilon_\perp(\delta_{ij} - a_i a_j) + \varepsilon_\parallel a_i a_j + i\epsilon_{ijk} g_{kl} H_l$$

Spatial dispersion So far we have assumed that ε_0, $\varepsilon_\perp$, $\varepsilon_\parallel$, g only depend on frequency. Once we remember that in general $\varepsilon = \varepsilon(\omega, \mathbf{k})$, we could also use vector $\mathbf{k}$ to construct possible tensors. When crystal is isotropic and has an inversion symmetry [62, §103] most general form is

$$\varepsilon_{ij} = \varepsilon_\perp \left(\delta_{ij} - \frac{k_i k_j}{k^2}\right) + \varepsilon_\parallel \frac{k_i k_j}{k^2}.$$

However, there is also a special case of spatial dispersion in materials with broken inversion, which creates a linear–in–k term similar to the magnetic field called *natural optical activity* [62, §104]

$$\varepsilon_{ij}(\omega, \mathbf{k}) = \varepsilon_0(\omega)\delta_{ij} + ig\epsilon_{ijk}\frac{k_k}{k}. \tag{2.15}$$

Chiral materials are known to be optically active, such as the materials with cholesteric order [65].

Gyrotropy Terms like (2.14) and (2.15) are called *gyrotropy*, because they rotate polarization of the light in transmission. It is, however, important to note that when transparent material is passed twice in the opposite direction, rotation due to natural optical activity cancels out, while rotation due to the magnetic field is doubled.

Whether rotation *in reflection* could happen due to natural optical activity and not only due to magnetic gyrotropy is still an open question (see Ref. [3] for review). It's tempting to say that rotation of polarization in reflection is indicative only of time-reversal symmetry breaking effects; however, a long list of controversial experiments and theories does not let us come to a simple conclusion. We will discuss this topic in more detail and circle back to the definition of gyrotropy later in this chapter.

2.1.3 Propagation of plane waves

Next, let us consider the propagation of light in media. Namely, let us assume that electromagnetic fields have the form of a plane monochromatic wave $\mathbf{E} \propto e^{-i\omega t + i\mathbf{kr}}$. Maxwell's equations are

simplified to the following form.

$$\begin{cases} \nabla \cdot \mathbf{D} = 0 \\ \nabla \cdot \mathbf{B} = 0 \\ \nabla \times \mathbf{E} = -\partial_t \mathbf{B} \\ \nabla \times \mathbf{H} = \partial_t \mathbf{D} \end{cases} \rightarrow \begin{cases} \mathbf{n} \cdot \mathbf{D} = 0 \\ \mathbf{n} \cdot \mathbf{B} = 0 \\ \mathbf{B} = \mathbf{n} \times \mathbf{E} \\ \mathbf{D} = -\mathbf{n} \times \mathbf{H} \end{cases} \quad \text{with} \quad \mathbf{n} = \frac{\mathbf{k}}{\omega}. \tag{2.16}$$

Substituting $\mathbf{H} = [\mathbf{n} \times \mathbf{E}]$ into $\mathbf{D} = \varepsilon \mathbf{E} = -[\mathbf{n} \times \mathbf{H}]$, we obtain an equation [62, (97.8)] which resembles an eigenproblem with additional relation between eigenvalues and the matrix itself.

$$\left(n^2 \delta_{ij} - n_i n_j - \varepsilon_{ij}\right) E_j = 0, \qquad i, j, k = x, y, z. \tag{2.17}$$

In order for a nontrivial solution to exist, the matrix has to be degenerate, i.e.

$$\det\left(\varepsilon + \mathbf{n} \otimes \mathbf{n}^\intercal - n^2\right) = 0 \tag{2.18}$$

Equation (2.18) is a dispersion relation[2] since it implicitly establishes the relation between the frequency ω and the wavevector $\mathbf{k}$. To make it more obvious, we can rewrite it as

$$\det\left(\frac{\omega^2}{c^2}\varepsilon + \mathbf{k} \otimes \mathbf{k}^\intercal - k^2\right) = 0$$

Solutions of this equation $\omega_i(\mathbf{k})$ determine allowed values of frequencies and wavevectors, and eigenvectors $\mathbf{E}_n$ give corresponding allowed polarization directions.

2.1.4 Effective 2D permittivity tensor

Let us study the structure of equation (2.17) a little more carefully. Let the direction of wavevector $\mathbf{k} = -k\mathbf{e}_z$ be parallel to the z-axis. Then explicitly in coordinates, we have

$$\begin{pmatrix} \varepsilon_{xx} - n^2 & \varepsilon_{xy} & \varepsilon_{xz} \\ \varepsilon_{yx} & \varepsilon_{yy} - n^2 & \varepsilon_{yz} \\ \varepsilon_{zx} & \varepsilon_{zy} & \varepsilon_{zz} \end{pmatrix} \begin{pmatrix} E_x \\ E_y \\ E_z \end{pmatrix} = 0$$

As long as $\varepsilon_{zz} \neq 0$, we can always express E_z through E_x and E_y

$$E_z = -\frac{\varepsilon_{z\alpha} E_\alpha}{\varepsilon_{zz}} \equiv -\frac{\varepsilon_{zx} E_x}{\varepsilon_{zz}} - \frac{\varepsilon_{zy} E_y}{\varepsilon_{zz}}$$

[2] Sometimes it's called Fresnel equation, but we would avoid this name not to confuse it with Fresnel equation for reflection and transmission amplitudes.

and obtain

$$\epsilon_{\alpha\beta}E_\beta = n^2 E_\alpha, \qquad \alpha,\beta = x,y. \tag{2.19}$$

with effective 2D permittivity tensor

$$\epsilon = \begin{pmatrix} \varepsilon_{xx} & \varepsilon_{xy} \\ \varepsilon_{yx} & \varepsilon_{yy} \end{pmatrix} - \frac{1}{\varepsilon_{zz}} \begin{pmatrix} \varepsilon_{zx} & \varepsilon_{zy} \end{pmatrix} \otimes \begin{pmatrix} \varepsilon_{xz} \\ \varepsilon_{yz} \end{pmatrix} \tag{2.20}$$

Eigenproblems (2.19) and (2.17) are equivalent as long as $\varepsilon_{zz} \neq 0$. If we solved eigenproblem (2.19) and obtained an eigenpair n^2, $\mathbf{E}_\perp$, then we can automatically find solution of eigenproblem (2.17) with $\mathbf{n} = (0,0,n)$, $\mathbf{E} = (E_x, E_y, \varepsilon_{zz}^{-1}\varepsilon_{z\alpha}E_\alpha)$. We see that the effective eigenproblem is two-dimensional, so there are only two solutions: ordinary and extraordinary waves.

2.2 Normal propagation

So far, we have only considered uniform media. Now we will show how an electromagnetic wave is reflected upon normal incidence from the phase boundary between vacuum and media with permittivity ε. In this section we take the customary approach: we assume that deep in the bulk and far away from the boundary in the vacuum, previously derived relations for uniform media hold. At the boundary, two waves are going to be linked to each other by matching values of electric field and its derivatives. In the next section, we would generalize this method to position-dependent permittivity tensor.

2.2.1 Boundary conditions

Let us assume that the incident wave is in vacuum $\varepsilon_0 = 1$. Let $\mathbf{E}$, $\mathbf{E}'$, $\mathbf{E}''$ be the incident, reflected and transmitted waves respectively (see Fig. 2.1). From Maxwell's equation $\nabla \times \mathbf{E} = -\frac{1}{c}\partial_t \mathbf{H}$ we deduce boundary condition $\mathbf{E}_\perp + \mathbf{E}'_\perp = \mathbf{E}''_\perp$, which has to be true along the whole $z = 0$ plane, i.e. for any position along the boundary $\mathbf{r}_\tau = (x, y, 0)$.

$$\mathbf{E}_\perp e^{-i\omega t + i\mathbf{k}\mathbf{r}_\tau} + \mathbf{E}'_\perp e^{-i\omega' t + i\mathbf{k}'\mathbf{r}_\tau} = \mathbf{E}''_\perp e^{-i\omega'' t + i\mathbf{k}''\mathbf{r}_\tau}.$$

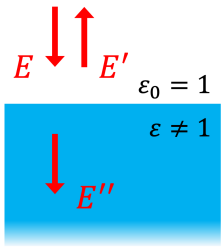

Figure 2.1: Phase boundary

From this identity follows $\omega = \omega' = \omega''$ and $\mathbf{k}_\perp = \mathbf{k}'_\perp = \mathbf{k}''_\perp$, where $\mathbf{k}_\perp = (k_x, k_y)$. Since $k_z = 0$, we deduce that $\mathbf{k}'$ and $\mathbf{k}''$ are parallel to the z-axis. Furthermore, since $\omega = \omega'$, from dispersion relation $n^2 = 1$ which holds for vacuum, we find $|\mathbf{k}| = |\mathbf{k}'|$, hence only two options are allowed $k'_z = \pm k$. We choose signs $\mathbf{k}' = (0,0,-k)$ and $\mathbf{k}'' = (0,0,k)$ based on the physical meaning of reflected and transmitted waves. Generally speaking, a transmitted wave could

consist of two waves $\mathbf{E}'' = \mathbf{E}''_{(o)} + \mathbf{E}''_{(e)}$; however, for the same reason as above, both transmitted waves should have the same frequency and wavevectors.

A full set of boundary conditions is

$$\begin{cases} \nabla \cdot \mathbf{D} = 0 \\ \nabla \cdot \mathbf{B} = 0 \\ \nabla \times \mathbf{E} = -\partial_t \mathbf{B} \\ \nabla \times \mathbf{H} = \partial_t \mathbf{D} \end{cases} \quad \rightarrow \quad \begin{cases} D_\nu^{(1)} = D_\nu^{(2)} \\ B_\nu^{(1)} = B_\nu^{(2)} \\ \mathbf{E}_\tau^{(1)} = \mathbf{E}_\tau^{(2)} \\ \mathbf{H}_\tau^{(1)} = \mathbf{H}_\tau^{(2)} \end{cases}$$

Here $E_\nu = (\boldsymbol{\nu} \cdot \mathbf{E})$ is the component normal to the phase boundary plane, and $\mathbf{E}_\tau = \mathbf{E} - \boldsymbol{\nu} E_\nu$ is its orthogonal complement. In the case of normal incidence $\mathbf{n} = \boldsymbol{\nu}$, even for the transmitted wave, so we would not differentiate between the two. We also note that we reserve notation $\mathbf{E}_\perp = (E_x, E_y)$ for 2–dimensional vectors, while $\mathbf{E}_\tau = (E_x, E_y, 0)$ is 3–dimensional.

As can be seen from (2.16), for any plane wave $\mathbf{n} \cdot \mathbf{D} = 0$, hence boundary condition $D_n^{(1)} = D_n^{(2)}$ is automatically satisfied. Furthermore, since we assume $\mu = 1$ for all media, the magnetic field is continuous at the phase boundary $\mathbf{H}^{(1)} = \mathbf{H}^{(2)}$. Overall, for an optical normal plane wave, the boundary conditions are

$$\begin{cases} \mathbf{E}_\tau^{(1)} = \mathbf{E}_\tau^{(2)} \\ \mathbf{H}^{(1)} = \mathbf{H}^{(2)} \end{cases} \tag{2.21}$$

2.2.2 Reflection from phase boundary

Let us define the operator $\sqrt{\epsilon}$ through its action on eigenvectors of (2.19). When dielectric permittivity is scalar, it coincides with the refraction index $\sqrt{\epsilon} = n = |\mathbf{n}|$, but generally it is a matrix

$$\sqrt{\epsilon} = \sum_\lambda \sqrt{\lambda}\, \mathbf{E}_\lambda \otimes \mathbf{E}_\lambda^\intercal, \qquad\qquad (\mathbf{E}_\lambda \cdot \mathbf{E}_{\lambda'}) = \delta_{\lambda\lambda'}$$

given by eigenvalues $\{\lambda\}$ and normalized eigenvectors $\{\mathbf{E}_\lambda\}$ of matrix ϵ. Then from (2.16) we can express magnetic field

$$\mathbf{H} = \sum_\lambda [\mathbf{n}_\lambda \times \mathbf{E}_{\tau\lambda}] = \operatorname{sgn}(k_z) \sum_\lambda \sqrt{\lambda}\, [\mathbf{e}_z \times \mathbf{E}_{\perp\lambda}] = \operatorname{sgn}(k_z) \left[\mathbf{e}_z \times \sqrt{\epsilon}\mathbf{E}_\perp\right]$$

Here we used $\mathbf{n}_\lambda = \operatorname{sgn}(k_z)\sqrt{\lambda}\mathbf{e}_z$, and we implicitly converted 2D vectors $\mathbf{E}_\perp = (E_x, E_y)$ into 3D vectors $\mathbf{E}_\tau = (E_x, E_y, 0)$ when computing cross product between $\mathbf{e}_z = (0, 0, 1)$ and 2D vectors $\sqrt{\epsilon}\mathbf{E}_\perp$.

Probably a better way to write this expression would be with the Pauli matrix

$$\mathbf{H}_\perp = \operatorname{sgn}(k_z)(-i\sigma_2)\sqrt{\epsilon}\,\mathbf{E}_{\perp\lambda}, \quad H_z = 0.$$

Finally, boundary conditions for a normal wave incoming from the vacuum are

$$\begin{cases} \mathbf{E}_\perp + \mathbf{E}'_\perp = \mathbf{E}''_\perp \\ \mathbf{E}_\perp - \mathbf{E}'_\perp = \sqrt{\epsilon}\,\mathbf{E}''_\perp \end{cases}$$

We can immediately find $\mathbf{E}'_\perp = \frac{1}{2}(1-\sqrt{\epsilon})\mathbf{E}''_\perp$ and finally reflection and transmission amplitudes defined as $\mathbf{E}'_\perp = rE_\perp$ and $\mathbf{E}''_\perp = tE_\perp$.

$$r = \frac{1-\sqrt{\epsilon}}{1+\sqrt{\epsilon}}, \qquad t = \frac{2}{1+\sqrt{\epsilon}}. \tag{2.22}$$

Generally speaking, E''_z is not zero.

2.3 Scattering problem

Let us now consider a non-uniform medium, whose characteristics depend only on one coordinate z. Let us first rederive some relationships we've used before in the case of a uniform space and show how they are modified in the case of a position-dependent medium.

We are interested in waves propagating along z, so all the fields are assumed to depend only on z and t, hence $\nabla = \mathbf{e}_z\partial_z$, while time-dependence has a familiar plane-wave form $e^{-i\omega t}$. In other words, we can take the time-Fourier transform of Ampere-Maxwell's and Faraday's equations.

$$\begin{cases} \partial_t\mathbf{B} = -\nabla\times\mathbf{E} \\ \partial_t\mathbf{D} = \nabla\times\mathbf{B} \end{cases} \quad\to\quad \begin{cases} \mathbf{B} = \frac{1}{i\omega}\mathbf{e}_z\times\partial_z\mathbf{E}_\tau \\ -i\omega\mathbf{D} = \mathbf{e}_z\times\partial_z\mathbf{B} \end{cases} \tag{2.23}$$

Previously, we had plane waves with a fixed wavevector and relations (2.16); now, the derivative with respect to z is left untouched. Since the electric field enters only in a vector product, its z-component is irrelevant and can be disregarded $\mathbf{E} \mapsto \mathbf{E}_\tau \equiv (E_x, E_y, 0)$. Combining two equations (2.23) we obtain one-dimensional wave equation

$$\partial_z^2\mathbf{E}_\tau + \omega^2\mathbf{D} = 0.$$

From here, it also follows that $D_z = 0$; however, in general, $E_z \neq 0$ inside the medium.

For an arbitrary non-uniform medium, vectors $\mathbf{D}$ and $\mathbf{E}$ are connected via a general linear

response theory relation

$$\mathbf{D} = \hat{\varepsilon}\mathbf{E}, \qquad D_i(\omega,\, z) = \int dz' \varepsilon_{ij}(\omega,\, z,\, z') E_j(z') \tag{2.24}$$

Here, hat-notation is used to distinguish the function operator from regular matrices. Similar to Eq. (2.20) we can exclude E_z using $D_z = 0$ condition

$$0 = \hat{\varepsilon}_{zx}E_x + \hat{\varepsilon}_{zy}E_y + \hat{\varepsilon}_{zz}E_z \qquad \Rightarrow \qquad E_z = -\hat{\varepsilon}_{zz}^{-1}\left(\hat{\varepsilon}_{zx}E_x + \hat{\varepsilon}_{zy}E_y\right)$$

and introduce a modified dielectric tensor

$$\mathbf{D}_\perp = \hat{\epsilon}\mathbf{E}_\perp, \qquad \text{where} \qquad \hat{\epsilon} = \begin{pmatrix} \hat{\varepsilon}_{xx} - \hat{\varepsilon}_{xz}\hat{\varepsilon}_{zz}^{-1}\hat{\varepsilon}_{zx} & \hat{\varepsilon}_{xy} - \hat{\varepsilon}_{xz}\hat{\varepsilon}_{zz}^{-1}\hat{\varepsilon}_{zy} \\ \\ \hat{\varepsilon}_{yx} - \hat{\varepsilon}_{yz}\hat{\varepsilon}_{zz}^{-1}\hat{\varepsilon}_{zx} & \hat{\varepsilon}_{yy} - \hat{\varepsilon}_{yz}\hat{\varepsilon}_{zz}^{-1}\hat{\varepsilon}_{zy} \end{pmatrix}$$

Here $\mathbf{E}_\perp = (E_x, E_y)$ and $\mathbf{D}_\perp = (D_x, D_y)$ are two-dimensional vectors. So we have the wave equation, which is reduced to

$$\partial_z^2\mathbf{E}_\perp + \omega^2\hat{\epsilon}\mathbf{E}_\perp = 0 \tag{2.25}$$

For the remainder of this section, we will drop the notation distinguishing three-dimensional vectors and will only use two-dimensional ones $\mathbf{E}_\perp \mapsto \mathbf{E}$, $\mathbf{D}_\perp \mapsto \mathbf{D}$.

Of course in practice, instead of (2.24) a concrete microscopic model needs to be found to describe conductivity and permittivity tensors. It's reasonable to assume that displacement field depends only on the electric field at the same point, i.e.

$$D_i(z) = \epsilon_{ij}(\omega, z)E_j(z).$$

Deviations from locality are usually considered as small corrections and we will invoke them when we're dealing with natural optical activity.

2.3.1 Quantum mechanical analogy

There exists a beautiful correspondence between scattering problem in electrodynamics and quantum mechanics [66, 67]. Formally, wave equation for time-translation invariant system looks exactly like stationary Schrödinger equation

$$-\partial_z^2\mathbf{E} - \omega^2\epsilon(\omega,\, z)\mathbf{E} = 0 \qquad \Leftrightarrow \qquad -\partial_z^2\psi + U(z)\psi = 0$$

with potential profile being set by permittivity tensor $U(z) = -\omega^2\epsilon(\omega, z)$. If we have a piece-wise permittivity function, such that inside each region ϵ is a scalar constant, then, similar to the 1D Schrödinger scattering problem, the solution is given by plane waves with different wavevectors k inside each medium, and related to each other through boundary conditions (compare to (2.21))

$$\begin{aligned} \mathbf{E}(z-0) = \mathbf{E}(z+0) \quad &\Leftrightarrow \quad \psi(z-0) = \psi(z+0), \\ \mathbf{B}(z-0) = \mathbf{B}(z+0) \quad &\Leftrightarrow \quad \partial_z\psi(z-0) = \partial_z\psi(z+0), \end{aligned}$$

Importantly, the wavefunction ψ in this analogy is two-dimensional, i.e., it is a spinor, and the potential felt by each component is different, while mixing between different spinors is also possible. Let us decompose the two-dimensional permittivity matrix into the basis of Pauli matrices $\omega^2\epsilon_{ij}(\omega, z) = \boldsymbol{\sigma}_{ij} \cdot \mathcal{B}(\omega, z)$. Now wave equation (2.25) looks like Pauli equation with fictitious z-dependent magnetic field $\mathcal{B}$.

$$-\partial_z^2\psi - (\boldsymbol{\sigma} \cdot \mathcal{B})\,\psi = 0, \qquad \psi = \begin{pmatrix} \psi_\uparrow \\ \psi_\downarrow \end{pmatrix}$$

For example, a birefringent material has $\mathcal{B}$ along the z-axis, so each spinor obtains a different phase. One needs to be accurate, not to stretch this analogy too far, namely, the spin matrix $\boldsymbol{\sigma}$ and permittivity tensor ϵ behave differently when the coordinate system axes are rotated. Let's say we rotated all vectors around z-axis by angle η, electric field transforms as $\mathbf{E}_\eta = R_\eta\mathbf{E}$ and permittivity matrix transforms as $\epsilon_\eta = R_\eta\epsilon R_{-\eta}$, with $R_\eta = \exp[-i\eta\sigma_y]$. Remarkably, this is equivalent to rotating components $(\mathcal{B}_x, \mathcal{B}_z)$ by angle $-\eta$. However, a true spinor would have rotated according to $\exp[-\frac{i}{2}\eta\sigma_z]$.

Energy flow conservation This analogy is helpful in many ways. For example, we know that transparent material does not lead to any dissipation; this is equivalent to energy conservation, which is provided by the hermiticity of the Hamiltonian in quantum mechanics. Similarly, in optics, when $\varepsilon^\dagger = \varepsilon$, energy flow is conserved.

Let's consider a medium with asymptotically constant permittivity

$$\varepsilon(\omega,\, z) = \begin{cases} 1, & z \to -\infty \\ \varepsilon_\infty(\omega), & z \to +\infty \end{cases}$$

Next, we take the wave equation (2.25) and its complex conjugate, multiply the first by $\mathbf{E}^*$ and the

second by $\mathbf{E}$, and subtract one from the other.

$$\begin{cases} \partial_z^2 \mathbf{E} = -\omega^2 \varepsilon \mathbf{E} \\ \partial_z^2 \mathbf{E}^* = -\omega^2 \varepsilon^* \mathbf{E}^* \end{cases} \qquad \Rightarrow \qquad \mathbf{E}^* \cdot \partial_z^2 \mathbf{E} - \mathbf{E} \cdot \partial_z^2 \mathbf{E}^* = -\omega^2 \mathbf{E}^* \left(\varepsilon - \varepsilon^\dagger\right) \mathbf{E}$$

Assuming the transparency ($\varepsilon^\dagger = \varepsilon$), we find $\mathbf{E}^* \cdot \partial_z \mathbf{E} - \mathbf{E} \cdot \partial_z \mathbf{E}^* = const$. From the asymptotic behavior of the wave, we get

$$\mathbf{E} = \begin{cases} \left(e^{ikz} + re^{-ikz}\right) \mathbf{E}_0, & z \to -\infty \\ e^{in_\infty kz} t\, \mathbf{E}_0, & z \to +\infty \end{cases} \qquad \Rightarrow \qquad \mathbb{I} = r^\dagger r + t^\dagger n_\infty t = R + T$$

Here, T and R are transmission and reflection coefficients, defined as the ratio of energy density currents; a quantum mechanical analogy would be a probability density of currents.

2.3.2 Phase boundary with natural optical activity

Let's consider a case of a single-phase boundary between a vacuum and naturally active media. We have already calculated the transmission and reflection amplitudes for a single boundary without natural optical activity earlier, as shown in (2.22). We would consider the simplest case of isotropic media, in which the permittivity is given by (2.15). However, we must be cautious with this expression, as it was shown in Ref. [68],

$$D_i = \epsilon_1 E_i + \gamma e_{ij} \partial_z E_j + \frac{1}{2} \partial_z \gamma \cdot e_{ij} E_j \tag{2.26}$$

where e_{ij} is totally anti-symmetric tensor Levi-Civita. Since $\gamma(z) = \gamma\theta(-z)$, we can further simplify this to

$$\mathbf{D} = \epsilon_{k=0}(z)\mathbf{E} + \gamma(z)[\mathbf{e}_z \times \partial_z \mathbf{E}] - \frac{\gamma}{2}\delta(z)[\mathbf{e}_z \times \mathbf{E}] \qquad \epsilon_{k=0}(z) = \begin{cases} \epsilon_0, & z > 0 \\ \epsilon_1, & z < 0 \end{cases}$$

and the wave equation becomes

$$\frac{-1}{\omega^2} \partial_z^2 \mathbf{E} = \mathbf{D} = \epsilon_{k=0}(z)\mathbf{E} + \gamma(z)[\mathbf{e}_z \times \partial_z \mathbf{E}] - \frac{\gamma}{2}\delta(z)[\mathbf{e}_z \times \mathbf{E}]$$

Boundary conditions are modified to

$$\begin{aligned} \mathbf{E}(z+0) - \mathbf{E}(z-0) &= 0, \\ \partial_z \mathbf{E}(z+0) - \partial_z \mathbf{E}(z-0) &= \omega^2 \frac{\gamma}{2} [\mathbf{e}_z \times \mathbf{E}] \end{aligned}$$

Wave in zeroth media (air) satisfies $(\partial_z^2 + \omega^2\epsilon_0)\mathbf{E} = 0$, so it has to be a plane wave with wavevectors $k_0^{\pm} = \pm\omega\sqrt{\epsilon_0}$. For the wave inside the media, our intuition from the uniform case tells us that circularly polarized light diagonalizes the permittivity tensor with a gyrotropic term. Thus, we propose that the solution has the form.

$$\mathbf{E}(z>0) = \mathbf{E}_0^{\searrow} e^{-ik_0 z} + \mathbf{E}_0^{\nearrow} e^{ik_0 z},$$
$$\mathbf{E}(z<0) = E_1^{+}\mathbf{e}_{+} e^{-ik_1^{+} z} + E_1^{-}\mathbf{e}_{-} e^{-ik_1^{-} z}$$

Here $\mathbf{e}_{\pm} = \frac{1}{\sqrt{2}}(\mathbf{e}_x \pm i\mathbf{e}_y)$ are unit circularly polarized vectors. Then, inside the media

$$\partial_z^2\mathbf{E} + \omega^2\epsilon_1\mathbf{E} + \omega^2\gamma[\mathbf{e}_z \times \partial_z\mathbf{E}] = 0$$

Since $[\mathbf{e}_z \times \mathbf{e}_{\pm}] = \mp i\mathbf{e}_{\pm}$, we can project this equation to each circular polarization to get

$$(k_1^{\pm})^2 \pm \omega^2\gamma k_1^{\pm} = \omega^2\epsilon$$

These dispersion relations determine values of $k_1^{\pm}$ for each of the circularly polarized components. Each equation has two solutions, but only one with $\mathrm{Re}[k_1^{\pm}] > 0$ should be considered, as we're interested in forward propagation solutions only.

$$\frac{k_1^{\pm}}{\omega} = \sqrt{\epsilon_1 + \frac{1}{4}\omega^2\gamma^2} \mp \frac{1}{2}\omega\gamma.$$

Let us introduce $\tilde{k}_1$ according to $k_1^{\pm} = \tilde{k}_1 \mp \frac{1}{2}\omega^2\gamma$. Then, due to cancellation of $\pm$ terms in the boundary conditions, we are left with

$$\begin{cases} \mathbf{E}_0^{\searrow} + \mathbf{E}_0^{\nearrow} = E_1^{+}\mathbf{e}_{+} + E_1^{-}\mathbf{e}_{-}, \\ k_0\mathbf{E}_0^{\searrow} - k_0\mathbf{E}_0^{\nearrow} = \tilde{k}_1\left(E_1^{+}\mathbf{e}_{+} + E_1^{-}\mathbf{e}_{-}\right) \end{cases}$$

Just as before, reflection and transmission amplitudes are

$$r = \frac{\tilde{k}_1 - k_0}{\tilde{k}_1 + k_0}, \qquad\qquad t = \frac{2k_0}{\tilde{k}_1 + k_0}.$$

Importantly, $\tilde{k}_1$ enters the expression instead of $k_1^{\pm}$. Due to the last term in Eq. (2.26), the boundary condition was modified, and as a result, the reflection amplitude matrix r turned out to be a scalar. Hence, $E_1^{+} = E_1^{-}$.

We see that there is no polarization rotation in reflected light when gyrotropy comes from natural optical activity. This is a significant result since it allows us to distinguish between TRS and TRSB types of gyrotropy. Of course, magnetically gyrotropic media would have rotated reflected light.

2.3.3 Transparent slab

Let's consider a case of propagation through a single layer of $z \in [0, a]$ of the material with permittivity $\varepsilon(\omega)$ surrounded by vacuum (see Fig. 2.2a).

$$\epsilon(\omega,\, z) = 1 + (\epsilon(\omega) - 1)\theta(z)\theta(a - z)$$

We shall denote as $\mathbf{E}_0^{\pm}$ and $\mathbf{E}_1^{\pm}$ the amplitudes of waves in vacuum (0) and medium (1) on the boundary $z = 0$ ($\pm$ corresponds to forward and backward propagation along the $-z$ axis).

At the second boundary, these fields get a phase shift $\mathbf{E}_1^{\pm} \to e^{\pm i\phi}\mathbf{E}_1^{\pm}$, where $\phi = kan$, $n = \sqrt{\epsilon}$, and ϵ is generally speaking a 2×2 matrix. After the second boundary, only the transmitted wave remains $\mathbf{E}_2^{+}$.

From the boundary conditions

$$(0 \to 1) : \begin{cases} \mathbf{E}_0^{+} + \mathbf{E}_0^{-} = \mathbf{E}_1^{+} + \mathbf{E}_1^{-} \\ \mathbf{E}_0^{+} - \mathbf{E}_0^{-} = \hat{n}\left(\mathbf{E}_1^{+} - \mathbf{E}_1^{-}\right) \end{cases} \qquad (1 \to 2) : \begin{cases} e^{i\varphi}\mathbf{E}_1^{+} + e^{-i\varphi}\mathbf{E}_1^{-} = \mathbf{E}_2^{+} \\ n\left(e^{i\varphi}\mathbf{E}_1^{+} - e^{-i\varphi}\mathbf{E}_1^{-}\right) = \mathbf{E}_2^{+} \end{cases} .$$

we can immediately find scattering amplitudes $\mathbf{E}_2^{+} = t\mathbf{E}_0^{+}$, $\mathbf{E}_0^{-} = r\mathbf{E}_0^{+}$.

$$r = \frac{i(n^2 - 1)\sin\varphi}{2n\cos\varphi - i(n^2 + 1)\sin\varphi}, \qquad t = \frac{2n}{2n\cos\varphi - i(n^2 + 1)\sin\varphi}$$

And for the reflection R and transmission coefficients T:

$$R = r^{\dagger}r = \frac{(n^2 - 1)^2\sin^2\varphi}{4n^2 + (n^2 - 1)^2\sin^2\varphi}, \qquad T = t^{\dagger}t = \frac{4n^2}{4n^2 + (n^2 - 1)^2\sin^2\varphi}$$

where we assumed transparency, i.e., ε is hermitian.

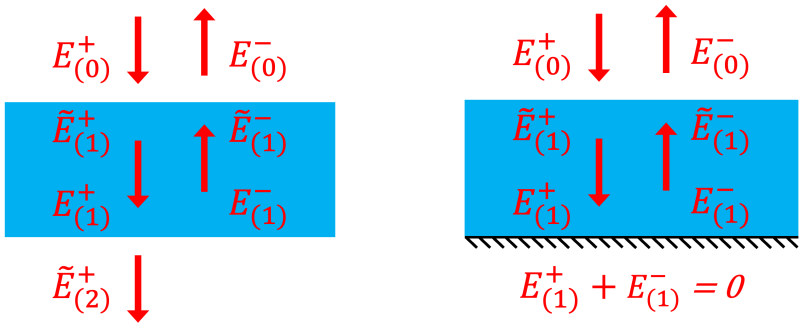

(a) Transparent slab (b) Back-and-forth transmission

Figure 2.2: Scattering problem setups

2.3.4 Jones formalism

Let us now consider the following example, important in practice: light travels through transparent media, reflects from a perfect mirror, and travels back. Can we somehow use the result we've obtained above? Maybe it's legitimate to say that light travelling is multiplied by the transmission coefficient on the way forward, then multiplied by the reflection amplitude of the mirror, and finally, once again, by the transmission transfer matrix on the way back?

Such an approach, which deals with multiple consecutive optical elements sequentially, is called Jones calculus. Let us derive the applicability condition of the Jones approximation.

Consider the setup shown in Fig. 2.2b. When the second boundary is the perfect mirror $\mathbf{E}_2^+ = 0$. We can immediately derive the following expression from the reflection amplitude obtained above.

$$r_M = -\frac{n\cos\varphi + i\sin\varphi}{n\cos\varphi - i\sin\varphi}, \qquad R_M = r_M^\dagger r_M = 1$$

In the Jones matrix approach, with $r_m = -1$ being the reflection amplitude from a perfect mirror, we would instead get

$$r_J = t_{10}e^{i\varphi}r_m e^{i\varphi}t_{01} = -\frac{4ne^{2i\varphi}}{(1+n)^2} \neq r_M, \qquad R_J = r_J^\dagger r_J \neq 1$$

How to reconcile the two results? The multi-ray interference approach (like in the Fabry–Pérot interferometer) extends the Jones formula.

$$r_{FP} = r_{01} + r_m t_{10}t_{01}e^{2i\varphi}\sum_{l=0}^{\infty}\left(r_m r_{10}e^{2i\varphi}\right)^l = r_{01} + \frac{r_m t_{10}t_{01}e^{2i\varphi}}{1 - r_m r_{10}e^{2i\varphi}} = r_{01} + \frac{r_J}{1 - r_m r_{10}e^{2i\varphi}}$$

$$t_{01} = \frac{2}{1+n}, \quad r_{01} = \frac{1-n}{1+n}, \quad t_{10} = \frac{2n}{1+n}, \quad r_{10} = \frac{n-1}{1+n} \qquad \Rightarrow \qquad r_{FP} = r_M$$

We see that if reflection upon exiting the media back into the air, is small $|r_{01}|, |r_{10}| \ll 1$, Jones' formula coincides with the self-consistent approach $r_M \approx r_J$. This is the applicability condition of the Jones' approximation. Alternatively, if we're dealing with conducting or absorbing material, such that after each pass through the material light intensity is dramatically reduced, we could also ignore many Fabry–Pérot reflections.

2.4 Definition of Magneto–optical Kerr Effect (MOKE)

Let us start with a remark that John Kerr made many contributions to the foundations of optics and named a plethora of different phenomena after himself. Here we are only interested in the so-called magneto-optical Kerr effect (MOKE), a sibling of the magneto-optical Faraday effect (MOFE). The Kerr effect is loosely defined as a rotation of the polarization of the light upon reflection from magnetized material (see Fig. 2.3). This is a very *confusing* definition for the following reasons:

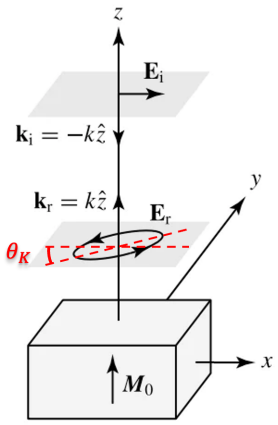

Figure 2.3: Naive definition of Kerr effect

1. It ignores the fact that the rotation of linear polarization could be caused by linear birefringence or linear dichroism, which are non-magnetic in nature.

2. It implicitly assumes the incident light is linearly polarized since it cannot be generalized to the case when the incident light is nearly circularly polarized.

A more accurate definition should encompass the microscopic properties of the interaction between light and electrons. At its core, the Kerr effect is caused by the magnetic orbital motion of electrons. Hence, we ought to say that material exhibits the Kerr effect when its microscopic properties lead to a change of polarization of the light in the same manner as a magnetic field would.

In the classical picture, this means that electrons shaken by an incoming electromagnetic wave move in a curved trajectory, which causes polarization of the re-emitted light to rotate (see Fig. 2.4).

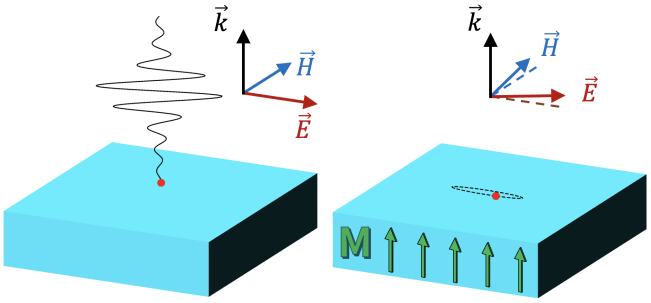

Figure 2.4: Lorentz force as a source of MOKE

To clarify our point, let us provide an analogy. The transport Hall effect is not defined through a measurement procedure (e.g., applying a current along the x axis and measuring the voltage along the y axis). One can choose to measure conductivity instead of resistivity, or Corbino disk geometry instead of a Hall bar. The definition remains independent of setup, leaving implementation to the

experimentalist. Likewise, the Kerr effect should not be defined solely by polarization rotation, but rather through linear response theory, which describes light–matter interactions.

Information about the orbital motion of electrons is encoded in the conductivity tensor. In sections 2.1 and 2.2, we have demonstrated how to obtain the reflection Jones matrix r, which relates amplitudes of the normally incident and reflected electric field $\mathbf{E}_{\text{ref}} = r\mathbf{E}_{\text{inc}}$. Starting from Maxwell's equation, we have demonstrated that given a conductivity tensor, we can obtain the reflection amplitude r. Conductivity, in turn, needs to be calculated from some microscopic model, using something like the Kubo formula or the DFT scheme. This procedure could be pictorially represented as follows.

$$\left.\begin{matrix}\text{Drude-Lorentz}\\ \text{Kubo formula}\\ \text{DFT calculation}\\ \dots\end{matrix}\right\} \xrightarrow[(2.11)]{} \varepsilon \xrightarrow[(2.20)]{} \epsilon \xrightarrow[(2.22)]{} \left\{\begin{matrix}t\\ r\end{matrix}\right\} \longrightarrow \left\{\begin{matrix}\text{Kerr/Faraday effect}\\ \text{Circ. dichroism}\\ \text{Lin. birefringence}\\ \dots\end{matrix}\right.$$

In this section, we will focus on the manifestations of different types of changes in polarization upon reflection and classify the manifestations of electron-light interaction in polarization-sensitive measurements.

2.4.1 Basis convention

When operating with reflection matrices, it is essential to consider the chosen basis. In this manuscript, we always use a fixed system of coordinates, such that the mirror has an identity reflection matrix in both linear and circular bases.

$$S = \begin{pmatrix}1 & 0\\ 0 & 1\end{pmatrix} \qquad \Sigma = \begin{pmatrix}1 & 0\\ 0 & 1\end{pmatrix}$$

Here $\Sigma = O^{-1}SO$ is matrix in basis of circular polarization

$$\mathbf{e}_{\pm} = \frac{1}{\sqrt{2}}(\mathbf{e}_x \pm i\mathbf{e}_y), \tag{2.27}$$

which are related to each other with a unitary matrix

$$O = \frac{1}{\sqrt{2}}\begin{pmatrix}1 & 1\\ i & -i\end{pmatrix} \qquad O^{-1} = \frac{1}{\sqrt{2}}\begin{pmatrix}1 & -i\\ 1 & i\end{pmatrix}$$

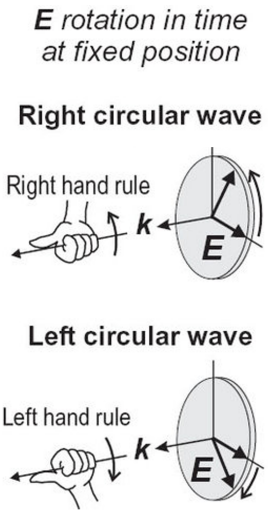

Figure 2.5: Circular polarizations

However, the most popular convention used in the literature is different. In Jones calculus, the system of coordinates is linked to the direction of propagation such that the z–axis is always aligned

with the wavevector $\mathbf{k}$. Because of it, upon reflection, some axes are flipped $z \mapsto -z$ and $y \mapsto -y \equiv \bar{y}$. This leads to bizarre results: the mirror's Jones matrix is the Pauli matrix σ_3.

$$S^{(xy,x\bar{y})} = \begin{pmatrix} 1 & 0 \\ 0 & -1 \end{pmatrix}$$

Furthermore, when working in a circular basis, instead of using the same vectors before and after reflection, adepts of Jones calculus also choose to complicate their life and choose right and left–circularly polarized unit vectors as a basis. Handedness is defined with respect to the direction of propagation.

$$\begin{aligned} &\text{Incident light } (\mathbf{k} \downarrow\uparrow \mathbf{e}_z): && \mathbf{e}_r^{\swarrow} = \frac{1}{\sqrt{2}}(\mathbf{e}_x - i\mathbf{e}_y), && \mathbf{e}_l^{\swarrow} = \frac{1}{\sqrt{2}}(\mathbf{e}_x + i\mathbf{e}_y). \\ &\text{Reflected light } (\mathbf{k} \uparrow\uparrow \mathbf{e}_z): && \mathbf{e}_r^{\nearrow} = \frac{1}{\sqrt{2}}(\mathbf{e}_x + i\mathbf{e}_y), && \mathbf{e}_l^{\nearrow} = \frac{1}{\sqrt{2}}(\mathbf{e}_x - i\mathbf{e}_y). \end{aligned}$$

Obviously, proper circular basis (2.27) does not change upon reflection. Naturally, there is a one-to-one relation between matrix elements in these two representations

$$\begin{pmatrix} S_{++} & S_{+-} \\ S_{-+} & S_{--} \end{pmatrix} = \begin{pmatrix} S_{lr} & S_{ll} \\ S_{rr} & S_{rl} \end{pmatrix}$$

We will not use a confusing basis that flips the axis upon reflection and will avoid distinguishing circular polarization by handedness. We will use $\pm$ circular polarizations (2.27) instead.

2.4.2 Structure of reflection matrix

Sample's reflection matrix S is, generally speaking, an arbitrary 2×2 complex-valued matrix, which does not have any constraints. Such a matrix has eight real parameters. A perfect mirror does not change polarization, so its reflection matrix is scalar. Without loss of generality, the scalar part can be chosen to be unity, so the most general matrix has the form

$$S = 1 + \Lambda\sigma_1 - i\Theta\sigma_2 + \Delta\sigma_3 = \begin{pmatrix} 1+\Delta & \Lambda-\Theta \\ \Lambda+\Theta & 1-\Delta \end{pmatrix} \qquad \Sigma = \begin{pmatrix} 1-i\Theta & \Delta-i\Lambda \\ \Delta+i\Lambda & 1+i\Theta \end{pmatrix}$$

In fact, since σ_1 and σ_3 are related by the rotation matrix

$$R_\eta = \exp\left[-i\eta\sigma_2\right] = \begin{pmatrix} \cos\eta & -\sin\eta \\ \sin\eta & \cos\eta \end{pmatrix}$$

the phase of Λ can always be fixed to an arbitrary value, i.e., it can be considered to be purely real or purely imaginary.

$$\begin{aligned} R_\eta \sigma_x R_\eta^{-1} &= \cos 2\eta \sigma_x - \sin 2\eta \sigma_z, \\ R_\eta \sigma_z R_\eta^{-1} &= \cos 2\eta \sigma_z + \sin 2\eta \sigma_x \end{aligned} \qquad \begin{bmatrix} \Lambda \\ \Delta \end{bmatrix} \underset{\eta}{\mapsto} \begin{bmatrix} \Lambda_\eta \\ \Delta_\eta \end{bmatrix} = R_{2\eta}^{-1} \begin{bmatrix} \Lambda \\ \Delta \end{bmatrix} = \begin{bmatrix} \cos 2\eta & \sin 2\eta \\ -\sin 2\eta & \cos 2\eta \end{bmatrix} \begin{bmatrix} \Lambda \\ \Delta \end{bmatrix}$$

This representation makes it obvious that rotations preserve $[\operatorname{Re}\Lambda]^2 + [\operatorname{Re}\Delta]^2 = \text{const}$ as well as $[\operatorname{Im}\Lambda]^2 + [\operatorname{Im}\Delta]^2 = \text{const}$. Rotations do not affect the Θ term, naturally.

Linear birefringence and dichroism

Looking at the expression for the permittivity tensor of a uniaxial crystal (2.12), we can immediately find the reflection amplitude S using (2.22).

$$\epsilon = \begin{pmatrix} \epsilon_x & 0 \\ 0 & \epsilon_y \end{pmatrix} \qquad S = \begin{pmatrix} r_x & 0 \\ 0 & r_y \end{pmatrix} \qquad r_{x,y} = \frac{1 - \sqrt{\epsilon_{x,y}}}{1 + \sqrt{\epsilon_{x,y}}}$$

As we will show next, when $\beta = \frac{1}{2}\arg(r_x/r_y) \neq 0$ such material exhibits linear birefringence and $|r_x| \neq |r_y|$ manifests itself as linear dichroism.

Circular birefringence and dichroism

Next, let us consider the permittivity tensor of materials with magnetic gyrotropy (2.14). Obviously, circularly polarized plane waves diagonalize such ε, i.e. $O^{-1}\epsilon O = \varepsilon_0 + g\sigma_3$.

$$\epsilon = \begin{pmatrix} \epsilon_0 & -ig \\ ig & \epsilon_0 \end{pmatrix} \qquad \Sigma = \begin{pmatrix} r_+ & 0 \\ 0 & r_- \end{pmatrix} \qquad r_\pm = \frac{1 - \sqrt{\epsilon_\pm}}{1 + \sqrt{\epsilon_\pm}} \qquad \epsilon_\pm = \varepsilon_0 \pm g$$

Typically, this matrix is parametrized with two real parameters: θ_K — Kerr angle (circular birefringence) and ε_K — circular dichroism (Kerr ellipticity).

$$\frac{r_-}{r_+} = \frac{1 - \tan\varepsilon_K}{1 + \tan\varepsilon_K} e^{2i\theta_K} = \tan\left[\frac{\pi}{4} - \varepsilon_K\right] e^{2i\theta_K} \approx 1 + 2i(\theta_K + i\varepsilon_K) \qquad \varepsilon_K, \theta_K \in \mathbb{R}. \quad (2.28)$$

Meaning of matrix elements

To sum up, the reflection matrix generally looks like

$$S = \begin{pmatrix} 1 + \Delta & -\Theta \\ \Theta & 1 - \Delta \end{pmatrix} \qquad S_\eta = R_\eta S R_{-\eta} = \begin{pmatrix} 1 + \Delta\cos 2\eta & -\Theta + \Delta \sin 2\eta \\ \Theta + \Delta \sin 2\eta & 1 - \Delta \cos 2\eta \end{pmatrix}$$

with $\Theta = \theta + i\varepsilon$ describing circular birefringence (MOKE θ) and dichroism (RMCD ε), and with $\Delta = \delta + i\beta$ describing linear birefringence (β) and dichroism (δ). Notably, the Θ–term is proportional

to σ_y, and the rotation matrix $R_\eta = \exp[-i\eta\sigma_y]$ commutes with it. In circular basis

$$\Sigma = O^{-1}SO = \begin{pmatrix} 1-i\Theta & \Delta \\ \Delta & 1+i\Theta \end{pmatrix} \qquad \Sigma_\eta = \exp[i\eta\sigma_z]\Sigma\exp[-i\eta\sigma_z] = \begin{pmatrix} 1-i\Theta & \Delta e^{2i\eta} \\ \Delta e^{-2i\eta} & 1+i\Theta \end{pmatrix}$$

From here $\sigma_{--}/\sigma_{++} \approx 1 + 2i\Theta$, which agrees with more general parametrization (2.28).

2.4.3 Optical rotation of linearly polarized light

Let's see how the rotation of linear polarization induced by different types of optical activity depends on the incident polarization angle.

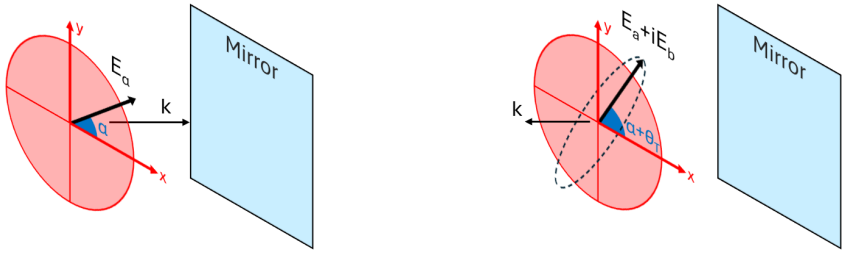

Figure 2.6: Reflection of linearly polarized light

Optical rotation due to linear dichroism

Assume linearly polarized light coming at angle $\mathbf{n}_\alpha$, after reflection it is going to have amplitude

$$\mathbf{E}' = [1+\sigma_z\delta]\,\mathbf{n}_\alpha = \begin{pmatrix} (1+\delta)\cos\alpha \\ (1-\delta)\sin\alpha \end{pmatrix} \qquad \mathbf{n}_\alpha = \begin{pmatrix} \cos\alpha \\ \sin\alpha \end{pmatrix}$$

Such a resulting vector is oriented at an angle

$$\theta_R = \arctan\left[\frac{1-\delta}{1+\delta}\tan\alpha\right] = \alpha - \delta\sin 2\alpha.$$

Importantly, rotation caused by linear birefringence only is $\frac{\pi}{2}$–periodic, while the presence of linear dichroism makes the rotation angle π–periodic function of incident polarization angle.

Optical rotation due to linear birefringence

Jones matrix of a linearly birefringent sample in the main optical axis basis is $J = \exp i\beta\sigma_z$. Upon reflection, light is elliptically polarized $\mathbf{E}'$ and we are mostly interested in the orientation of

its major axis.

$$\mathbf{E}' = \begin{pmatrix} e^{i\beta} & \\ & e^{-i\beta} \end{pmatrix} \begin{pmatrix} \cos\alpha \\ \sin\alpha \end{pmatrix} = \begin{pmatrix} e^{i\beta}\cos\alpha \\ e^{-i\beta}\sin\alpha \end{pmatrix} = \cos\beta \begin{pmatrix} \cos\alpha \\ \sin\alpha \end{pmatrix} + i\sin\beta \begin{pmatrix} \cos\alpha \\ -\sin\alpha \end{pmatrix}$$

In order to find the major axis orientation and the ellipticity of elliptically polarized light, it's useful to transition into a circular basis.

$$\boldsymbol{\mathcal{E}}' = O^{-1}\mathbf{E}' = \frac{1}{\sqrt{2}} \begin{pmatrix} 1 & -i \\ 1 & i \end{pmatrix} \begin{pmatrix} e^{i\beta}\cos\alpha \\ e^{-i\beta}\sin\alpha \end{pmatrix} = \frac{1}{\sqrt{2}} \begin{pmatrix} \cos(\alpha+\beta) - i\sin(\alpha-\beta) \\ \cos(\alpha-\beta) + i\sin(\alpha+\beta) \end{pmatrix}$$

Ellipticity ε_R and major axis orientation θ_R of polarization of reflected light are given by

$$\frac{\cos(\alpha+\beta) - i\sin(\alpha-\beta)}{\cos(\alpha-\beta) + i\sin(\alpha+\beta)} = \frac{1+\tan\varepsilon_R}{1-\tan\varepsilon_R} e^{-2i\theta_R}$$

Finally, the major axis orientation is

$$\theta_R = \frac{1}{2}\arctan\frac{\sin(\alpha+\beta)}{\cos(\alpha-\beta)} + \frac{1}{2}\arctan\frac{\sin(\alpha-\beta)}{\cos(\alpha+\beta)} \approx \alpha - \frac{\beta^2}{2}\sin 4\alpha, \quad \beta \ll 1.$$

Optical rotation due to circular dichroism

Now, let's assume that the sample only has circular dichroism.

$$\mathbf{E}' = (1+\tan\varepsilon\sigma_y)\mathbf{n}_\alpha = \begin{pmatrix} \cos\alpha - i\tan\varepsilon\sin\alpha \\ \sin\alpha + i\tan\varepsilon\cos\alpha \end{pmatrix}$$

We obtained the amplitude of elliptically polarized light with the major axis at an angle $\theta_R = \alpha$. Thus, we've shown that Kerr ellipticity does not rotate linearly polarized light, but rather only makes it elliptical.

Optical rotation due to circular birefringence

Finally, the most interesting case of Kerr rotation.

$$\mathbf{E}' = \exp[-i\theta\sigma_y]\mathbf{n}_\alpha = \begin{pmatrix} \cos(\alpha+\theta) \\ \sin(\alpha+\theta) \end{pmatrix}$$

We see that reflected light has polarization, which is rotated by a fixed amount independently of the initial polarization $\theta_R = \alpha + \theta$. Once again, we see that Kerr rotation is unique in its manifestation.

2.4.4 Classification of optical effects

We have classified every matrix element by the physical effect they have on linear polarization. They can be characterized by their action on linear polarization, which is summarized in Tab. 2.1, where $\theta_T = \theta_R - \alpha$ is the total rotation.

Name	Element	Rotation angle
Linear dichroism	δ	$\theta_T = -\delta \sin 2\alpha$
Linear birefringence	β	$\theta_T = -(\beta^2/2) \sin 4\alpha$
Circular dichroism	ε	$\theta_T = 0$
Circular birefringence	θ	$\theta_T = \theta$

Table 2.1: Classification of optical effects

What if we have several effects combined? We should expect to get a combination of the effects, for example, if both linear and circular dichroism are present, then we would expect total rotation to have the same $\sin 2\alpha$ harmonic; however, ellipticity would be modified. Indeed

$$\mathbf{E}' = \begin{pmatrix} 1+\delta & -i\varepsilon \\ i\varepsilon & 1-\delta \end{pmatrix} \begin{pmatrix} \cos\alpha \\ \sin\alpha \end{pmatrix} = \begin{pmatrix} (1+\delta)\cos\alpha - i\varepsilon \sin\alpha \\ (1-\delta)\sin\alpha + i\varepsilon\cos\alpha \end{pmatrix}$$

which, in a circular basis, reads

$$\boldsymbol{\mathcal{E}}' = O^{-1}\mathbf{E}' = \frac{1}{\sqrt{2}} \begin{pmatrix} 1 & -i \\ 1 & i \end{pmatrix} \begin{pmatrix} (1+\delta)\cos\alpha - i\varepsilon \sin\alpha \\ (1-\delta)\sin\alpha + i\varepsilon\cos\alpha \end{pmatrix}$$

Major axis orientation

$$\theta = \frac{1}{2}\arctan\frac{(1-\delta-\varepsilon)\sin\alpha}{(1+\delta-\varepsilon)\cos\alpha} + \frac{1}{2}\arctan\frac{(1-\delta+\varepsilon)\sin\alpha}{(1+\delta+\varepsilon)\cos\alpha} \approx \alpha - \frac{\delta}{1-\varepsilon^2}\sin 2\alpha.$$

Combining circular dichroism with linear optical activity does not lead to unexpected results.

2.4.5 Isotropic rotation as evidence for TRSB

Most importantly, the isotropic (i.e., α–independent) component of total rotation is only present when the θ matrix component is not zero. Let us demonstrate it. The most general form of reflection matrix without circular birefringence is $S = r_0 + r''\sigma_x + r'\sigma_z$, i.e., there is no term proportional to σ_y in the linear basis. Which is equivalent to $\Sigma = r_0 + r'\sigma_x + r''\sigma_y$.

$$S = \begin{pmatrix} r_0 + r' & r'' \\ r'' & r_0 - r' \end{pmatrix} \qquad \Sigma = \begin{pmatrix} r_0 & r' + ir'' \\ r' - ir'' & r_0 \end{pmatrix}$$

Here $2r_0 \equiv r_+ + r_- = r_{xx} + r_{yy}$, $2r' \equiv r_\pm + r_\mp = r_{xx} - r_{yy}$, and $r'' \equiv \frac{1}{2i}(r_{+-} - r_{-+}) = \frac{1}{2}(r_{xy} + r_{yx})$. The reflected polarization vector in the linear polarization basis is

$$\begin{pmatrix} \cos\alpha & \sin\alpha \end{pmatrix} S = \begin{pmatrix} (r_0 + r')\cos\alpha + r''\sin\alpha \\ r''\cos\alpha + (r_0 - r')\sin\alpha \end{pmatrix}^T$$

The same equation in circular polarization basis reads

$$\frac{1}{\sqrt{2}} \begin{pmatrix} e^{-i\alpha} & e^{i\alpha} \end{pmatrix} \Sigma = \begin{pmatrix} r_0 e^{-i\alpha} + r_\mp e^{i\alpha} \\ r_0 e^{i\alpha} + r_\pm e^{-i\alpha} \end{pmatrix}^T \equiv \begin{pmatrix} \alpha_+ \\ \alpha_- \end{pmatrix}^T$$

In order to find the orientation of the major axis, we need to compute

$$\frac{1}{2}\arg\left[\frac{\alpha_-}{\alpha_+}\right] = \frac{1}{2}\arg\left[\frac{r_0 e^{i\alpha} + r_\pm e^{-i\alpha}}{r_0 e^{-i\alpha} + r_\mp e^{i\alpha}}\right] = \alpha + \theta_T$$

Since it's a generic matrix and $r_0 \neq 0$, we can redefine $r_1 = r_\pm / r_0$ and $r_2 = r_\mp / r_0$; obviously, r_0 does not change optical activity since it's an overall factor that affects both polarizations equally.

$$\begin{aligned} \theta_T(\alpha) &= \frac{1}{2}\arg\left[\frac{1 + r_1 e^{-2i\alpha}}{1 + r_2 e^{2i\alpha}}\right] = \frac{1}{2}\arg\left[1 + r_1 e^{-2i\alpha}\right] - \frac{1}{2}\arg\left[1 + r_2 e^{2i\alpha}\right] \\ &= -\frac{1}{2}\arctan\left[\frac{|r_1|\sin(2\alpha - \phi_1)}{1 + |r_1|\cos(2\alpha - \phi_1)}\right] - \frac{1}{2}\arctan\left[\frac{|r_2|\sin(2\alpha + \phi_2)}{1 + |r_2|\cos(2\alpha + \phi_2)}\right] \end{aligned}$$

Here $r_{1,2} = |r_{1,2}|e^{i\phi_{1,2}}$ are arbitrary complex numbers for which it is reasonable to assume $|r_{1,2}| < 1$. Now we want to show that θ_T derived above has no isotropic component θ_C, in other words, we need to show that

$$\int_0^{2\pi} \theta_T(\alpha) d\alpha = 0$$

Indeed, we can expand the integrand in a Taylor series valid for $|r| < 1$, exchange the order of summation, and obtain an asymptotic series

$$\int_0^{2\pi} \arctan\left[\frac{|r|\sin\alpha}{1 + |r|\cos\alpha}\right] d\alpha = \sum_{m=1}^{\infty} (-1)^{m+1} \frac{|r|^m}{m} \int_0^{2\pi} \sin(m\alpha) d\alpha = 0.$$

This conclusion lets us use the isotropic component of polarization rotation as a test for magnetism in a crystal.

Next, we provide an alternative method for experimentally probing the same matrix element θ, responsible for the magneto-optical Kerr effect, also known as circular birefringence, by utilizing circular polarization instead of linear polarization.

Chapter 3

Sagnac interferometer

3.1 Design of Sagnac interferometer

The all-fiber design of zero-area loop Sagnac interferometer (ZALSI) used in the present thesis was invented by Xia *et al* [69, 1], who modified the previous design of Sagnac interferometer invented by Kapitulnik *et al* [70, 71, 72].

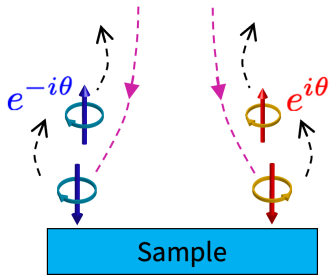

Figure 3.1: Circular birefringence

Over the last two decades, the ZALSI apparatus has proven itself to be an extremely sensitive magneto-optical measurement technique. It was used to detect ferromagnetism in ultra–thin films of $SrRuO_3$ [73], and inverse proximity effect in superconductor-ferromagnet structures [74]. Due to remarkably high shot–noise–limited sensitivity of 100 nrad/$\sqrt{\text{Hz}}$ ZALSI is even able to observe a time-reversal breaking superconducting order parameter in heavy–fermion materials Sr_2RuO_4 [75], $PrOs_4Sb_{12}$ [76], UPt_3 [77] and UTe_2 [78, 79].

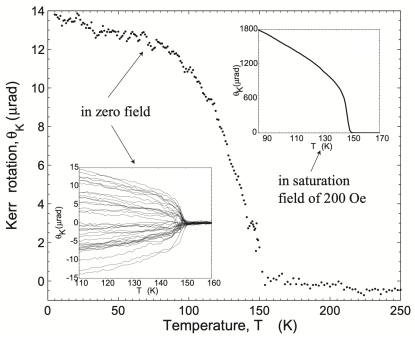

Figure 3.2: MOKE in $SrRuO_3$ [Xia *et al*, 2006]

At its core, the Sagnac interferometer measures the difference between the phases acquired by right and left circularly polarized light waves reflected from the sample (see Fig. 3.1). To create an interference pattern between the two waves, a non-monochromatic light source (superluminescent emitting diode) is used, which guarantees that only wave packets that traverse the same optical paths would interfere. The light is sent down a polarization-maintaining (PM) fiber with birefringence through a polarizer, which splits the light equally between the slow and fast axes of the fiber. Upon exiting the

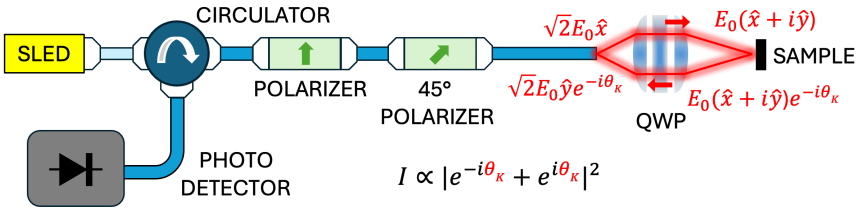

Figure 3.3: Core elements of Sagnac interferometer design.

fiber, light goes through a quarter-wave plate (QWP), oriented at 45° with respect to the axis of the fiber, which turns linearly polarized light into circularly polarized, and after reflection from the sample QWP converts circular polarization back into linear. The light traveling along the slow axis of the PM fiber on its way to the sample travels in the fast axis on its way back, and vice versa, because passing twice through the QWP is equivalent to passing through a half-wave plate (HWP). On the way back, light is projected on the single axis and sent into the photodetector, where two beams interfere. A simplified version of ZALSI is shown in Fig. 3.3 .

Significantly, because a broadband light source is used, a portion of light, which, after reflection, does not change its helicity (handedness), would not contribute to the interference pattern. Hence, optical rotations due to linear birefringence/dichroism are excluded by design.

Indeed, if, say, some part of the light beam traveling along the slow axis of the fiber gets reflected into the slow axis, then by the time it reaches the detector it would have acquired the phase $\varphi_{xx} = 2n_{\text{slow}}L$, where $L \simeq 5$ m is the distance between the 45° polarizer and the sample. Only the beams traveling along the time-reversal symmetric copies of each other's path and acquiring phase $\varphi_{xy} = n_{\text{slow}}L + n_{\text{fast}}L$ will interfere as guaranteed by the finite bandwidth of the source.

This incredible property could also be viewed as a consequence of the reciprocity of the apparatus: two light waves interfering at the detector can be considered time-reversal symmetric copies of each other as long as they interact with the sample in the same manner. In other words, to have a non-trivial interference term in the intensity at the detector, the sample must break time-reversal symmetry (TRS).

3.1.1 Extracting Kerr angle

To measure phase shift $2\theta_K$ induced by magneto-optical Kerr effect, we use an electro-optical modulator (EOM) to modulate the phase of the light passing through the slow axis of the fiber (see Fig. 3.4). Let the sample be described by some arbitrary reflection matrix S, which in the basis of

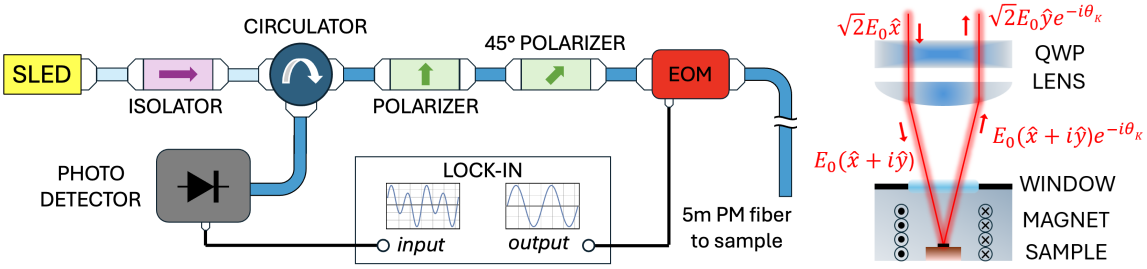

Figure 3.4: Schematics of the zero-area-loop fiber-optic Sagnac interferometer

circular polarizations has elements

$$\Sigma = \begin{pmatrix} r_+ & r_\mp \\ r_\pm & r_- \end{pmatrix} \qquad\qquad \theta_K = \frac{1}{2}\arg\left[\frac{r_-}{r_+}\right].$$

Then, the power at the detector (up to an overall factor) is given by

$$P = |r|^2 + 2|r_+ r_-|\cos 2\left[\theta_K - \phi_m \sin(\omega t + \delta)\right], \tag{3.1}$$

where the first term $|r|^2 \equiv |r_+|^2 + |r_\pm|^2 + |r_\mp|^2 + |r_-|^2$ is the total power without modulation and interference, while the second term comes from interfering two counter–propagating beams. Phase shift $\delta = (\omega - \omega_p)\frac{\tau}{2}$ is the phase acquired from traveling from EOM to the sample and back.

Modulation frequency ω and modulation amplitude ϕ_m in equation (3.1) are parameters of the waveform generator, which we are free to play with. We fix the modulation frequency to a proper value $\omega_p = \frac{\pi}{\tau} \simeq 10$ MHz determined by the time τ it takes the light to make the round trip (see the later section for details). In doing so, we minimize the contribution from the residual–amplitude modulation, which is ignored in the formulas above and below. Phase modulation amplitude ϕ_m is chosen to maximize $J_1(2\phi_m)$, which in turn maximizes signal-to-noise ratio.

Producing the Fourier decomposition of the signal (3.1), we split the signal into three main components:

$$\begin{aligned} P_0 &= |r|^2 + 2|r_+ r_-|J_0(2\phi_m), \\ P_\omega &= 4|r_+ r_-|\sin(2\theta_K)J_1(2\phi_m)\sin(\omega t + \delta), \\ P_{2\omega} &= 4|r_+ r_-|\cos(2\theta_K)J_2(2\phi_m)\cos(2\omega t + 2\delta). \end{aligned} \tag{3.2}$$

where J_1 and J_2 are Bessel functions. From here we see that the first harmonic P_ω is only present when $\theta_K \neq 0$, and the Kerr angle can be calculated as

$$\theta_K = \frac{1}{2}\tan^{-1}\left[\frac{J_2(2\phi_m)V_\omega^{\mathrm{RMS}}}{J_1(2\phi_m)V_{2\omega}^{\mathrm{RMS}}}\right], \tag{3.3}$$

which is independent of optical power or sample reflectivity. Here, $V_\omega^{\mathrm{RMS}} \propto P_\omega$ is the voltage reading on the lock-in amplifier. Finally, to maximize the signal-to-noise ratio, we set the modulation amplitude value ϕ_m and first lock-in phase δ such that the first harmonic is maximized when measured from a magnetic material.

3.2 Reciprocity

Reciprocity is the most essential property of the zero-area loop Sagnac interferometer. It follows from the finite bandwidth of the light source. We are using Thorlabs SLD1005S and SLD830S-A20 superluminescent diodes with finite bandwidth (see Fig. 3.5). As a result, when two wave packets

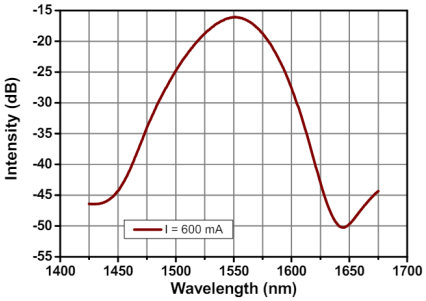

(a) SLD1005S ($\lambda = 1550$ nm)

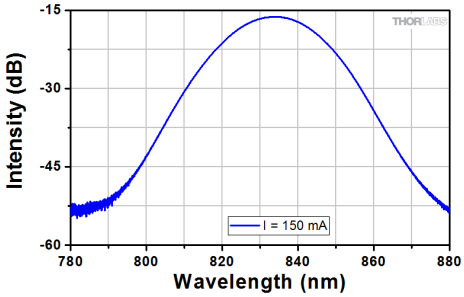

(b) SLD830S-A20 ($\lambda = 830$ nm)

Figure 3.5: SLED optical spectrum (from thorlabs.com)

with different optical frequencies are added together, the total intensity is given by the sum of individual intensities without the interference term. To illustrate this, we can consider the light as the sum of monochromatic components, where each component interferes with the element from the second source that has the same wavelength. Total intensity is given by the sum of individual intensities I_λ weighted with the correct distribution function, which could be, for simplicity, assumed to be Gaussian.

$$\begin{aligned} I &= \int (dk) \exp\left[-\frac{(k-k_0)^2}{2(\Delta k)^2}\right] \left|e^{ikz}E_{x1} + e^{ikz}E_{x2}e^{ik\Delta z}\right|^2 \\ &= |E_{x1}|^2 + |E_{x2}|^2 + 2\,\mathrm{Re}\,[E_{x1}E_{x2}^*] \int (dk) \exp\left[-\frac{(k-k_0)^2}{2(\Delta k)^2}\right] \cos k\Delta z \\ &= |E_{x1}|^2 + |E_{x2}|^2 + 2\,\mathrm{Re}\,[E_{x1}E_{x2}^*] \exp\left[-\frac{(\Delta z)^2(\Delta k)^2}{2}\right] \cos k_0\Delta z \end{aligned} \tag{3.4}$$

We see that for a significant enough difference in optical paths Δz, the interference term between two non-monochromatic waves dies out (this argument was copied from [3]).

Probably, a better way to model the same phenomenon is to consider a source which emits light

with a random phase $\phi(t)$ with zero average $\langle\varphi\rangle = 0$ and two-point correlator

$$\langle\varphi(t)\varphi(t+\tau)\rangle = e^{-\tau/\tau_\varphi}.$$

This means that the light emitted by such a source has roughly the same phase as long as the time passed between emission events is smaller than *coherence time* τ. When the intensity of the light is measured at the detector, it is averaged over a period much larger than τ, and as a result, the interference pattern is smoothed out.

$$\begin{aligned}\left\langle \left| e^{i\varphi(t_1)}E_{x1} + e^{i\varphi(t_2)}E_{x2} \right|^2 \right\rangle &= |E_{x1}|^2 + |E_{x2}|^2 + 2\,\mathrm{Re}\left[E_{x1}E_{x2}^*\right]\langle\cos\Delta\varphi\rangle \\ &= |E_{x1}|^2 + |E_{x2}|^2 \\ &\quad + 2\,\mathrm{Re}\left[E_{x1}E_{x2}^*\right]e^{-\frac{\Delta\varphi}{\phi\varphi}}\cos\Delta\varphi \\ &\approx |E_{x1}|^2 + |E_{x2}|^2, \quad \Delta\varphi \gg \phi_\varphi\end{aligned}$$

This model shows the same result as above in (3.4), however, it directly indicates the *temporal* nature of decoherence (as opposed to spatial decoherence).

3.2.1 Coherence time

The polarization-maintaining fiber used in the ZALSI, which works due to a birefringent core, namely Thorlabs PM1550-XP, has refractive indices of $n_y = 1.4492$ and $n_x = 1.4496$ along the fast and slow axes, respectively. Light traveling inside the core has a wavelength which is effectively shorter $\lambda_n = \lambda/n$, while frequency is the same as in vacuum. In our case, $\lambda = 1550$ nm and FWHM spectral width $\Delta\lambda = 50$ nm, the frequency of the light is about $f = \omega/2\pi = c/\lambda \simeq 200$ THz.

Since such a light wave packet consists of waves with different frequencies, which do not interfere with each other, such a wave packet has a finite coherence time τ_φ calculated as $\Delta\omega\tau_\varphi \sim 2\pi$ or $\Delta f\tau_\varphi \sim 1$. This time can be estimated from the following argument: if after time τ_φ wave components from the edge of the spectrum $\omega \pm \frac{\Delta\omega}{2}$ are single period apart, then the sum over all frequencies in between will average out to zero.

Similarly, one can define the coherence length $l_\varphi = v\tau_\varphi$. Since $\Delta f/f \approx \Delta\lambda/\lambda = \Delta\lambda_n/\lambda_n$ we can express coherence length and coherence time as

$$l_\varphi = \frac{\lambda^2}{n\Delta\lambda} = 33\ \mu\mathrm{m}, \qquad \tau_\varphi = \frac{\lambda^2}{c\Delta\lambda} = 160\ \mathrm{fs}.$$

Alternatively, we could also define phase difference, which leads to decoherence

$$\phi_\varphi = 2\pi\cdot\frac{f}{\Delta f} = 2\pi\cdot\frac{\lambda}{\Delta\lambda} \simeq 31\cdot 2\pi.$$

In our case, birefringence is $\delta n = 4.2 \cdot 10^{-4}$, so the two waves inside the core of the PM fiber will acquire a phase difference $\delta\phi = \phi_x - \phi_y \sim \phi_\varphi$ after traveling for

$$L = \frac{k}{\delta k} l_\varphi = \frac{n}{\delta n} l_\varphi = 3451 \cdot l_\varphi = \frac{\lambda^2}{\delta n \cdot \Delta\lambda} = 114 \text{ mm}.$$

This means we should always think about two perpendicular components traveling inside the fiber as decoherent wave packets. Let us now demonstrate it with a simple test.

3.2.2 Demonstration of decoherence

We perform a simple test by comparing two setups that would have resulted in the same outcome, assuming we had a monochromatic source. In scenario (a), we use a free-space 45° polarizer. In scenario (b), we use an input port EOM as an in-line polarizer, since the input and output ports have orientations of the PM fiber axis rotated by 45°.

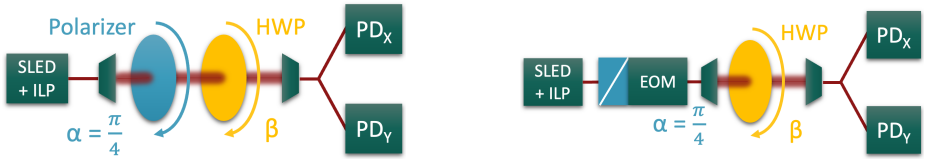

(a) Free-space polarizer. (b) In-line polarizer.

Figure 3.6: Decoherence demonstration setups

In scenario (a), after incoming light is equally split between the x and y axes, it travels through the air and then through a rotating half-wave plate. Orientation of HWP $\beta = 0$ corresponds to 22.5° between HWP major axis and polarizer orientation, hence intensities of x and y components follow

$$P_x = \frac{1}{2}(\sin 2\beta)^2, \qquad P_y = \frac{1}{2}(\cos 2\beta)^2$$

In scenario (b), the result should be the same for monochromatic light. However, in our setup, the coherence length is short. Consequently, light passing through the HWP consists of two decoherent, linearly polarized components that are perpendicular to each other and rotate together, resulting in no change in the intensity distribution, as seen in Fig. 3.7b.

This observation has an essential consequence: right and left circularly polarized light waves that hit the sample are decoherent; they do not add up to a single linearly polarized wave.

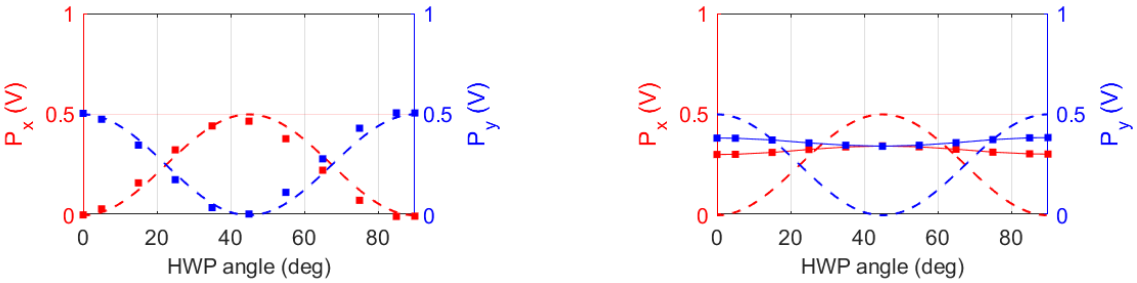

(a) Free-space polarizer (see Fig. 3.6a)

(b) In-line polarizer (see Fig. 3.6b)

Figure 3.7: Intensities of x and y components of the light

3.3 Proper modulation settings

In this section, we explain the rationale behind using a specialized set of modulation parameters and provide guidance on how to configure them in practice.

3.3.1 Residual amplitude modulation

A real-life electro-optical modulator not only modulates the phase, but also affects the amplitude, so that the change in polarization when light passes through the EOM is described by the Jones matrix (in linear polarization basis)

$$M_{\phi,\alpha} = \begin{pmatrix} (1+\alpha(t)) \cdot e^{i\phi(t)} & 0 \\ 0 & 1 \end{pmatrix} \qquad \begin{aligned} \phi(t) &= \phi_m \sin \omega t, \\ \alpha(t) &= a_m \sin \omega t. \end{aligned}$$

On the way from the circulator to the sample and back (see Fig. 3.4) light passes through EOM, QWP, reflects from the sample and then goes through QWP and EOM again, hence initial and final polarizations are related by Jones matrix $J = M_{\phi_2,\alpha_2} QO\Sigma O^{-1} Q M_{\phi_1,\alpha_1}$, where $\Sigma = O^{-1}SO$ is sample's reflection matrix in circular basis, and Q is the Jones matrix for the quarter-wave plate. Since

$$QO = \begin{pmatrix} 0 & 1 \\ i & 0 \end{pmatrix} \qquad O^{-1}Q = \begin{pmatrix} 1 & 0 \\ 0 & i \end{pmatrix} \qquad \Rightarrow \qquad QO\Sigma O^{-1}Q = \begin{pmatrix} r_\pm & ir_- \\ ir_+ & -r_\mp \end{pmatrix}$$

and for the total Jones matrix

$$J = \begin{pmatrix} (1+\alpha_1)(1+\alpha_2) e^{i\phi_1} e^{i\phi_2} r_\pm & i(1+\alpha_2) e^{i\phi_2} r_- \\ i(1+\alpha_1) e^{i\phi_1} r_+ & -r_\mp \end{pmatrix}$$

Here $\phi_1 = \phi(t)$ and $\phi_2 = \phi(t+\tau)$ correspond to two passes through the EOM. Since we use a broadband light source, only light waves with the same optical path will interfere; hence, the power at the detector is $P = |J_{11}|^2 + |J_{22}|^2 + |J_{12} + J_{21}|^2$.

Next, let us assume for simplicity that we're measuring reflection from a perfect mirror $r_\pm = r_\mp = 0$, $r_+ = r_- = -1$, then

$$P = 2 + 2\alpha_\Sigma + 2(1+\alpha_\Sigma)\cos(\phi_1 - \phi_2),$$
$$\cos(\phi_1 - \phi_2) = J_0(2\varphi_m) + 2J_2(2\varphi_m)\cos\left(2\omega_m t + (\omega_m - \omega_p)\tau\right) + \dots$$

Here we have ignored $\mathcal{O}(\alpha^2)$ compared to $\mathcal{O}(\alpha)$ and used notation $\alpha_\Sigma \equiv \alpha_1 + \alpha_2$ since RAM enters the expression only as the sum

$$\alpha_\Sigma = a_m \sin\omega_m t + a_m \sin(\omega_m t + \omega_m \tau) = 2a_m \sin\left(\omega_m t + \frac{\omega_m\tau}{2}\right)\cos\frac{\omega_m\tau}{2}.$$

Decomposition into Fourier components gives us a modified version of Eq. (3.2)

$$\begin{aligned} P_0 &= 2 + 2J_0(2\varphi_m) \\ P_1 &= \left[1 + 2J_2(2\varphi_m) + [1 + 2J_0(2\varphi_m)]\right]\alpha_\Sigma \\ P_2 &= 4J_2(2\varphi_m)\cos\left(2\omega_m t + (\omega_m - \omega_p)\tau\right) \end{aligned}$$

Note that product $\cos(\phi_1 - \phi_2)\alpha_\Sigma = J_0(2\varphi_m)\alpha_\Sigma + J_2(2\varphi_m)\alpha_\Sigma + \dots$ also contains a contribution to the first harmonic due to the product of the first and second harmonics.

We observe that residual amplitude modulation introduces a parasitic contribution to the first-harmonic signal, which contains the most significant information about Kerr rotation. Luckily, $\alpha_\Sigma \propto \cos\frac{\omega_m\tau}{2}$, so it can be minimized by selecting the right frequency $\omega_p = \pi/\tau$, called *proper frequency*.

3.3.2 Proper modulation frequency and amplitude

We have the freedom to choose the modulation frequency and amplitude. Reading at the detector with arbitrary modulation settings, for a material with a Kerr angle, ignoring RAM, looks like

$$\begin{aligned} P_0 &= |r|^2 + 2|r_+ r_-| J_0(2\varphi_m), \\ P_\omega &= 4|r_+ r_-| \sin(2\theta_K) J_1(2\varphi_m)\sin(\omega t + \delta), \\ P_{2\omega} &= 4|r_+ r_-| \cos(2\theta_K) J_2(2\varphi_m)\cos(2\omega t + 2\delta). \end{aligned} \tag{3.5}$$

with $\varphi_m = \phi_m \sin\frac{\omega_m\tau}{2}$. At the proper frequency $\varphi_m = \phi_m$, but in general this is not the case.

We have demonstrated that the exceptional value of modulation frequency $\omega_p = \pi/\tau$ minimizes RAM. It turns out that the same value also maximizes the second harmonic, since it maximizes

φ_m over ω_m. As can be seen from (3.3), maximizing second harmonic amplitude $V_{2\omega}$ maximizes sensitivity when converting ratio voltage to Kerr angle.

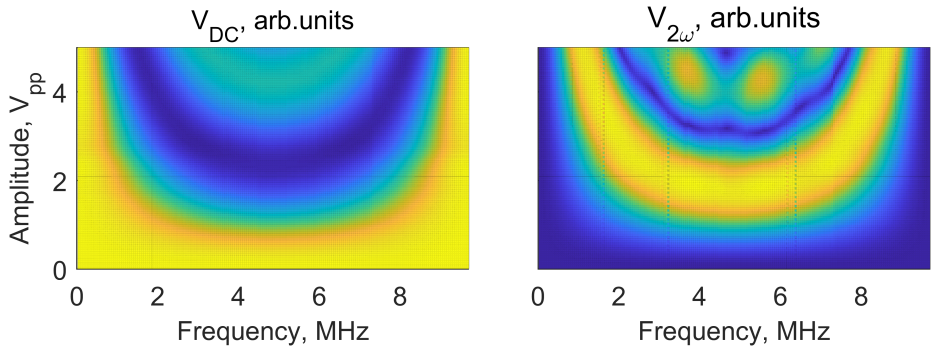

Figure 3.8: DC and 2nd harmonic signal as a function of modulation parameters

Similarly, choosing modulation amplitude ϕ_m such that $J_1(2\phi_m)$ is maximized leads to increased sensitivity of $V_{1\omega}$ to Kerr angle θ_K, which means that proper modulation amplitude should be defined as $\phi_p = \operatorname{argmax} J_1(2\phi_m)$. In practice, we would measure the first harmonic from the magnetic signal with a large θ_K and sweep the modulation amplitude until $V_{1\omega}$ is maximized.

As usually happens, in practice, measured data deviates from ideal formulas (3.5). Figure 3.8 is a false-color plot that shows how measured voltage is changing when modulation amplitude and frequency are varied. The yellow color corresponds to high values and the blue to smaller values; exact values are not shown, because they are only determined up to an oversampling factor. The Newport 1811 photodetector exhibits different sensitivities in the DC and AC channels, which are not accurately listed in the manual, as shown below. This means that the conversion coefficient from voltage to optical power is different for DC and AC signals. However, even if we can determine these coefficients, the overall optical power remains dependent on the input power and the insertion losses of many optical components. Therefore, for now, we will ignore this dependency and focus on the function's dependence on modulation parameters ω_m and ϕ_m.

One can see from Figure 3.8 that the DC signal V_0 (corresponding to $f \lesssim 100$ kHz) depends smoothly on modulation parameters and follows the predicted behavior quite nicely. The same cannot be said about the second harmonic magnitude $V_{2\omega}$. At high amplitude modulation, we clearly see that instead of a single maximum at $\omega_m \sim \omega_p \simeq 2\pi \cdot 5$ MHz, we get two maxima at $f_m \simeq 5 \pm 1$ MHz. The same effect is present at modulation amplitudes closer to the optimal value $\phi_p \simeq 1$ V_{pp}, yet it is not visible on this scale.

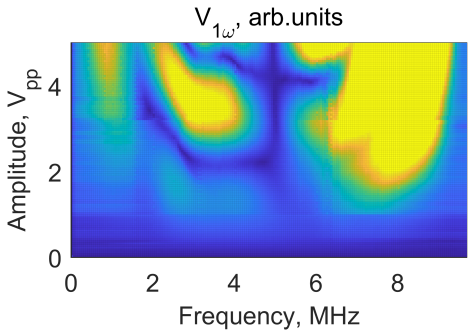

Figure 3.9: RAM (1st harmonic) as a function of modulation parameters

Most interesting is the behavior of the first harmonic.

Figure 3.9 shows the value of $V_{1\omega}$ measured from a non-magnetic aluminum sample, i.e., a perfect mirror without the Kerr effect. While there is a clear minimum at $\omega = \omega_p$, there is no apparent symmetry in frequency around ω_p.

In practice, to find the proper frequency and modulation, it's more practical to iteratively produce one-dimensional sweeps with all but one modulation parameter fixed. We typically start by choosing a modulation amplitude close to $\frac{1}{3}V_\pi$, as specified in the EOM manual. Then, we sweep the frequency ω_m and record the DC signal using the corresponding output of the photoreceiver, and demodulate the 1ω and 2ω harmonics. The obtained data should be fitted to

$$P_0(\phi_m, \omega_m) - P_0(0,0) = A_0 \left[J_0 \left(2\phi_m \sin \frac{\omega_m}{\omega_p} \right) - 1 \right], \tag{3.6}$$
$$P_2(\phi_m, \omega_m) = A_2 J_2 \left(2\phi_m \sin \frac{\omega_m}{\omega_p} \right)$$

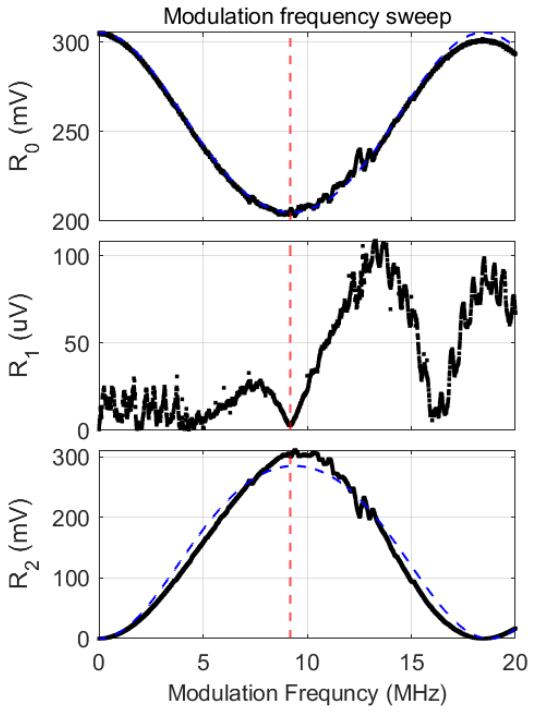

Figure 3.10: Modulation frequency sweep

Here, $P_0(0,0)$ is DC power/voltage in the absence of modulation. In principle, responsivities A_0 and A_2 are specified in the photodetector's manual; however, in practice, their ratio never matches the official value. Hence, they should be fitted as two independent parameters. Modulation amplitude ϕ_m should also be used as a fitting parameter shared between DC and $2f$ signals. As a result, the proper frequency can be determined, which is roughly equal to 5 MHz for a 10 m fiber and 10 MHz for a 5 m fiber connecting the EOM and free-space collimator.

The first harmonic, as measured from non-magnetic material, contains information mostly about RAM, which is minimized at the proper frequency. As seen from Fig. 3.10, there is a special frequency at which the first harmonic is minimized and the second harmonic is maximized at the same time. Raw data is shown in black; the blue dashed line represents the fit, and the red dashed line indicates the proper frequency. Furthermore, the maximum of the second harmonic corresponds to the minimum of the DC component magnitude R_0. This illustrates conservation of energy: as frequency is swept, energy is converted from DC to AC. Fig. 3.10 can be viewed as a one-dimensional slice of Fig. 3.8 along the line of fixed modulation amplitude.

Once the proper frequency is found, the next step is to sweep the amplitude while holding ϕ_m

fixed. Once again, the Fourier components of intensities are given by (3.6), while the first harmonic contains garbage when measured from the mirror. The data shown in Fig. 3.11 was recorded from magnetized materials: Co-based and Fe-based heterostructures. As a result, the first harmonic follows

$$P_1 = A_1 J_2 \left(2\phi_m \sin \frac{\omega_m}{\omega_p} \right).$$

Similarly to the plot above, raw data in Fig. 3.11 is shown in black; the blue dashed line represents the fit.

Coefficient A_1 contains information about the Kerr signal. However, it is also proportional to the overall intensity; therefore, it's more practical to look at the ratio A_1/A_2, which does not depend on sample reflectivity or input laser power. In practice, it is sufficient to select a single value of modulation amplitude and measure the power at the detector as a function of other external parameters (e.g., magnetic field). Proper modulation amplitude is picked to correspond to the maximum of the first harmonic (red dashed line).

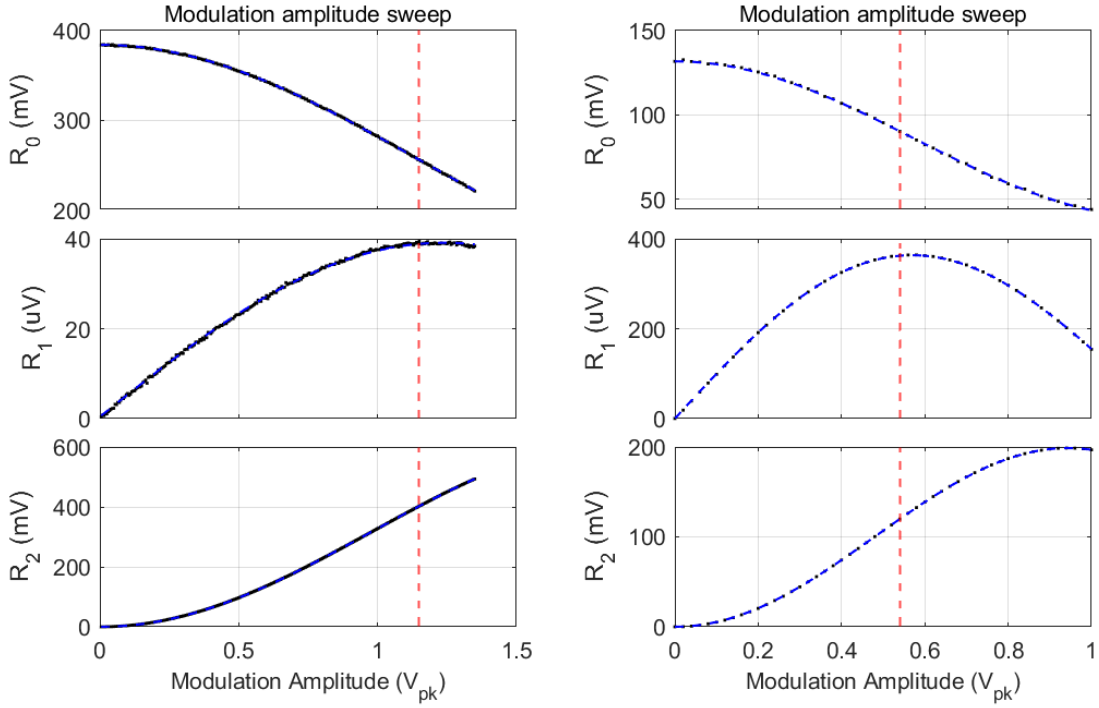

(a) Proper amplitude is reached at $V_{\text{pk}} = 1.14$ V. $\lambda = 1550$ nm.

(b) Proper amplitude is reached at $V_{\text{pk}} = 0.54$ V. $\lambda = 830$ nm.

Figure 3.11: Modulation amplitude sweeps.

3.3.3 Proper phase

Finally, the signal-to-noise ratio could be improved if the proper phase of the lock-in amplifier is set. As seen from Eq. 3.3.1, the parasitic RAM signal is out of phase with the true magnetic Kerr signal. If we choose the phase of the lock-in such that the Kerr signal is in-phase, then RAM will be in quadrature. This way, we minimize sensitivity to RAM when we use the in-phase component to calculate the Kerr angle.

To set the proper phase, one can find a paramagnetic or diamagnetic material, such as glass, and measure $X_{1\omega}$ and $Y_{1\omega}$ as a function of the external magnetic field. When the lock-in phase is set correctly, only $X_{1\omega}$ would change with the field, while $Y_{1\omega}$ doesn't respond to it.

Note that several factors can reverse the sign of the Kerr angle: rotating the QWP by 90 degrees, changing the phase of the lock-in by 180 degrees, or modulating the fast axis instead of the slow axis. Therefore, the sign should be determined experimentally. The easiest test is to measure the Kerr (Faraday) effect from the glass (e.g., fused silica or N-BK7). It is known that glass has a negative Verdet constant over a wide range of wavelengths, with a larger magnitude for shorter wavelengths ($V \sim \lambda^{-1}$). Of course, the sign of the magnetic field needs to be determined first.

Alternatively, one could use a known ferromagnet. However, this is not the best option. Even though remanent magnetization is always aligned in the direction of the training field, Kerr rotation could be both parallel and anti-parallel to magnetization $\theta_K \sim \mathrm{Im}\,\sigma_{xy} \sim \pm M_z$.

3.4 RMCD-ZALSI

Is it possible to use a zero area loop Sagnac interferometer to measure circular dichroism instead of circular birefringence? Is it possible to build an apparatus that would be as good for the detection of TRSB as Sagnac is? Such a machine could be used for detecting TRSB, as circular dichroism in reflection can only appear due to magnetism. In transmission, naturally active optical media demonstrate circular dichroism without the need for magnetism.

Since the only difference between Kerr angle and Kerr ellipticity is that the former affects phase and the latter affects amplitude, it would be natural to assume that using an amplitude modulator instead of a phase modulator would bring the desired outcome. Indeed, since the rest of the ZALSI design is left untouched, such an apparatus would possess the same reciprocity property and would neglect all non-magnetic signals. Thus, such a modification of ZALSI would only be sensitive to reflecto-magnetic circular dichroism (RMCD). Let us analyze such a system from the point of Jones' calculus.

3.4.1 Jones analysis

The Jones matrix is $J = M_2QSQM_1$ with the modulation matrix being determined by two parameters: insertion loss α_0 and modulation amplitude α_m.

$$M_i = \begin{pmatrix} 1 & 0 \\ 0 & \alpha_0 + a_i(t) \end{pmatrix} \qquad \begin{aligned} a_1(t) &= \alpha_m \sin \omega_m t, \\ a_2(t) &= \alpha_m \sin \omega_m (t+\tau). \end{aligned}$$

Here, α_0 is at most $1/2$ when the modulator is biased at the Q point and has no insertion loss. In practice, $\alpha_0 \approx 1/4$ due to high insertion loss. We could also make it very small $\alpha_0 \approx \alpha_m$ if we bias the intensity modulator at the minimum of the transfer function. Of course, the modulation amplitude and frequency output of the waveform generator should be redefined to account for frequency doubling. For now, we will keep α_0 as a parameter.

Following a procedure similar to conventional ZALSI, we can simplify the resulting Jones matrix to

$$J = \begin{pmatrix} \sigma_{21} & i(\alpha_0 + a_1)\sigma_{22} \\ i(\alpha_0 + a_2)\sigma_{11} & -(\alpha_0 + a_1)(\alpha_0 + a_2)\sigma_{12} \end{pmatrix}$$

where σ_{ij} are the elements of the Sample Jones matrix in circular basis.

Finally, in order to get the resulting amplitude, we should multiply matrix J by $n_{\frac{\pi}{4}} = \frac{1}{\sqrt{2}}(1,1)$ to account for the polarizers, which is equivalent to summing all the elements in the matrix J. However, not every wave will interfere with every other one. Since phase difference that J_{11} and J_{22} acquired is larger than decoherence phase, only J_{12} and J_{21} will interfere.

The intensity detected at the photo diode is

$$\begin{aligned} I &= |J_{11}|^2 + |J_{22}|^2 + |J_{12} + J_{21}|^2 \\ &= |\sigma_{21}|^2 + (\alpha_0 + a_1)^2(\alpha_0 + a_2)^2|\sigma_{12}|^2 + |(\alpha_0 + a_2)\sigma_{11} + (\alpha_0 + a_1)\sigma_{22}|^2 \\ &= |\sigma_{21}|^2 + (\alpha_0^2 + \alpha_0 a_+ + a_1 a_2)^2|\sigma_{12}|^2 + |(\alpha_0 + \tfrac{1}{2}a_+)(\sigma_{11} + \sigma_{22}) - \tfrac{1}{2}a_-(\sigma_{11} - \sigma_{22})|^2 \end{aligned}$$

Here, we used a simple identity

$$\begin{aligned} a_2\sigma_{11} + a_1\sigma_{22} &= \tfrac{1}{2}(a_1 + a_2)(\sigma_{11} + \sigma_{22}) + \tfrac{1}{2}(a_1 - a_2)(\sigma_{22} - \sigma_{11}) \\ &\equiv \tfrac{1}{2}a_+(\sigma_{11} + \sigma_{22}) - \tfrac{1}{2}a_-(\sigma_{11} - \sigma_{22}) \\ &\equiv \tfrac{1}{2}a_+\sigma_\Sigma - \tfrac{1}{2}a_-\sigma_\Delta \end{aligned}$$

Expanding the brackets and ignoring higher-order contributions, we can rearrange the resulting

power by combining the same harmonics.

$$\begin{aligned} I = {} & |\sigma_{21}|^2 + \alpha_0^2|\sigma_+|^2 + \alpha_0^4|\sigma_{12}|^2 + \\ & + 2\alpha_0^3 a_+|\sigma_{12}|^2 + \alpha_0 a_+|\sigma_+|^2 - \alpha_0 a_- \operatorname{Re}\left[\sigma_+\sigma_-^*\right] \\ & + \alpha_0^2(a_+^2 + 2a_1a_2)|\sigma_{12}|^2 + \tfrac{1}{4}a_+^2|\sigma_+|^2 + \tfrac{1}{4}a_-^2|\sigma_-|^2 - \tfrac{1}{2}a_+a_- \operatorname{Re}\left[\sigma_+\sigma_-^*\right] \\ & + \mathcal{O}\big(\alpha_m^3\big) + \mathcal{O}\big(\alpha_m^4\big) \end{aligned}$$

Furthermore, we introduce some shorthand notation for brevity

$$\begin{aligned} a_+ \equiv a_1 + a_2 &= 2\alpha_m \cos\frac{\omega_m\tau}{2} \sin\left(\omega_m t + \frac{\omega_m\tau}{2}\right), \\ a_- \equiv a_1 - a_2 &= 2\alpha_m \sin\frac{\omega_m\tau}{2} \cos\left(\omega_m t + \frac{\omega_m\tau}{2}\right), \\ a_1^2 + a_2^2 &= \alpha_m^2 - \alpha_m^2 \cos\omega_m\tau \cos\left(2\omega_m t + \omega_m\tau\right), \\ a_+a_- = a_1^2 - a_2^2 &= \alpha_m^2 \sin\omega_m\tau \sin(2\omega_m t + \omega_m\tau), \\ 2a_1a_2 &= \alpha_m^2 \cos\omega_m\tau - \alpha_m^2 \cos\left(2\omega_m t + \omega_m\tau\right). \end{aligned}$$

Assuming $\sigma_{11} = \sigma_{22} \neq 0$ and $\sigma_{12} = \sigma_{21} = 0$ (perfect mirror)

$$\begin{aligned} I_{\mathrm{DC}} &= \alpha_0^2|\sigma_\Sigma|^2, \\ I_{1\omega} &= \alpha_0 a_+|\sigma_\Sigma|^2 \\ &= 2\alpha_0\alpha_m \cos\frac{\omega_m\tau}{2} \sin\left(\omega_m t + \frac{\omega_m\tau}{2}\right)|\sigma_\Sigma|^2, \\ I_{2\omega} &= \tfrac{1}{4}(a_+^2 - \langle a_+^2\rangle_t)|\sigma_\Sigma|^2 \\ &= -\tfrac{1}{2}\alpha_m^2 \cos^2\frac{\omega_m\tau}{2} \cos\left(2\omega_m t + \omega_m\tau\right)|\sigma_\Sigma|^2. \end{aligned}$$

We define proper frequency as before: $I_{1\omega}$ is minimized when reflection is measured from the mirror. We find $\omega_p = \frac{\pi}{\tau}$ so that $\omega_m\tau = \pi\frac{\omega_m}{\omega_p}$.

3.4.2 Circular dichroism parametrization

Let us introduce parametrization

$$\frac{\sigma_{22}}{\sigma_{11}} = \frac{1-\tan\varepsilon}{1+\tan\varepsilon}e^{2i\theta} = \tan\left[\frac{\pi}{4} - \varepsilon\right]e^{2i\theta} \approx 1 + 2i(\theta + i\varepsilon) \qquad \varepsilon, \theta \in \mathbb{R}.$$

Here, θ is the Kerr angle, and ε is circular dichroism; of course, the two are intimately related to each other through the Kramers-Kronig equations. Equivalently, we can set $\sigma_{11} = \frac{\sigma_0}{2}(1+\tan\varepsilon)e^{-i\theta}$

and $\sigma_{22} = \frac{\sigma_0}{2}(1 - \tan\varepsilon)e^{i\theta}$, with $\sigma_0 > 0$ then

$$\begin{aligned}
\sigma_\Sigma &= \sigma_0(\cos\theta - i\sin\theta\tan\varepsilon) \approx \sigma_0(1 - i\varepsilon\theta),\\
\sigma_\Delta &= \sigma_0(\cos\theta\tan\varepsilon - i\sin\theta) \approx \sigma_0(\varepsilon - i\theta),\\
\mathrm{Re}\left[\sigma_\Sigma\sigma_\Delta^*\right] &= \sigma_0^2\tan\varepsilon.\\
\mathrm{Im}\left[\sigma_\Sigma\sigma_\Delta^*\right] &= \frac{\sigma_0^2}{2}(1 - \tan\varepsilon)\sin 2\theta.\\
\mathrm{Re}\left[\frac{\sigma_\Sigma\sigma_\Delta^*}{|\sigma_\Sigma|^2}\right] &= \frac{\tan\varepsilon}{\cos^2\theta + \sin^2\theta\tan^2\varepsilon} \approx \frac{\tan\varepsilon}{\cos^2\theta} \approx \tan\varepsilon.
\end{aligned}$$

Suppose that circular dichroism is present $\varepsilon \neq 0$, then the first harmonic has two contributions.

$$I_{1\omega} = 2\alpha_0\alpha_m\cos\frac{\omega_m\tau}{2}\sin\left(\omega_m t + \frac{\omega_m\tau}{2}\right)|\sigma_+|^2 - 2\alpha_0\alpha_m\sin\frac{\omega_m\tau}{2}\cos\left(\omega_m t + \frac{\omega_m\tau}{2}\right)\mathrm{Re}\left[R_{++}R_{--}^*\right]$$

and $\mathrm{Re}\left[R_{++}R_{--}^*\right] = R_0^2\tan\varepsilon$. The quantity that we would use to extract circular dichroism could be chosen as

$$\frac{I_{1\omega,X}^{\mathrm{RMS}}(\omega_m = \omega_p)}{I_{1\omega,R}^{\mathrm{RMS}}(\omega_m = 2\omega_p)} = -\frac{\mathrm{Re}\left[\sigma_\Sigma\sigma_\Delta^*\right]}{|\sigma_\Sigma|^2}$$

Here, I^{RMS} is the root-mean-square (RMS) lock-in reading of the intensity at the photodetector. The sign is due to the fact that the fast axis is modulated, rather than the slow axis. There are many other reasons for the sign to flip, such as QWP orientation.

Since the phase is not guaranteed to be precisely zero even at multiples of proper frequencies, we have to find the proper phase at $\omega_m = \omega_p$ empirically. For the value of the first harmonic at $\omega_m = 2\omega_p$, we can use the magnitude.

3.4.3 Tests

In order to see if this idea works, we build the system and measure hysteresis in 70 nm thick $Li_{0.5}Al_{1.0}Fe_{1.5}O_4$ (LAFO) sample, which suits our needs well since it has low coercivity and relatively large magneto-optical signal at room temperature. Remarkably, this sample is an example of a ferromagnet with the Kerr sign opposite to magnetization.

We observe hysteresis in both Kerr angle and Kerr ellipticity measurements. However, noise is much higher in the latter, about 20 μrad, which does not allow us to use this apparatus for real-life applications.

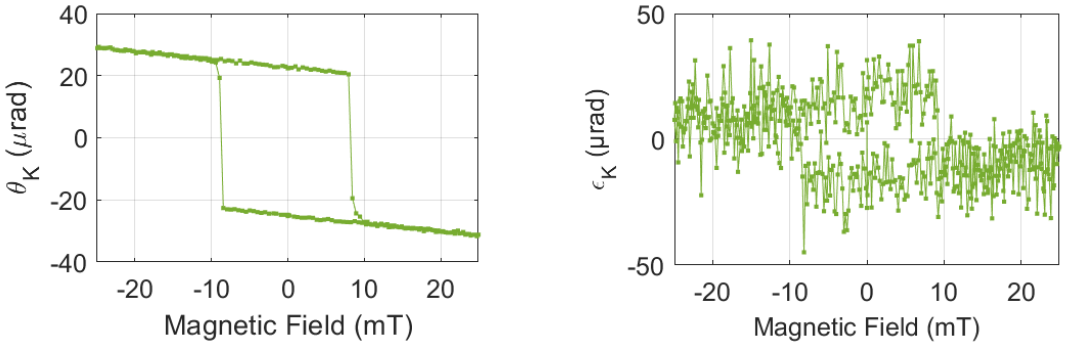

(a) Kerr angle in LAFO

(b) Kerr ellipticity in LAFO

Figure 3.12: Comparison of PM and AM ZALSI.

Chapter 4

Spin-glass state in nickelates

4.1 What is a spin-glass?

4.1.1 Exchange interaction

Typical ferromagnetic (e.g., Fe, Co, Ni) and antiferromagnetic (e.g., NiO, MnO) materials owe their properties to the exchange interaction between spins of unpaired electrons. Exchange interaction arises from the combination of the Pauli exclusion principle and the Coulomb repulsion. In metals, such as elemental iron or nickel, spins of itinerant electrons align due to the so-called Stoner mechanism [80, Ch. 12]. When electrons are localized, the energy of spin configuration can be succinctly described with the Heisenberg Hamiltonian

$$\mathcal{H} = -\sum_{i,j} J_{i,j} \mathbf{S}_i \cdot \mathbf{S}_j,$$

where $J_{i,j}$ is the so-called exchange interaction integral, whose value is determined by the overlap between neighboring electronic wavefunctions. It can be positive or negative depending on interatomic distances and electronic orbitals.

$$J_{i,j} = \iint U(\mathbf{r}_1 - \mathbf{r}_2)\psi_i(\mathbf{r}_1)\psi_i(\mathbf{r}_2)\psi_j(\mathbf{r}_2)\psi_j(\mathbf{r}_1)d\mathbf{r}_1 d\mathbf{r}_2$$

When $J > 0$, the spin-triplet state of ψ_1 and ψ_2 is more energetically favorable since it corresponds to an odd spatial wavefunction $\psi_{1,2}(\mathbf{r}_1, \mathbf{r}_2) = -\psi_{1,2}(\mathbf{r}_2, \mathbf{r}_1)$ and reduces Coulomb repulsion energy. However, in materials such as NiO, localized unpaired $3d$ Ni^{2+} electrons interact with each other through the $2p$ orbital of oxygen. This effectively leads to antiferromagnetic ($J < 0$) alignment of the spins in neighboring Ni atom electrons. Such indirect exchange interaction is known as *superexchange* and is typical for Mott insulators.

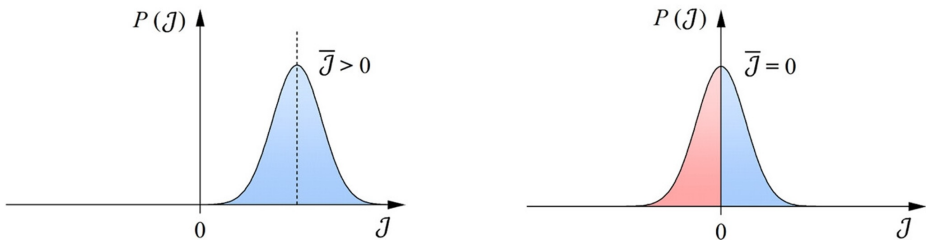

(a) Disordered ferromagnet (b) Spin–glass

Figure 4.1: Types of disorder in exchange interaction integrals [Mondal *et al*, 2024]

Another type of indirect magnetic coupling between localized spins is possible through the RKKY (Ruderman–Kittel–Kasuya–Yosida) mechanism. In a material such as $Cu_{1-x}Mn_x$ with $x \ll 1$, copper electrons form a delocalized electron band, which interacts with rare randomly distributed magnetic Mn atoms. These scattering events lead to spin polarization of itinerant electrons and modulate electronic density in a Friedel-like manner. As a result, neighboring Mn magnetic moments interact with each other through the sea of conduction electrons with effective exchange energy

$$J_{\mathrm{RKKY}} \sim \frac{\cos 2k_F r}{r^3}.$$

Since the distance between Mn atoms is random, the sign of $J_{i,j}$ fluctuates. As a result, such a system does not behave like a ferromagnet nor like an anti-ferromagnet; instead, it shows new emergent behavior known as *spin–glass* (e.g., see [81, 82] for modern examples).

4.1.2 Hallmarks of spin–glass

Spin-glasses demonstrate a plethora of peculiar phenomena (for reviews see [83, 84]).

Irreversible magnetization

First of all, magnetization in spin-glasses depends on how the system arrived at the thermodynamic state it is in. In Fig. 4.2, magnetization of $Fe_{0.5}Mn_{0.5}TiO_3$ measured during different protocols is shown [85]. In the first measurement (red circles), the sample is cooled down in zero field (ZFC), then the field is ramped up to 5 Oe, and magnetization is measured during the warmup. In the second experiment (blue circles), the sample is cooled down in a finite field $H = 5$ Oe (FC) and then the magnetization is

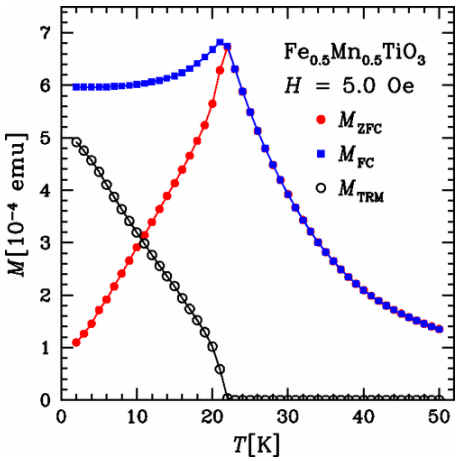

Figure 4.2: Magnetization in FeMnTiO [Katzgraber *et al*, 2007]

measured during warmup while the field is kept fixed.

For a typical paramagnet, magnetic susceptibility doesn't depend on cooling history, hence $M_{\mathrm{ZFC}}(T)$ and $M_{\mathrm{FC}}(T)$ curves would coincide. However, when a spin-glass system is cooled down through its transition temperature, spins freeze in different orientations depending on the applied field magnitude, leading to *irreversible magnetization*.

Thermo-remanent magnetization (TRM) can be measured with FC-ZFW protocol: cooldown in field, ramp the field down at base temperature, measure during warmup in zero field (black circles in Fig. 4.2). This result is akin to ferromagnetism; however, in spin-glass systems, the value of remanent magnetization depends on the magnitude of the cooling field, and the onset of magnetization $M_{\mathrm{TRM}}(T)$ at the freezing temperature is more gradual, not like a second-order transition.

Aging

The second most prominent hallmark of spin-glass is *slow time dynamics* of magnetization [86]. The reason the spin-glass system acquired its name is its resemblance to silica glass materials, which are known to flow very slowly under the pull of gravity. Similarly, in the spin-glass state, magnetization slowly changes as a function of time at the scales which can be measured in minutes, hours, or even days. This is nicely demonstrated in the following experiment.

Figure 4.3 presents experimental results on AgMn [84]. The sample was rapidly cooled in a field of $H = 0.1$ Oe from above T_g down to $T = 0.87T_g$, where it was held for a waiting time t_w. After this interval, the field was switched off and the subsequent relaxation was recorded as a function of the observation time t measured from the field cut-off. We see that magnetization is logarithmically slowly relaxing as a function of time. Amusingly, it turns out that the longer the wait time, the slower the relaxation. The inflection point of the relaxation curves systematically shifts to longer times with increasing t_w, consistently occurring around $t \approx t_w$. When the data are plotted versus the scaled variable t/t_w, the curves nearly collapse onto one another. This slow time relaxation behavior is known in the spin-glass dictionary as *aging*.

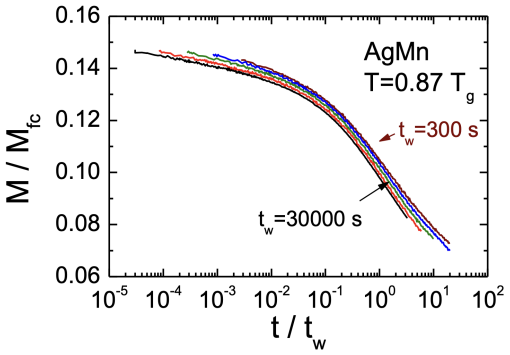

Figure 4.3: Aging in AgMn [Vincent *et al*, 1997]

Memory

Lastly, let us mention one more well-known, yet quite peculiar, property of spin-glasses. Low-frequency $f = 0.1$ Hz AC susceptibility χ measurements performed on $CdCr_{1.7}In_{0.3}S_4$ ($T_g = 16.7$

K) by Lefloch *et al* [87] revealed a new facet of spin-glasses: *memory effect*.

Figure 4.4 shows the results of measurement of dissipative part of susceptibility χ'' (responsible for relaxation) during a run in which the system was kept at $T = 12$ K during a time $t_1 = 350$ min just after the quench from above T_g, then the system was cooled down to $T = 10$ K and left for a time $t_2 = t_1$, and finally heated back to $T = 12$ K, and measured for another period of $t_3 = t_1$. On each of the three time intervals, clear aging behavior is observed. When the temperature is decreased by ΔT, a new aging process is started with a different relaxation rate and equilibrium asymptotic value from the one during the first time interval. However, when the temperature is raised back to $T = 12$, susceptibility χ'' immediately comes back to the quasi-equilibrium level reached before the temperature cycle. No new aging is observed. In the insert, the experimental data taken during t_1 and t_3 have been gathered and plotted vs. the total time spent at $T = 12$ K, and the curve looks incredibly smooth. This effect is interpreted as a memory: when the system is heated back to the previous temperature, it remembers all the dynamics that happened at this temperature before.

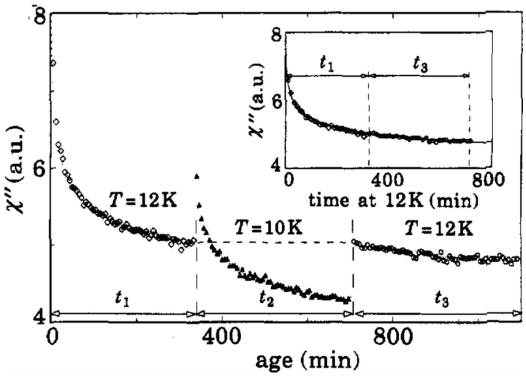

Figure 4.4: Memory in $CdCr_{1.7}In_{0.3}S_4$ [Lefloch *et al*, 1992]

4.1.3 Theory of spin glass

There are two main schools of thought on which physical principles govern the thermodynamics of spin-glasses: model of hierarchical free energy landscape pioneered by Parisi [88], and phenomenological droplet model developed by Fisher and Huse [89, 90]. There have been several attempts to experimentally determine which model is better at describing spin-glass state, such as AC susceptibility measurements in $CdCr_{1.7}In_{0.3}S_4$ of Lefloch *et al* [87] and mesoscopic resistance fluctuation experiments in CuMn of Weissman *et al* [91]. Both investigations concluded that observed phenomena are inconsistent with the droplet model, but can be understood within the picture of a hierarchical ground state. This evidence seems convincing to us and makes us believe that the droplet model does not capture the essential physics of spin-glass systems.

Even if there exists an explanation of the mentioned experiments within the droplet model, such an explanation must be very involved and should be disregarded according to Occam's razor principle. Furthermore, according to Dotsenko [92], some materials which exhibit spin-glass-like behavior may indeed be described by the droplet model; however, such systems should not be called spin-glass because they are in fact not a new phase of matter, but just a highly complex ferromagnet.

Finally, Parisi's model provides a clear, intuitive way to explain the experimental signatures of spin-glass, which is the main reason why we will concentrate on it.

Parisi's theory is based on Sherrington-Kirkpatrick's solvable model of spin glass [93]

$$\mathcal{H} = -\frac{1}{2}\sum_{i\neq j} J_{i,j}\mathbf{S}_i \cdot \mathbf{S}_j, \qquad S_i = \pm, \qquad \mathcal{P}(J_{ij}) \propto \exp\left[-\frac{(J_{ij}-J_0)^2}{2J^2}\right]. \tag{4.1}$$

This is an all-to-all mean-field-like Ising model with randomly distributed exchange integrals (see Fig. 4.1). Computation of disorder-averaged statistical sum within this model requires a mathematical manipulation called *replica trick* based on a simple identity $\ln Z = \lim_{n\to 0} \frac{1}{n}\left(Z^n - 1\right)$. Since averaging free energy $F = -T \ln Z$ over disorder is challenging, but averaging n non-interacting copies Z^n of the system is doable, fictional copies called replicas are introduced. The first solution obtained by Sherrington and Kirkpatrick was assumed to be replica symmetric. While it was successful at explaining the kink in susceptibility, it also led to non-physical negative entropy. A better approach was developed by Parisi, who found a replica symmetry-breaking solution of (4.1): instead of one amorphous equilibrium state, there are infinitely many nearly degenerate spin configurations.

Furthermore, it turns out free energy configurations at different temperatures are related through a hierarchical structure [92]. At temperatures above the freezing temperature $T > T_g$, the system is in a paramagnetic state. As the temperature is lowered, at each temperature $T < T_g$ many spin configurations appear with nearly degenerate energies separated by macroscopically large barriers. Minima of the free energy called *valleys* correspond to replica indices in Parisi's solution. As the temperature is lowered further, each valley is split into several mini-valleys, so that at low temperatures, there is a hierarchical structure of minima.

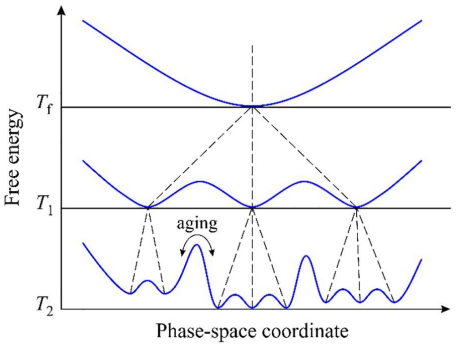

Figure 4.5: Hierarchical structure of free energy landscape [Kozelj *et al*, 2021]

This simple picture provides enough intuition to understand the physics behind spin-glass phenomena. Indeed, when the sample is cooled in an external magnetic field, the system falls into a different valley compared to a zero-field cooldown, since the field tilts the free energy $F(m)$ function. Naturally, susceptibility varies across different valleys, making it irreversible. Next, because free energy minima are nearly degenerate, when the field is turned on, the system 'tunnels' from one valley to the nearest one, which explains the aging phenomena. Lastly, due to the hierarchical structure, when the sample is cooled down, it falls into a new valley and 'rejuvenates', but when it's warmed back up, it falls back into the previous valley at a higher temperature, 'remembering' the previous state. Even if there were some field cycling at lower temperatures, the system would still fall into the same valley, since all nearby valleys are connected to a single one. Thus, we explained the memory effect as well.

4.2 Magnetism in infinite-layer nickelates

While the magnetic structure of infinite-layer nickelate superconductors is yet to be fully understood, particularly as it affects superconductivity, its most salient features are the absence of long-range AFM ordering and the freezing of spins into a glass phase even in the parent compound [24, 25, 26]. In the cuprates, magnetism originates from copper spins in the CuO_2 planes, which is also the starting point for models of the SG state [27]. By contrast, glassy dynamics observed in polycrystalline $LaNiO_2$ samples were attributed to the presence of subtle local oxygen disorder in the form of remaining apical oxygen [24].

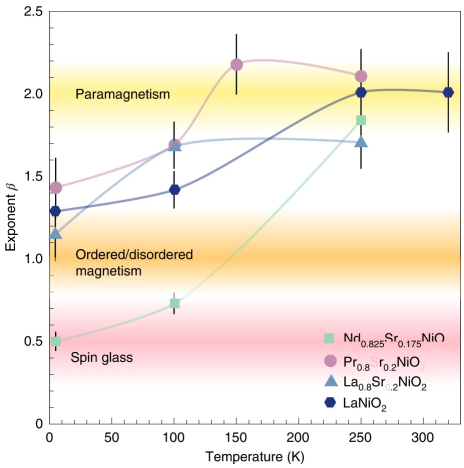

Figure 4.6: μSR study [Fowlie *et al*, 2022]

Because superconductivity has so far only been detected in thin-film nickelates, their associated magnetic states have not yet been established. A comprehensive muon spin-relaxation (μSR) study of $R_{1-x}Sr_xNiO_2$ by Fowlie *et al* [29] discovered intrinsic magnetism, which gradually onsets in the 100-150 K temperature range across the rare earth (R) series, and co-exists with superconductivity. The authors speculated that the observed glassy magnetic phase is intrinsic in nature and reflects the AFM coupling between the Ni^+ spins.

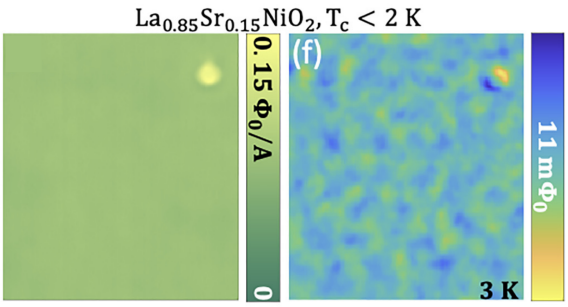

Figure 4.7: SQUID data [Shi *et al*, 2024]

On the other hand, scanning superconducting quantum interference device (SQUID) microscopy has picked up an inhomogeneous ferromagnetic background in $La_{0.85}Sr_{0.15}NiO_2$ slightly above the superconducting temperature, which has been attributed to extrinsic NiO_x particles on the interface between the nickelate and the $SrTiO_3$ capping layer [30].

Moreover, measurements of the magnetic excitations in $Nd_{1-x}Sr_xNiO_2$ using resonant inelastic x-ray scattering (RIXS) indicate strong spin-1/2 AFM paramagnons [23], while nuclear magnetic resonance (NMR) measurements observe short-range glassy antiferromagnetic fluctuations [22]. These dissimilar observations call for a better understanding of the relationship between magnetism and superconductivity in infinite-layer nickelate superconductors.

4.3 Magneto-optical Kerr effect measurements

4.3.1 Thin-film magneto-optics

Light beam experiences several reflections upon its optical path on each interface. However, the STO capping layer and substrate are transparent, while the nickelate layer is mostly transparent. It has a resistivity of $\rho \simeq 200$ μOhm*cm, which corresponds to a skin depth $\delta \simeq 50$ nm, much larger than the sample's thickness of $d \simeq 5$ nm. Overall, returned light is mainly composed of the light reflected from the bottom surface of the substrate with a small contribution from the metallic surface (see Fig. 4.8). As a result (in the absence of a magnetic field), the measured optical rotation consists mainly of a combination of two Faraday angles acquired upon propagation in two different directions.

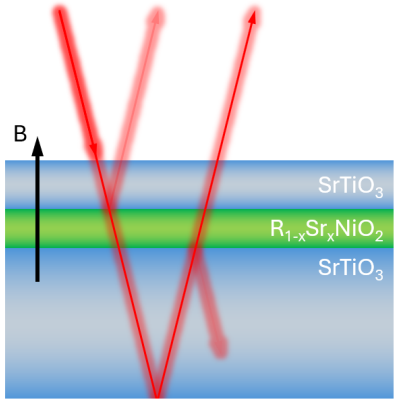

Figure 4.8: Schematic propagation of light

$$\theta_K^{\text{total}} \simeq \theta_F^{\swarrow} + \theta_F^{\nearrow}.$$

It is essential to highlight that the Faraday effect measured in transmission only can be present due to non-magnetic types of optical activities, such as birefringence or dichroism; however, a combination of two counter-propagating Faraday rotations has the exact symmetry as a Kerr angle [94]. The situation is more complicated, however, in the presence of an external magnetic field, since then the substrate contributes to the optical rotation as well.

As follows directly from Fresnel equations, Kerr and Faraday rotations are given by [95]

$$\theta_K = \text{Re}\left\{\frac{\sigma_{xy}}{\sigma_{xx}\left[1+4\pi i\sigma_{xx}/\omega\right]^{1/2}}\right\},$$
$$\theta_F = \frac{2\pi d}{c}\,\text{Re}\left\{\frac{\sigma_{xy}}{\left[1+4\pi i\sigma_{xx}/\omega\right]^{1/2}}\right\},$$

where d is the thickness of the material. The meaning behind this equation is simple: when electromagnetic wave propagates inside the media, it constantly "shakes" electrons, which in turn re–emit the light as radiation, however in the presence of magnetic moment, electron's orbital motion is curved (described by finite $\sigma_{xy}(\omega)$), which finally leads to rotation of polarization. Such optical activity is known as gyrotropy and is characteristic of many magnetic materials [62]. What is not generally simple is the relation between Hall conductivity $\sigma_{xy}(\omega)$ and magnetization M_z at optical frequencies, since it's determined by the exact structure of all the allowed optical transitions. In general, Hall conductivity $\sigma_{xy}(\omega)$ typically changes sign as a function of light energy (wavelength).

4.3.2 In–field MOKE measurements

All measurements performed in the presence of a magnetic field suffer from a background signal caused by the Faraday effect in optical elements along the light's path: quarter-wave plate, lens, and cryostat window all contribute to the measured MOKE value. This additional wavelength-dependent linear-in-field part of the signal can be estimated based on the Verdet constant of the material, the thickness of optical elements, and the magnetic field they experience. However, in practice, the magnetic field varies with distance from the cryostat, which results in a noticeable change in the measured signal even when the lens is moved by 1 mm, so it is easier to measure the contribution from optics by placing a mirror (non-magnetic reflecting material) next to the sample and measuring the signal from it.

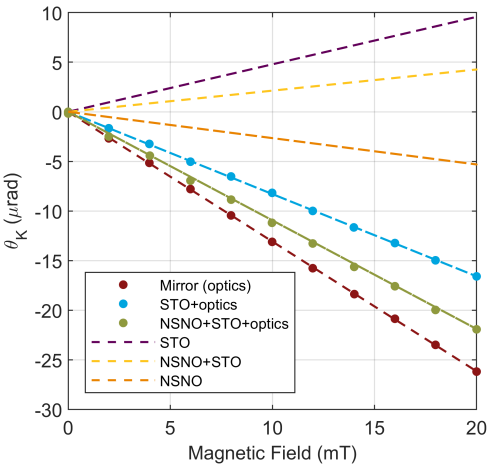

Figure 4.9: MOKE vs Magnetic Field

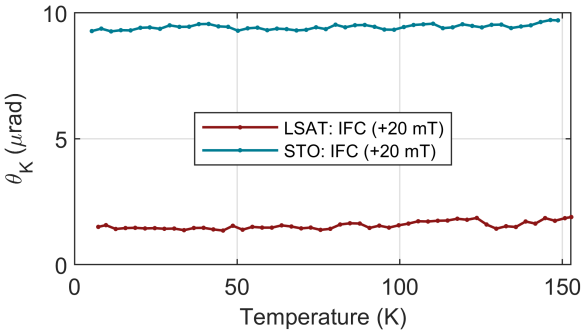

Figure 4.10: MOKE in STO and LSAT

Results of such calibration measurement performed on NSNO–on–STO sample, STO substrate, and mirror are shown on Fig. 4.9 . Magnetic field sweeps were performed at $T = 150$ K, where no history–dependent spin–glass dynamics is expected to be present. Kerr rotation measured off of the mirror comes fully from the Faraday rotation happening in the optical elements, and is as expected negative in positive field, due to negative Verdet constant of fused silica glass $V_{\text{glass}} \simeq 2.5$ rad·T^{-1}·m^{-1} at 1550 nm. Measurement of $SrTiO_3$ substrate results in a combination of positive paramagnetic-like contribution from the substrate and negative signal from the optics. Subtracting the value recorded off the mirror, we can isolate the Kerr rotation produced by the $SrTiO_3$ substrate. Finally, to separate the signal from the nickelate, we look at the difference between the Kerr signal detected from the sample and from the substrate. Due to several factors, including non-uniformity of the magnetic field around the optical components and the impact of the annealing procedure on the substrate, we do not expect the described subtraction procedure to yield perfect isolation of the signal from the sample. However, as seen from Fig. 4.10 , the signal from the substrate is constant in temperature, hence the contribution from the substrate only affects the overall constant background, which is not essential for the SG state analysis.

Furthermore, we repeat substrate measurement at a fixed applied magnetic field of +20 mT and sweep the temperature to obtain data presented on Fig. 4.10 . We observe almost no temperature dependence of the STO–induced Kerr signal, which lets us conclude that the observed glassy phase (Fig. 1 of the main text) is coming fully from the sample.

Lastly, let us emphasize that, unlike in-field measurement, running an experiment at $B = 0$ mT has no such drawbacks; hence, there is no need to perform a background subtraction for the zero-field warmup datasets.

Overall, magneto-optical Kerr effect measurements are ideally suited for studying magnetization in nickelate thin-film superconductors, since they allow for a local bulk probe (beam spot size ≈ 25 μm) of magnetization in a wide range of temperatures. However, due to the tiny absolute magnitude of the SG signal of ~ 5 μrad, this measurement is beyond the reach of conventional MOKE setups. In contrast, ZALSI is able to resolve such signals with ease owing to its extremely high sensitivity of 100 nrad/$\sqrt{\text{Hz}}$.

4.3.3 $La_{0.8}Sr_{0.2}NiO_2$

Figure 4.11 shows evidence for spin glass behavior in $La_{0.8}Sr_{0.2}NiO_2$ (LSNO). Figure 4.11a demonstrates the presence of spontaneous magnetization. Thermo-remanent magnetization (TRM) gradually emerges in LSNO below $T_{\text{onset}} \simeq 80$ K. When the sample is field-cooled in a small field of ± 20 mT and then the field is turned off at the base temperature $T_{\text{base}} \sim 5$ K, any remanent Kerr rotation is evidence for aligned magnetic moments in the material. Reversing the direction of the training field leads to the reversal of the sign of the Kerr signal, which confirms the magnetic nature of the optical signal. The observed smooth onset of the magnetic signal is characteristic of glassy systems.

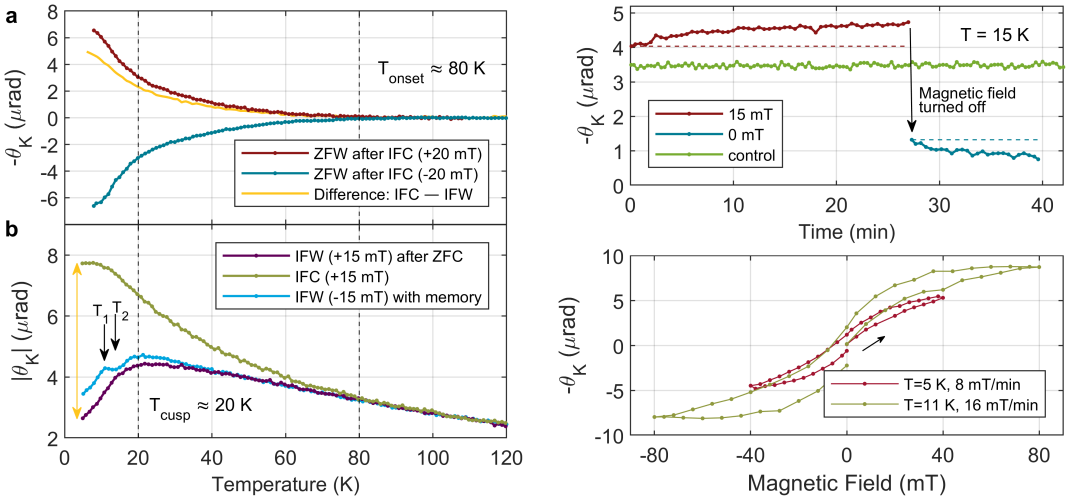

Figure 4.11: Kerr signal in $La_{0.8}Sr_{0.2}NiO_2$

In-field cooldown and warmup measurements (bottom panel of Fig. 4.11b) probe magnetic susceptibility, which appears to be irreversible: following a zero-field cooldown (ZFC), magnetic moments are frozen and cannot be rotated by a weak external field, while during the in-field cooldown (IFC), moments are aligned with the field. The difference between these two measured susceptibilities (IFW and IFC) is roughly the same as the remanent magnetization extracted during the measurement with the ZFW protocol, as shown by the yellow line on the top panel of Fig. 4.11a.

Irreversible behavior of magnetic susceptibility and gradual onset of magnetization are known properties of spin-glass; however, these could also be explained with domain physics alone. Thus, to verify the SG nature of magnetic state in nickelate superconductors, we further probe dynamical manifestations of SG phase.

After cooling the sample in zero-field from room temperature to T_{base}, we heat it to $T_2 = 15$ K, turn on a weak external field $B_z = +15$ mT, and record the Kerr signal as a function of time. As evident from Fig. 4.11c, magnetization slowly increases on the scale of minutes; this property of spin-glass is known as *aging*. Once the field is turned off, the magnetization slowly relaxes to some finite but smaller value on a similar time scale. The observed time-dependence of magnetic susceptibility is characteristic of glass-like spin dynamics and is comparable to analogous experiments performed on bulk polycrystalline $LaNiO_2$ samples [24, 25].

From T_2 we cool the sample down to $T_1 = 11$ K and perform a hysteresis loop by sweeping the field to +80 mT, then to −80 mT and back to zero. The resulting hysteresis curve is depicted in the inset of Fig. 4.11 d. Finally, we cool down to a base temperature of $T_0 = 5$ K, turn on an opposite field $B_z = -15$ mT and record the Kerr signal during in-field warmup, which exhibits a relatively sharp, non-monotonic features at $T_1 = 11$ and $T_2 = 15$ K (see Fig. 4.11b). This unusual effect can be explained as a manifestation of the 'memory', which happens because the system retains information about spin dynamics that was happening at T_1 and T_2 prior to cooldown. Above T_2, the magnetic susceptibility recovers the same trend that was recorded during the previous in-field warmup after zero-field cooldown. The hierarchical structure of the free-energy landscape with many local minima leads to apparent "memory" about the state from which the system was cooled down.

4.3.4 $Nd_{0.825}Sr_{0.175}NiO_2$

Finally, we direct our attention to measurements of $Nd_{0.825}Sr_{0.175}NiO_2$ (NSNO) samples prepared on $SrTiO_3$ and $(LaAlO_3)_{0.3}(Sr_2TaAlO_6)_{0.7}$ substrates, abbreviated as STO and LSAT, respectively (Fig. 4.12). It was shown that nickelate films prepared on LSAT substrate have higher crystallinity compared to the similar films fabricated on STO substrate [96, 97]. This is evident from the reduction in Ruddlesden-Popper-type stacking faults, improved metallicity, and an increase in the superconducting critical temperature (see Fig. 4.13) when compared to NSNO on STO [98].

Superconducting transition temperatures T_c in Fig. 4.13 (indicated with dashed lines) were determined as the mean of the inflection point temperature and the half-normal point temperature.

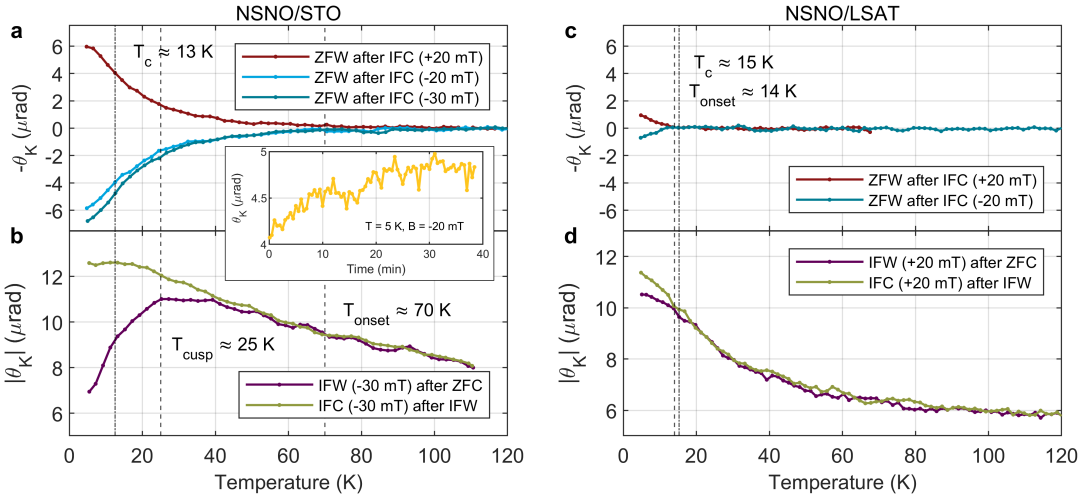

Figure 4.12: Kerr signal in $Nd_{0.825}Sr_{0.175}NiO_2$

The irreversible trend in Kerr susceptibility, together with the aging effect, undoubtedly demonstrates the glassy nature of magnetic order in $Nd_{0.825}Sr_{0.175}NiO_2$. Furthermore, the data explicitly demonstrates a significant difference in the strength of the magnetic signal between the two NSNO samples grown on different substrates, which we attribute to the difference in film quality as well as strain-epitaxy.

Specifically, the magnitude of the zero-field Kerr signal at base temperature drops from about 6 μrad to about 1 μrad. At the same time, the onset temperature is decreased to $T_{\text{onset}} \approx 13$ K in the NSNO/LSAT sample compared to $T_{\text{onset}} \approx 70$ K in the NSNO/STO. In fact, since the full strength of the magnetic signal in NSNO/LSAT is just $\theta_K^{(0)} \approx 850$ nanorad (see Fig. 4.12 c), we're unable to demonstrate the aging phenomenon in this sample. Based on the similar measurements in LSNO/STO and NSNO/STO samples, we would expect the aging magnitude $\theta_K(t = 30\text{min}) - \theta_K(t = 0)$ to be an order of magnitude smaller than $\theta_K^{(0)}$, which is below the resolution of our apparatus of 100 nanorads. Still, irreversible susceptibility and a gradual onset of the magnetic signal in zero-field measurements are indicative of a spin-glass state. We also note that in NSNO/LSAT samples, we observe only a single characteristic temperature at which the signal onsets, but we do not see cusp features in the susceptibility data.

4.4 Discussions

Our results of the dynamics of the magnetic state of doped thin-film nickelates are in good agreement with the magnetic susceptibility measurements of the polycrystalline parent compound $LaNiO_2$ [24, 25], which demonstrated similar hallmarks of SG phase: irreversible susceptibility, aging, and a memory effect. The authors of [24] have also identified two characteristic temperatures

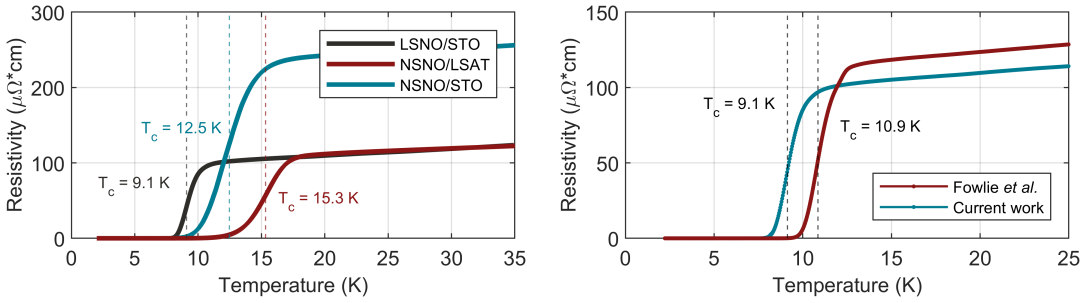

(a) Resistivity of LSNO and NSNO.

(b) Change of resistivity of LSNO over time.

Figure 4.13: Resistivity in $La_{0.8}Sr_{0.2}NiO_2$ and $Nd_{0.825}Sr_{0.175}NiO_2$

associated with SG behavior in the AC susceptibility of $LaNiO_2$: cusp-like peak feature around $T_{\text{cusp}} \simeq 13$ K and an onset of frequency-dependent susceptibility at $T_{\text{onset}} \simeq 85$ K. Approximate typical temperatures are summarized in the Table 4.1. Based on this observation, they surmised the possible existence of two disorder mechanisms at play with different characteristic energy scales.

However, it is challenging to estimate the exact SG emergence temperature due to the gradual nature of the transition. Based on T_{cusp} and the magnitude of the splitting between susceptibility curves, the magnetic signal in the thin films on the STO substrate appears to be comparable to the signal in the (undoped) nickelate crystals [24], which generally have lower crystallinity [28]. This similarity appears to be even more bizarre when it is taken into account that polycrystalline samples are reported to have no nickel impurities, while ~ 37 nickel particles per μm^2 have been reported in the thin-film samples [30]. In any case, the onset temperature of the SG phase does not depend strongly on the rare earth ion or Sr doping, which permits us to surmise the phase diagram shown in Fig. 6.1 .

Sample	T_c, K	T_{cusp}, K	T_{onset}, K
$LaNiO_2$ (polycrystal) [24]	-	13	85
$NdNiO_2$ (polycrystal) [24]	-	6	85
$La_{0.8}Sr_{0.2}NiO_2$ / STO	9.1	20	80
$Nd_{0.825}Sr_{0.175}NiO_2$ / STO	12.5	25	70
$Nd_{0.825}Sr_{0.175}NiO_2$ / LSAT	15.3	-	13

Table 4.1: Summary of the transition temperatures in nickelates

Importantly, present magneto-optical measurements agree with the μSR study [29], conducted on the same $La_{0.8}Sr_{0.2}NiO_2$ sample as measured in the current work. We speculate that the spin-glass magnetic order detected with ZALSI is responsible for the change in muon spin relaxation rate between $T = 100$ K and $T = 5$ K reported in Ref. [29]. Since μSR confirms the bulk nature of the magnetic signal, we conclude that the glassy spin dynamics is not caused by extrinsic factors such as Ni clusters on the interface with the capping layer, but instead arises due to intrinsic mechanisms.

However, in contrast to μSR, we can exclude the AFM interaction as the origin of the observed glassy magnetic state, since compensated AFM ordered moments would not produce any Kerr rotation.

Finally, we comment on the significant reduction in strength and characteristic temperature of the magnetic signal between the NSNO samples that are fabricated on STO and LSAT substrates. A relatively moderate increase by 20 % in superconducting temperature (see Fig. 4.13) indicates that the mechanism for "static" magnetism in nickelates is weakly related to superconductivity. Instead, it appears that the overall improvement in the sample's crystallinity is responsible for the suppressed SG state. Furthermore, as evident from the RIXS study of $PrNiO_2$, the paramagnon spectrum does not change between samples prepared on STO or LSAT substrates [99].

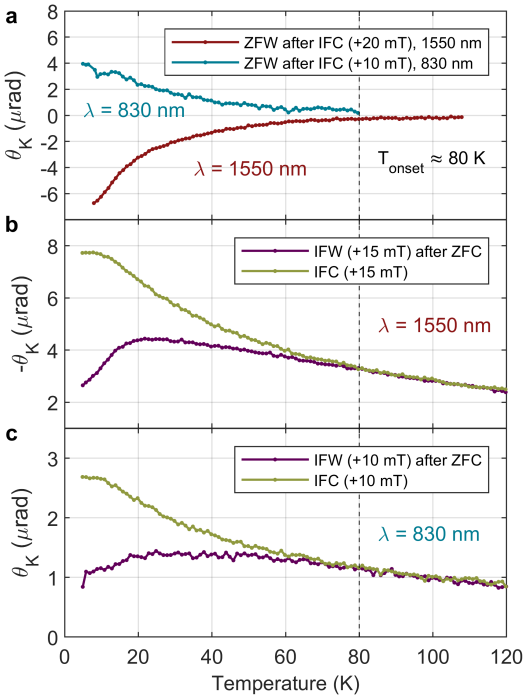

Figure 4.14: MOKE in LSNO at 1550 nm and 830 nm

4.4.1 Wavelength dependence

In our study, we used a light source operating at λ = 1550 nm SLED (0.8 eV) and at 830 nm (1.5 eV) ZALSI, and found qualitatively similar results. Notably, the Kerr rotation from the LSNO at 830 nm is reversed in sign and has a smaller magnitude compared to the signal detected at 1550 nm.

$$\theta_K^{\lambda=830\text{ nm}} \propto +M_z, \qquad \theta_K^{\lambda=1550\text{ nm}} \propto -M_z.$$

Moreover, for in-field measurements, paramagnetic-like contributions from the substrate are much larger at 830 nm. This makes longer wavelengths more suitable for studying magnetism in nickelate superconductors.

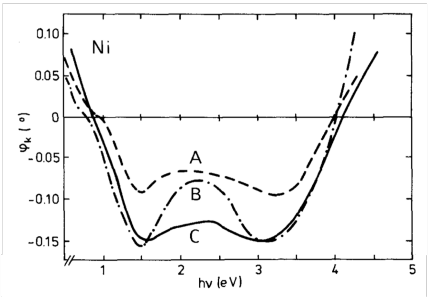

Figure 4.15: MOKE in elemental Ni [Buschow, 1988]

Observed behavior is, in fact, similar to elemental nickel, where the Kerr angle is known to reverse sign at $\omega \approx 1$ eV [100]. In Fig. 4.15, the MOKE in Ni below the Curie temperature, calculated within the DFT model by several different groups (A, B, C), is shown. This raises a question: Does the observed spin-glass behavior stem from elemental nickel inclusions that may be present due to fabrication imperfections?

4.4.2 Examination of NiO_x inclusions

To address the question of the effect of NiO_x inclusions on our measurements, we provide atomic force microscopy data in Fig. 4.16. In Ref. [30], NiO_x particles were found on the interface between infinite-layer nickelate and the capping STO layer, and the observed ferromagnetic signal was attributed to these particles. Specifically, the authors of Ref. [30] used STEM-EELS data to identify the particles and, using atomic force microscopy, found a typical density of 37.5 particles per μm^2. Each particle was clearly visible in the AFM as a 6 nm tall protrusion.

We present AFM scans of our samples, which show that the top surface of our LSNO/STO and NSNO/STO samples has a root-mean-square roughness of less than 1 nm. Fig. 4.16a is pasted from Ref. [30], while b and c correspond to LSNO/STO and NSNO/STO samples that were measured in the present work. The AFM images of infinite layer nickelates grown on $SrTiO_3$ substrate show a sufficiently low surface particle density to cause any potential background from NiO_x inclusions to be minimal. The planar density of surface particles is significantly lower than that reported in Ref. [30], given similar scan sizes in AFM images.

This evidence demonstrates that the current generation of thin-film infinite layer nickelate samples has a negligible concentration of NiO_x inclusions [96]. Thus, the measured optical magnetization is likely not due to disorder at the nickelate/capping layer interface.

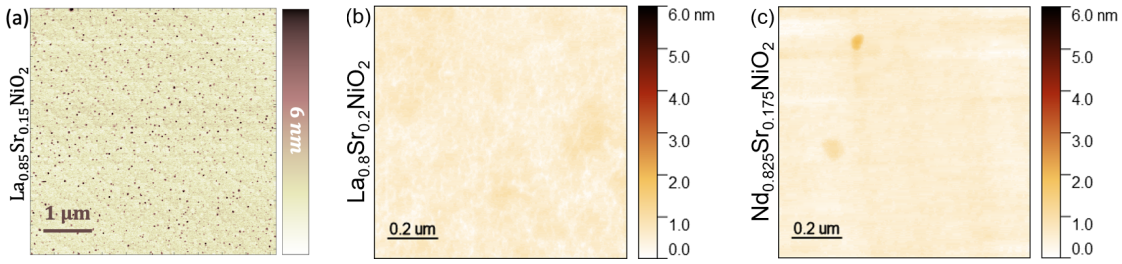

Figure 4.16: AFM scans of LSNO/STO and NSNO/STO

Chapter 5

Mystery of CsV_3Sb_5

5.1 Chaos of experimental data

5.1.1 Scanning tunneling microscope experiments

Since the observation of chirality switching of CDW-related STM peaks under the change of applied magnetic field in AV_3Sb_5 (A = Cs, Rb, K) [38, 39, 40], there has been active debate over whether the CDW hosts a chiral flux phase with orbital loop currents [35, 36, 37]. While the spatial chirality of STM peak arrangements is a purely geometric property and does not by itself imply magnetism, the fact that an external magnetic field can reversibly control chirality suggests coupling between the CDW order parameter and the field.

It is entirely possible that the CDW is by itself magnetic, in which case the role of the external magnetic field is in aligning magnetic order parameters across different domains. If this is indeed the case, observed STM CDW-peaks chirality switching should still be observed after the field is turned off. Unfortunately, none of the original experiments [38, 39, 40] and not even the consequent STM study in RbV_3Sb_5 [43], dedicated to the phenomenon of STM peaks chirality switching, have performed such experiments.

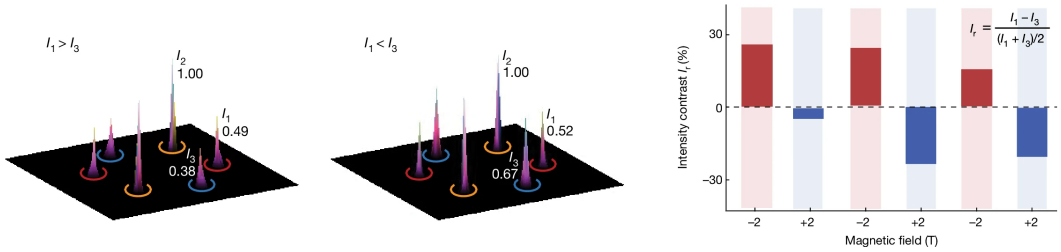

Figure 5.1: Chiral STM peaks in RbV_3Sb_5 [Xing *et al*, 2024]

If, instead, the chiral CDW response exists only in a finite magnetic field and vanishes when the field is ramped down, this behavior would not constitute evidence for time-reversal symmetry breaking (TRSB). Instead, it would point to an interplay between the sample's paramagnetism and the CDW.

Furthermore, an independent STM study of CsV_3Sb_5 with spin-polarized tips found no evidence of chirality switching or local magnetic moments [41], challenging chiral flux order interpretation. Similarly, another independent STM study of KV_3Sb_5 reported the absence of sensitivity of CDW peaks to magnetic field whatsoever [42].

Taken together, these considerations indicate that the observed STM chirality switching with high applied magnetic field in CsV_3Sb_5 is not a compelling signature of TRSB.

5.1.2 Muon spin relaxation experiments

Muon spin relaxation (μSR) experiments have also provided conflicting results. Studies of CsV_3Sb_5 observed enhanced internal magnetic fields below the CDW transition [44, 45] and interpreted it as evidence of TRSB. Similar μSR evidence for hidden magnetism was reported in ScV_6Sn_6 [46]. At the same time, μSR experiments on KV_3Sb_5 [47] attribute observed changes in relaxation rates at the CDW transition to nuclear rather than electronic fields, thus concluding that no evidence of TRSB is present.

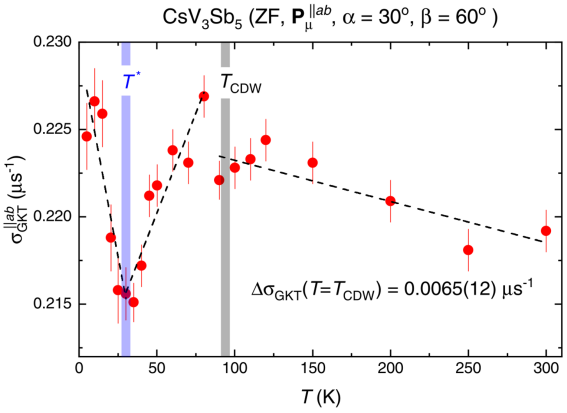

Figure 5.2: μSR rate in CsV_3Sb_5 [Khasanov *et al*, 2022]

It is an open question whether it is possible to separate the contribution to muon rotation from the nuclei and electrons. Typically, this is achieved by applying transverse and longitudinal magnetic fields. However, numerous experiments have shown that high magnetic fields significantly alter electronic behavior in a dramatic and not fully understood manner [58].

Without a clear separation between nuclear and electronic contributions, it is impossible to draw any conclusive statements about the onset of orbital magnetism at T_{CDW}. This is because, as nuclei move when CDW onsets, the same landing site in the crystal experiences different atomic magnetic fields.

5.1.3 Quasi-anomalous Hall effect

A series of transport measurements has revealed an appearance of non-linear-in-H behavior below the CDW transition in CsV_3Sb_5 and related compounds, which was interpreted as a precursor to

anomalous Hall effect (AHE) indicative of spontaneous orbital magnetism [48, 49, 50, 51].

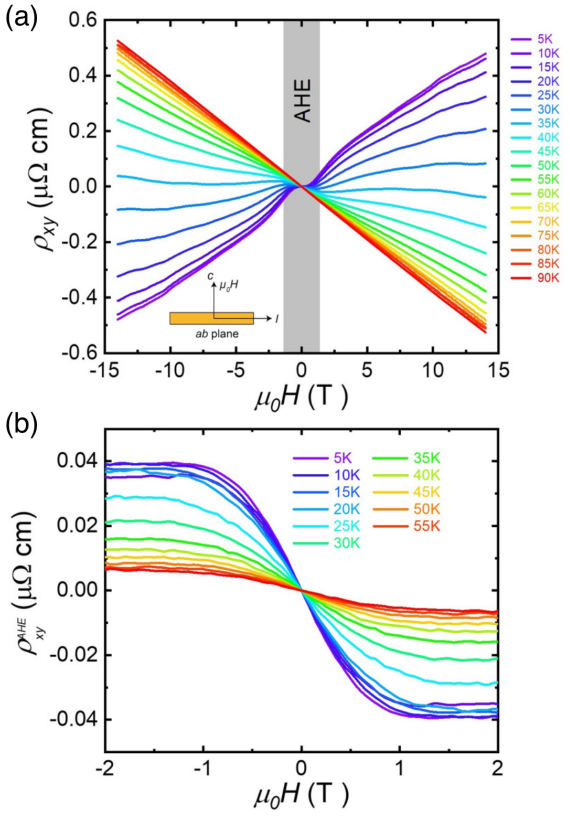

Figure 5.3: Fake AHE in CsV_3Sb_5 [Yu *et al*, 2021]

Typical data presented as evidence for the anomalous Hall effect is shown in Fig. 5.3 [48]. Hall resistivity ρ_{xy} is fitted to a linear function in the field range between 1 and 2 T, and then this linear 'ordinary' part is subtracted; what is left is called the AHE contribution $\rho_{xy}^{\mathrm{AHE}} = \rho_{xy}$ (see Fig. 5.3b). Authors observe that below the CDW onset temperature, a non-linear-in-H part emerges and is referred to as the anomalous Hall effect, despite the absence of hysteresis and $\rho_{xy}(H=0)=0$.

We speculate that the logic behind this name is probably coming from the resemblance to strong paramagnetism, which aligns spins in a finite field but is absent in a zero field. Such strong paramagnetism is then interpreted as a precursor for AHE.

Typically, analysis of Hall resistivity data also includes subtraction of the even-in-field part, which always contaminates the signal due to imperfections in contact geometry. In materials that exhibit real AHE, hysteresis makes the anti-symmetrization process tricky. Usually magnetic field is swept up and down, and the average between the two is computed $\bar{\rho}_{xy}(H) = \frac{1}{2}\left[\rho_{xy}^{\rightarrow}(H) + \rho_{xy}^{\leftarrow}(H)\right]$. Next even part $\rho_{xy}^{\mathrm{even}}(H) = \frac{1}{2}[\bar{\rho}_{xy}(H) + \bar{\rho}_{xy}(-H)]$ is subtracted: $\rho_{xy}(H) = \rho_{xy}^{\mathrm{raw}}(H) - \rho_{xy}^{\mathrm{even}}(H)$ for each of the forward and backward traces independently. This way, anti-symmetrization does not extinguish hysteresis (see e.g. [101] for an example of real AHE data). Authors of Refs. [48, 49, 50, 51] do not provide data analysis details, which leads us to believe that there is no evidence for hysteresis in the raw data as well. Thus, we conclude the presented data does not constitute evidence for spontaneous magnetism and probably should not be called the anomalous Hall effect altogether.

5.1.4 Explanation of fake anomalous Hall effect

Recent detailed studies of CsV_3Sb_5 propose a simple explanation of deviation from linear-in-H Hall resistivity without invoking the mechanism of anomalous Hall effect. They show that apparent 'anomalies' could arise from high-mobility low-density Fermi pockets opening below T_{CDW} and

specific Fermi surface reconstructions rather than intrinsic TRSB phenomena [52, 53].

Liu *et al* [52] demonstrated that a simple Drude model with electronic and hole bands of different carrier density and mobility reproduces experimental results very well. Conductivity in the Drude model is given by the sum of conductivities in each of the bands for each of the carrier types.

$$\sigma_{xy} = \sum_i \frac{e n_i \mu_i^2 H}{1 + \mu_i^2 B^2},$$

Here n_i are carrier densities and μ_i are mobilities.

Next, suppose we assume that there are non-compensated ($n_e \neq n_h$) electronic and hole bands above T_{CDW}, and that below T_{CDW} a new electronic and a new hole pocket open with higher mobilities and smaller Fermi surfaces. In that case, we can easily obtain $\rho_{xy}(H)$ function which has a wiggle at smaller fields.

Liu *et al* systematically use electron irradiation to reduce mobility of carriers and extract transport parameters for relevant bands in CsV_3Sb_5. They show by simultaneously fitting magneto-resistance (MR) and Hall resistance (HR) data in a field up to 20 T that the Drude model is fully capable of reproducing the behavior of $\rho_{xy}(H)$ observed in experiment (see Fig. 5.4).

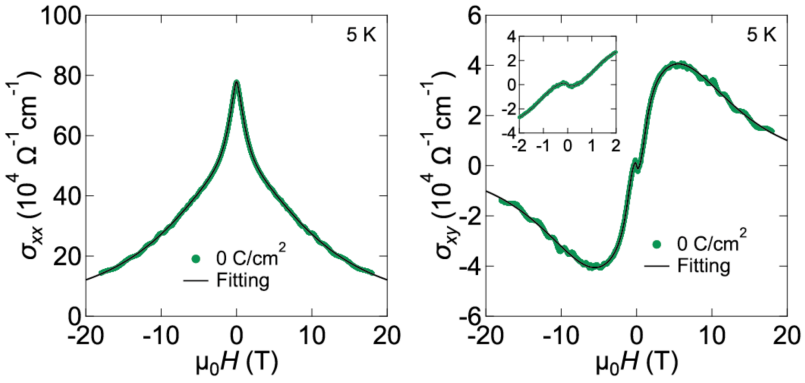

Figure 5.4: Magneto-resistance and Hall resistance in CsV_3Sb_5 [Liu *et al*, 2025]

5.2 Magneto-optical Kerr effect studies

Magneto-optical Kerr effect (MOKE) experiments have provided some of the most contentious and intriguing results regarding TRSB in CsV_3Sb_5. Initially large Kerr rotations ($\sim$ 100 μrad) concurrent with the CDW onset were reported by Xu *et al* and Wu *et al*; these findings were interpreted as strong evidence of TRSB [54, 55]. Both groups utilized a photo-elastic modulator to extract elements of the reflection matrix of the sample. This powerful method enables simultaneous

measurements of various optical properties, including circular and linear birefringence and dichroism. Versatility of the apparatus, however, is also its drawback since a signal from one type of measurement could, in principle, 'leak' into a different mode of measurement.

Contradicting these claims, we found no observable spontaneous Kerr rotation within the 30 nrad noise floor over the $d = 10$ μm beam spot size [56]. In our measurement, we used a Sagnac interferometer, which by design neglects TRS-preserving effects, hence only being sensitive to magnetic circular birefringence. Simultaneously with testing for spontaneous magnetic order, we have also measured Kerr susceptibility in small but finite fields and observed an abrupt change in the Kerr signal at T_{CDW} consistent with the opening of the CDW gap leading to a reduction of carrier density (see Fig. 5.6a).

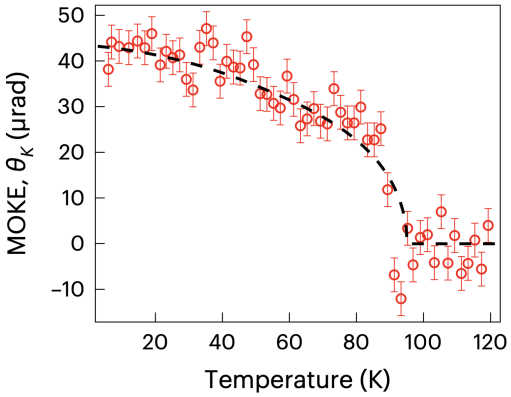

Figure 5.5: Fake MOKE in CsV_3Sb_5 [Xu *et al*, 2022]

At first, we were perplexed by our findings and tried to find an explanation for the 'accidental zeroing' of the signal in our system. One possible reason could lie in sample variability; it is possible that, depending on growth conditions, some samples might have different electronic properties. To address this issue, we've measured samples from two distinct groups: Claudia Felser's lab in MPI, Dresden, and Stephen Wilson's lab in UC Santa Barbara.

To further ensure that observed zero results cannot be explained by sample-to-sample variation, we have performed MOKE measurements on ScV_6Sn_6 samples, which are predicted to possess the same chiral flux phase as hinted by μSR [46] and transport [50] data. We observed very similar behavior, with the main difference being the sign of Kerr susceptibility: while in CsV_3Sb_5 , Kerr rotation is negative in a positive field, in ScV_6Sn_6 samples, it has the same sign as the external field. Conclusion for both CsV_3Sb_5 and ScV_6Sn_6 is very clear: there is no spontaneous magneto-optical Kerr effect.

Furthermore, our collaborator Camron Farhang from Jing Xia's group at UC Irvine has performed similar measurements on CsV_3Sb_5 using an independent Sagnac interferometer and obtained MOKE data comparable to ours. In fact, Camron measured Kerr susceptibility in a higher field and was able to cleanly subtract the contribution from optics, showing that overall in-field MOKE response is roughly proportional to magnetic susceptibility for temperatures above 50 K [56]. Below these temperatures, susceptibility demonstrates an enhancement of the paramagnetic response that is absent in MOKE data. This is due to the fact that the optical probe is only sensitive to a small volume on the sample surface and is not susceptible to bulk impurities that are responsible for the low-temperature behavior of magnetic susceptibility.

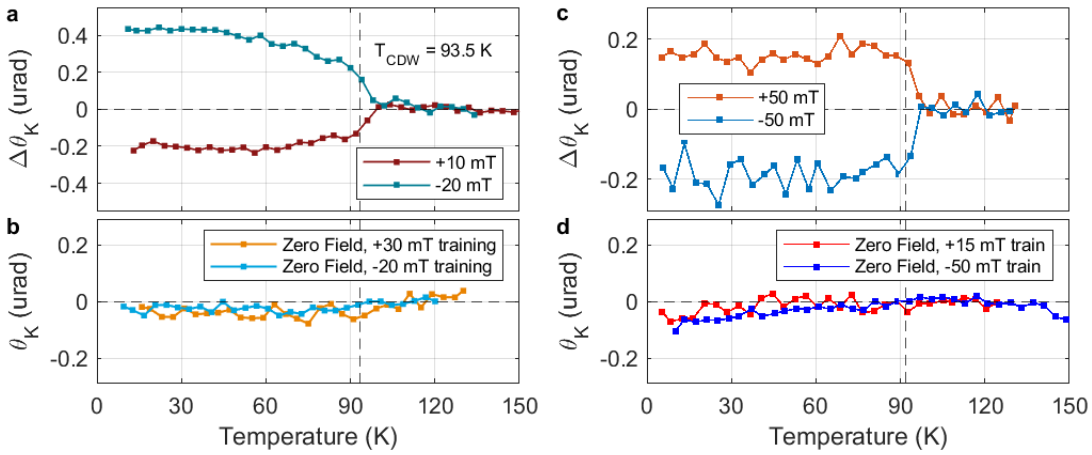

Figure 5.6: Kerr signal in CsV_3Sb_5 (a,b) and ScV_6Sn_6 (c,d) at $\lambda = 1550$ nm

5.2.1 Elasto-magneto-optical Kerr effect

While our findings showed an apparent absence of spontaneous MOKE in CsV_3Sb_5 and all existing evidence for TRSB CDW state could not stand against any reasonable scrutiny, the scientific community was not ready to so easily give up an exciting idea of chiral flux phase appearing in charge-ordered state. Many people, including ourselves, continued to seek a possible explanation for the apparent inconsistencies between different probes of TRSB.

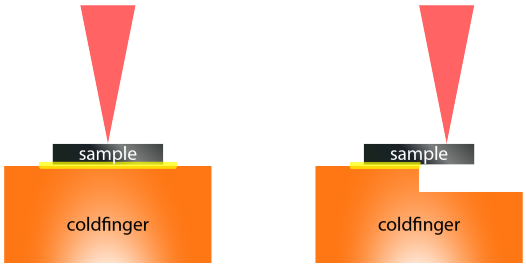

Figure 5.7: Two ways to mount a sample on a coldfinger

One idea that was put forward suggested that the TRSB state could be susceptible to strain. Namely, Guo *et al* showed that weak strain can also cause in-plane transport anisotropy [59]. Based on this measurement, Philip Moll suggested to us in a private conversation that the strain induced by the thermal mismatch between the sample and the copper coldfinger could be responsible for the null MOKE result. To address this issue, we repeated the measurement in two different geometries shown in Fig. 5.7 and found no difference.

Independently, a study by Xing *et al* demonstrated that the chirality of STM CDW peaks can be switched not only by magnetic field, but also by linearly polarized electric field [43]. They explained this effect as a result of the electrostriction effect and concluded that the TRSB parameter of CDW can be easily manipulated with strain. The authors of this study even claimed that their findings reconcile the contradicting MOKE measurements!

To systematically study the effect of stress on the MOKE signal, we used a commercially produced cryogenic uniaxial strain cell, CS100, by Razorbill. This setup allowed us to control the application

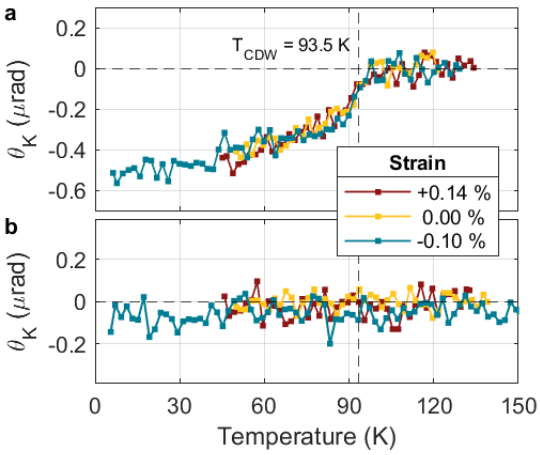

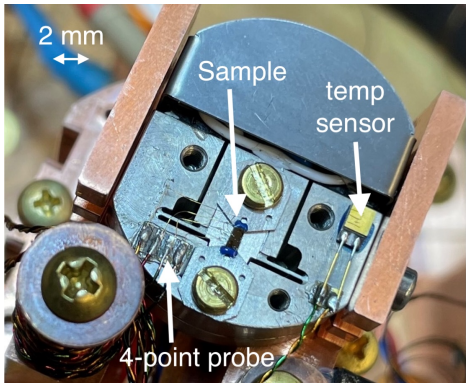

Photo of CsV_3Sb_5 on a strain cell

Figure 5.8: Kerr signal in strained CsV_3Sb_5 at $\lambda = 1550$ nm

of uniaxial stress to the sample and cool it down through the CDW transition with tensile and compressive strains applied. Of course, strictly speaking, applied strain is not purely uniaxial, but some strain in perpendicular directions is also present, which can be estimated from Poisson coefficients.

This way, we could, in principle, probe for a magnetic order parameter that couples to both the magnetic field and strain. If CsV_3Sb_5 has an order parameter ψ, which is trained by the product of magnetic field and strain, it could in principle be manipulated by either of those.

$$\mathcal{F} = -\mathbf{m} \cdot \mathbf{H} + \psi_1 \varepsilon_{x^2-y^2} H_z + \psi_2 \varepsilon_{xy} H_z + \dots$$

To test this hypothesis, we cooled down the sample through the CDW transition at finite uniaxial strain $\varepsilon = \pm 0.1\%$ in the presence of a magnetic field $H = +25$ mT, then turned the field off at temperatures much lower than T_{CDW} and measured during zero-field warmup (ZFW) at fixed applied strain.

One important technical remark is that reported strain values were estimated based on the temperature-dependent capacitance of the gap without any load. Actual strain could be different due to present stress from the sample caused by the thermal expansion coefficient mismatch between CsV_3Sb_5 and the strain cell. As a result, an unknown overall offset may be present in reported strain values, which is likely less than 0.1%.

Similar to previously reported results [56], we did not observe any spontaneous Kerr signal. In-field measurements of Kerr susceptibility in $H = +25$ mT (see Fig. 5.8a) all looked the same within our resolution for different values of applied strain.

Based on these observations, we would speculate that uniform ($\mathbf{k} = 0$) magnetic response in

CsV_3Sb_5 in small fields is not sensitive to strain. The same can be said about spontaneous magnetic order, which remains elusive. This does not, however, apply to measurement in high fields, at which CsV_3Sb_5 seems to demonstrate unexpected properties [43, 58].

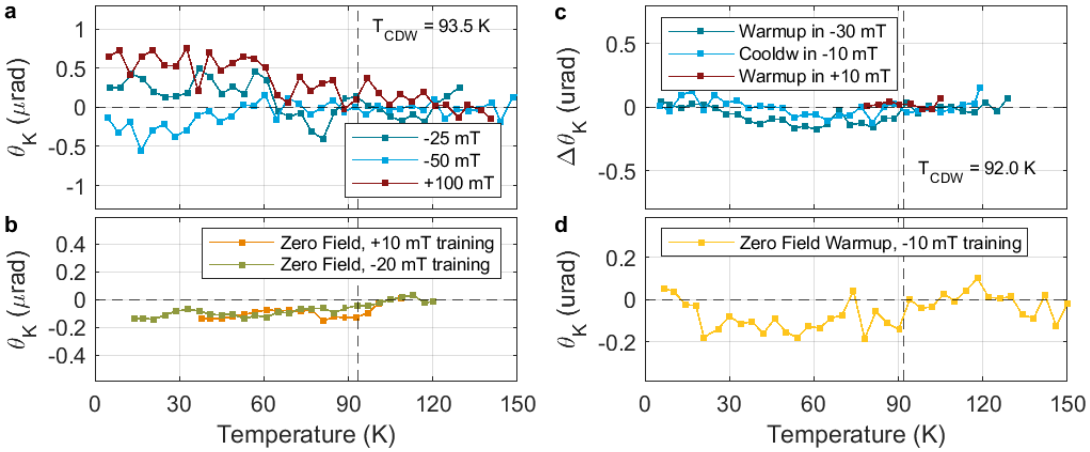

Figure 5.9: Kerr signal in CsV_3Sb_5 (a,b) and ScV_6Sn_6 (c,d) at $\lambda = 830$ nm

.

5.2.2 Wavelength dependence

Another important consideration that should be taken into account when comparing MOKE measurements producing positive results [54, 55] and null results [56] is the dependence of Kerr rotation on the frequency of the light. The measurement setup utilized a photo-elastic modulator with an 800 nm wavelength, whereas Sagnac interferometry was conducted using a 1550 nm SLED source.

Spectroscopy studies of optical conductivity [102, 103] have identified Lorentz transitions at 0.2, 0.7, and 1.2 eV, and showed that the transition at 0.7 eV includes electrons at the Fermi level (see Fig. 5.10). This observation suggests that 1550 nm should be more sensitive to electrons involved in the formation of the charge density wave. Furthermore, lower energy light is expected to be more sensitive to optical inter-band transitions since the contribution to the permittivity tensor from each transition scales with frequency as

$$\varepsilon \stackrel{+}{=} \frac{\omega_{p,k}^2}{\omega^2 - \omega_0^2 + i\omega/\tau}.$$

Nonetheless, it is possible to have an accidental zero in Kerr rotation or Kerr ellipticity at a specific frequency (e.g., see Fig. 4.15). To test whether the null result reported at 1550 nm [56] is in fact a coincidence, we have built a Sagnac interferometer at 830 nm following the steps outlined in Ref. [3].

The design of ZALSI includes many wavelength-specific components, such as polarization-maintaining fiber, waveplates, and, most importantly, the EOM, which is why it is not easy to perform ZALSI spectroscopy. Instead, all the optical parts, starting from the SLED and ending with the photodetector, have to be replaced in order to operate ZALSI at a different frequency.

Result of Kerr effect measurement on CsV_3Sb_5 and ScV_6Sn_6 performed with 830 nm ZALSI are shown in Fig. 5.9. While the noise floor in this instrument is larger than in 1550 nm ZALSI, we can still report with certainty that there is no spontaneous Kerr rotation above 100 nrad, which is 1000 times smaller than observed by Xu *et al* [54].

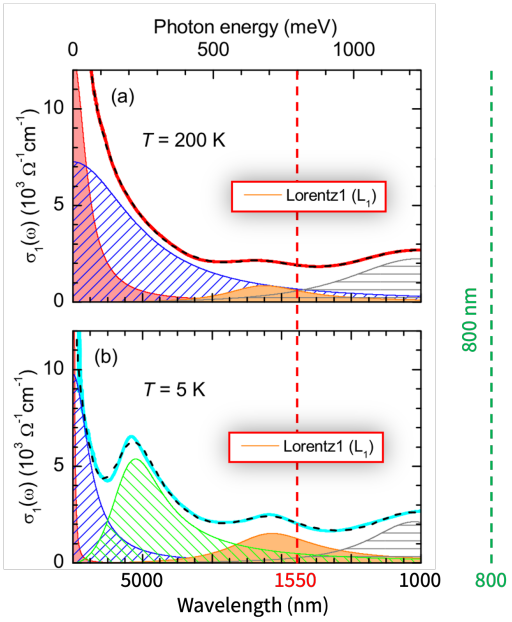

Figure 5.10: Optical conductivity of CsV_3Sb_5 [Zhou *et al*, 2021]

Furthermore, in-field measurements of the Kerr effect reveal no change in susceptibility at the CDW transition in fields of up to 100 mT within our resolution. This observation reinforces our initial hypothesis that a wavelength of 1550 nm is more sensitive to charge-ordered electrons.

5.3 Discussions

5.3.1 Is optical Kerr rotation magnetic?

After the report by Saykin *et al* [56] came out, it became clear that there is some problem with measurements of Kerr rotation by Xu *et al* [54]. To avoid controversy, the authors decided to concentrate on measurements of circular dichroism (CD) instead of circular birefringence (CB). Kerr ellipticity can be used as a probe for time-reversal symmetry breaking just as well as Kerr rotation, since it follows from straightforward analysis that TRS requires equality between reflection amplitude of two circular polarizations $r_+ = r_-$ [94].

Collaborators of Xu *et al* reported novel circular dichroism measurements at 633 nm at APS March Meeting 2024 [104]. These data have not been confronted by Saykin *et al* since the two magneto-optical effects (birefringence and dichroism) are in general different, even though they are related to each other by the Kramers-Kronig relations. Interpretation of the data was the same as before: time-reversal symmetry is spontaneously broken. Yet, the data is not convincing for two reasons.

First of all, no zero-field data was presented; only circular dichroism in high-field $H = \pm 6$ T

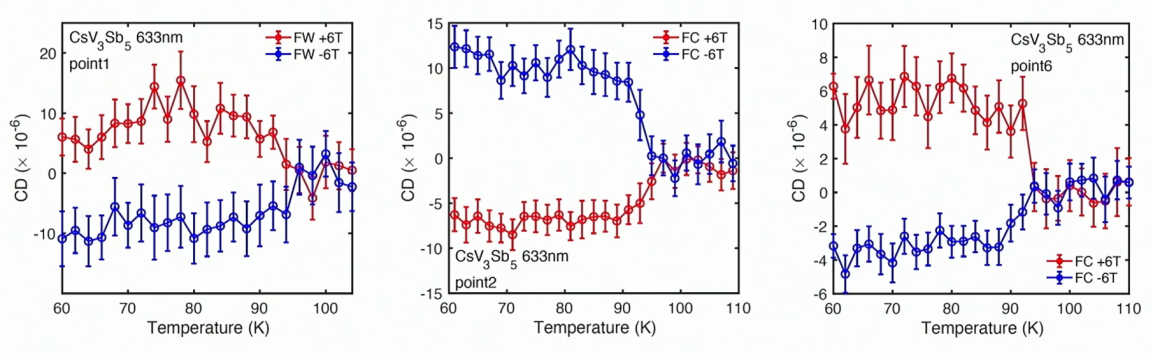

Figure 5.11: Circular dichroism in CsV_3Sb_5 [Deng *et al*, APS MM, 2024]

was demonstrated. This is important since a change in the in-field magneto-optical signal at T_{CDW} could be simply a consequence of the change in carrier density (see Fig. 5.6). Secondly, there is no fixed relation between the sign of the CD and the sign of the external field. As seen from Fig. 5.11, the sign of the effect flips from point to point. This could suggest that there is coupling to some other order parameter besides the magnetic field, as speculated in [43]; however, this scenario seems unlikely, as discussed in Subsection 5.2.1. Otherwise, the observed independence from the field sign demonstrates that CD measured by Deng *et al* is actually not magnetic in nature. Similarly to the reversal of STM peaks, a high magnetic field somehow interacts with the crystal lattice, which changes the sign of the effect, but the order detected by CD is still time-reversal symmetry preserving.

5.3.2 Isotropic rotation of linear polarization

Another stab at the mystery of optical rotation in CsV_3Sb_5 was taken by Farhang *et al* [57], who used yet another setup to detect total rotation of linearly polarized light upon reflection and extracted the isotropic component of rotation θ_C (independent of initial polarization α). As it was demonstrated in subsection 2.4.5 time-reversal symmetry prohibits any isotropic rotation, so it can be used for detection of magnetism.

$$\theta_C = \int_0^{2\pi} \theta_T(\alpha) \frac{d\alpha}{2\pi}$$

In this measurement, reflected light is split into two perpendicular components with a Wollaston prism, and the intensity of each component is measured with its own detector. Reflected

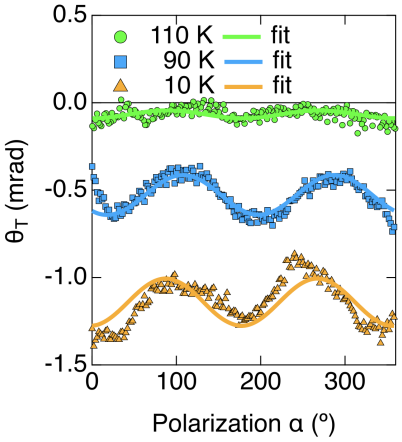

Figure 5.12: Linear polarization rotation θ_T [Farhang *et al*, 2023]

light is generally elliptically polarized with orientation of major axis at angle θ_T to x-axis, and ellipticity ε. Measured intensities are

$$I_1 = |\cos\theta_T + \sin\theta_T + i\tan\varepsilon\,(\sin\theta_T - \cos\theta_T)|^2$$
$$I_2 = |\cos\theta_T - \sin\theta_T - i\tan\varepsilon\,(\sin\theta_T + \cos\theta_T)|^2$$

From here $I_1 - I_2 \propto \sin 2\theta_T(1-\tan^2\varepsilon)$ and $I_1 + I_2 \propto 1 + \tan^2\varepsilon$, hence the Kerr angle can be extracted as

$$\tilde{\theta}_T = \frac{1}{2}\arcsin\frac{I_1 - I_2}{I_1 + I_2} = \frac{1}{2}\arcsin\left[\sin 2\theta_T \cos 2\varepsilon\right] \approx \theta_T.$$

This study found an even larger isotropic Kerr rotation of about 1 mrad. Importantly, they showed that observed rotation does not change with magnetic field and varies from sample to sample, both in sign and magnitude. Furthermore, they conducted measurements with a Wollaston prism and a Sagnac interferometer at the same wavelength of 1550 nm, showing that there is no accidental zeroing of 'fake' MOKE at 1550 nm.

The increased value of the non-magnetic optical Kerr effect (non-MOKE) can be attributed to the lower frequency of the light. Still, it could also be explained by the lower sensitivity of the apparatus and its higher susceptibility to errors. For example, if there is a mismatch in the sensitivity of the two detectors δ, then the measured quantity is modified to

$$\tilde{\theta}_T = \frac{1}{2}\arcsin\left[\frac{\sin 2\theta_T - \delta\sin^2\left(\theta_T - \frac{\pi}{4}\right)}{1 + \delta\sin^2\left(\theta_T - \frac{\pi}{4}\right)}\right].$$

Overall, there is a trend between three different types of MOKE measurements reported on CsV_3Sb_5. The Wollaston prism setup, having the worst precision, reports the highest observed Kerr rotation. At the same time, the photo-elastic modulator-based measurement reports ten times smaller signal while also having better precision. Finally, the Sagnac interferometer designed to probe only TRS breaking circular birefringence reports no signal while also having the smallest absolute measurement error. Results are summarized in Table 5.1. Correlation between reported effect and apparatus suggests that the observed non-trivial signals might be entirely a fluke.

Method	λ, nm	Precision	Typical θ_K	Error $\Delta\theta_K$
Wollaston prism [57]	1550	Low	1000 μrad	50 μrad
Photo-elastic modulator [54, 55]	800	Medium	100 μrad	5 μrad
Sagnac interferometer [56, 57]	1550, 830	High	< 0.05 μrad	0.05 μrad

Table 5.1: Comparison of different MOKE measurements in CsV_3Sb_5 .

Finally, there is one more reason to believe that observed Kerr rotation in CsV_3Sb_5 is just an experimental error. A similar story has already occurred in cuprate superconductors. Lyons *et al*

[105] observed circular dichroism in reflection in $YBa_2Cu_3O_7$ and $Bi_2Sr_2CaCu_2O_8$ below 200 K. Yet, later Lawrence *et al* [106] modified the apparatus to make it sensitive only to T-violating circular dichroism and found no evidence of magnetic circular dichroism.

Chapter 6

Conclusions

6.1 Spin-glass in infinite-layer nickelates

The main results of the present work are magneto-optical measurements of superconducting infinite-layer nickelates $La_{0.8}Sr_{0.2}NiO_2$ and $Nd_{0.825}Sr_{0.175}NiO_2$, which clearly demonstrate the presence of a spin-glass phase coexisting with superconductivity and persisting up to temperatures T_g much higher than the superconducting critical temperature T_c (see Fig. 6.1).

We presented a comprehensive study of the magnetic state of doped infinite-layer nickelates through highly sensitive measurements of the polar magneto-optical Kerr (MOKE) and Faraday (MOFE) effects using zero-area-loop Sagnac interferometers (ZALSI). Our work provides direct evidence of a spin-glass state in infinite-layer nickelate superconductors through observations of:

1. Irreversible magnetic susceptibility
2. Slow dynamics and aging
3. Memory effect

The dramatic change in magnetic signal and onset temperature between $Nd_{0.825}Sr_{0.175}NiO_2$ samples grown on $SrTiO_3$ and $(LaAlO_3)_{0.3}(Sr_2TaAlO_6)_{0.7}$ substrates indicates the importance of the sample's crystallinity on the magnitude of disorder in the exchange interaction energy. On the other hand, the relatively minor effect this change has on the superconducting T_c suggests that there is no simple, direct connection between SG order and the mechanism of superconductivity in this material - and possibly, by analogy - in the cuprates as well. Yet, in all the samples we've measured, the observed spin-glass transition temperature T_g was higher or comparable to the superconducting critical temperature T_c, hinting that a strong exchange interaction coupling might be necessary for superconductivity in infinite-layer nickelates.

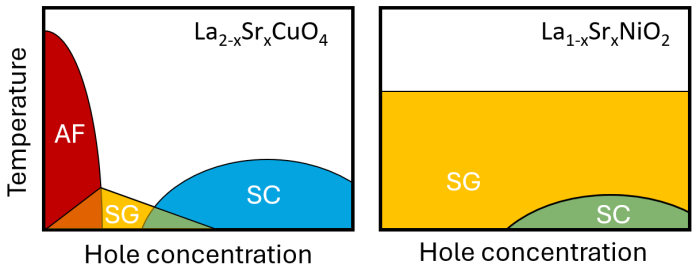

Figure 6.1: Comparison of phase diagrams of cuprates and nickelates

6.2 Charge density wave in CsV_3Sb_5

In this study, we conducted a comprehensive investigation of the kagome metal CsV_3Sb_5, focusing on its charge-density-wave (CDW) order, potential time-reversal symmetry breaking (TRSB) chiral flux phase, and the underlying mechanisms driving these phenomena.

We have described the primary experimental studies providing evidence for and against the TRSB charge-ordered state in CsV_3Sb_5 and closely related compound ScV_6Sn_6. We've presented convincing arguments as to why the available STM, μSR, and Hall transport data do not constitute smoking-gun evidence for spontaneous time-reversal symmetry breaking in CsV_3Sb_5. We have paid special attention to existing optical Kerr rotation and Kerr ellipticity data, describing the difference between various probes used to detect magneto-optical signatures of TRSB. We can state with a high degree of confidence that all observed finite Kerr rotations and circular dichroism in CsV_3Sb_5 are not magnetic in nature.

We have completed a thorough study of MOKE in CsV_3Sb_5 and ScV_6Sn_6 using ZALSI. We have conducted studies on samples grown in different laboratories, measuring the Kerr effect at two wavelengths: 1550 nm and 830 nm, and repeated the experiment under tensile and compressive uniaxial strains of 0.1% magnitude. All our studies yielded the same result: no spontaneous uniform Kerr signal above 50 nanoradians is observed. This upper bound is four orders of magnitude smaller compared to Kerr rotations measured with alternative techniques.

Our findings do not disregard the possibility of TRSB CDW in CsV_3Sb_5 completely, since the signal from finite-momentum magnetic order would be averaged out over the 10 μm beam spot size. Yet our results significantly constrain the potential magnitude of the orbital flux phase and challenge theoretical models that predict observable TRSB effects.

Appendix A

Models of optical conductivity

Let us present a toy model that provides an explicit expression for conductivity. This will help us gain some intuition into the physical meaning of the components of the permittivity tensor ε before we delve into analyzing its general properties.

A.1 Drude model

The Drude model gives the classical description of itinerant electrons in metals. In this model, electrons are imagined as a gas of charged balls, which are accelerated by an external electric field, but also slowed down by the ionic lattice. Motion of such an electron in the presence of a magnetic field is described by

$$\dot{\mathbf{v}} = \frac{q}{m}\left(\mathbf{E}(t) + \left[\frac{\mathbf{v}}{c} \times \mathbf{B}\right]\right) - \frac{\mathbf{v}}{\tau}$$

where τ is the mean free time, i.e., the typical time between scattering events. For Fourier components corresponding to plane waves $\mathbf{E}(t) = \mathbf{E}e^{-i\omega t}$, the solution is

$$\mathbf{v}_\omega = \frac{q\tau_\omega/m}{1 + (\Omega\tau_\omega)^2}\left\{\mathbf{E} + (\mathbf{E}\cdot\boldsymbol{\Omega}\tau_\omega)\boldsymbol{\Omega}\tau_\omega + [\mathbf{E}\times\boldsymbol{\Omega}\tau_\omega]\right\}, \tag{A.1}$$

$$\boldsymbol{\Omega} = \frac{q}{mc}\mathbf{H}, \qquad \tau_\omega = \left(\frac{1}{\tau} - i\omega\right)^{-1}$$

Here Ω is the cyclotron frequency, and we assume the charge of electrons to be negative $q = -|e|$. Finally, considering the case of crossed fields $\mathbf{E} \perp \mathbf{H} = H\mathbf{e}_z$, we find for the conductivity defined by

$\mathbf{j} = qn\mathbf{v} = \sigma\mathbf{E}$

$$\sigma = \frac{\sigma_0}{1+(\Omega\tau_\omega)^2}\begin{pmatrix} 1 & -\Omega\tau_\omega & 0 \\ \Omega\tau_\omega & 1 & 0 \\ 0 & 0 & 1+(\Omega\tau_\omega)^2 \end{pmatrix} \quad \sigma_0 = \frac{ne^2\tau}{m}\frac{1}{1-i\omega\tau} \tag{A.2}$$

The typical value of the mean–free time τ in good metals is $2\cdot 10^{-14}$ seconds, which corresponds to $\omega_\tau = \frac{2\pi}{\tau} \simeq 300$ THz, the frequency of 1 μm light. Hence, we should expect within the Drude model that

$$\sigma_0^{\mathrm{IR}} \approx \sigma_0^{\mathrm{DC}} = \frac{ne^2\tau}{m} \qquad\qquad \sigma_0^{\mathrm{vis,UV}} \approx \frac{ine^2}{m\omega}.$$

In bad metals or dielectrics, Drude conductivity at optical frequencies would be mostly real $\sigma_0 \approx \sigma_0^{\mathrm{DC}}$. At the same time, for any reasonable magnetic field $\Omega\tau_\omega \ll 1$, so we can simplify our result to

$$\sigma \approx \sigma_0\left[1 - i\Omega\tau_\omega \cdot \varsigma_2\right].$$

Here ς_i are 2×2 Pauli matrices (we ignore z components).

A.1.1 Boltzmann transport equation

The same result could be obtained within the semiclassical Boltzmann transport equation formalism. It operates with electron quasi-particles, which are considered as wave packets with given position and momentum. They are described by the distribution function $f = f(\mathbf{r}, \mathbf{k})$, which is conserved in the absence of scattering events.

$$\frac{\partial}{\partial t} f_{\mathbf{k}} + \left(e\mathbf{E} + \frac{q}{c}[\mathbf{v}_{\mathbf{k}} \times \mathbf{H}], \frac{\partial f_{\mathbf{k}}}{\hbar \partial \mathbf{k}} \right) + \frac{f_{\mathbf{k}} - f_{\mathbf{k}}^{(0)}}{\tau(\varepsilon_{\mathbf{k}})} = 0.$$

Here $f_{\mathbf{k}}^{(0)}$ is the equilibrium Fermi-Dirac distribution function, and the scattering integral is written in linear τ–approximation. We can perform perturbation theory in power of $\mathbf{E}$ and find that linear response has the form $f_{\mathbf{k}}^{(1)} = (\boldsymbol{\chi}, \mathbf{v}_{\mathbf{k}}) \frac{\partial f_{\mathbf{k}}^{(0)}}{\partial \varepsilon_{\mathbf{k}}}$ with constant vector $\boldsymbol{\chi}$. Substitution into the first equation leads us to

$$\frac{1}{\tau_\omega}\boldsymbol{\chi} + \frac{q}{c}[\mathbf{H} \times \hat{m}^{-1}\boldsymbol{\chi}] = -q\mathbf{E}$$

which has the same solution as the Fourier equation on velocity in the Drude model. Finally, when we compute conductivity according to

$$\mathbf{j} = q \int (d\mathbf{k}) \mathbf{v}_{\mathbf{k}} \left(\boldsymbol{\chi}, \mathbf{v}_{\mathbf{k}}\right) \frac{\partial f_{\mathbf{k}}^{(0)}}{\partial \varepsilon_{\mathbf{k}}} = \frac{e^2 \nu_F \frac{v_F^2}{3} \tau_\omega}{1 + (\Omega \tau_\omega)^2} \left(\mathbf{E} + [\mathbf{E} \times \boldsymbol{\Omega} \tau_\omega]\right).$$

We arrive at the same result as (A.2) above; however, it now has a different meaning. It is now generalized to an arbitrary Fermi liquid and not limited to a parabolic spectrum. This is clearly seen from the formula for conductivity in the DC limit

$$\sigma_{\mathrm{DC}} = e^2 \nu_F \frac{v_F^2}{3} \tau.$$

Even though we used the τ approximation to linearize the scattering integral, the mean-free time is no longer a simple phenomenological parameter; it can be used to describe several scattering mechanisms simultaneously with the help of the Matthiessen rule. Scattering here comes from impurities, phonons, or electron–electron interactions.

A.2 Drude-Lorentz model

Drude conductivity (A.2) only considers itinerant electrons close to the Fermi energy; however, at optical frequencies, conductivity is dominated by inter-band transitions at specific frequencies. The classical model describing them is the Lorentz model, which imagines that the electric field drives a gas of harmonic oscillators with frequency ω_k and damping factors $\gamma_k = \tau_k^{-1}$.

$$\dot{\mathbf{v}} + \omega_k^2 \mathbf{r} = \frac{q}{m} \left(\mathbf{E}(t) + \left[\frac{\mathbf{v}}{c} \times \mathbf{B}\right]\right) - \frac{\mathbf{v}}{\tau_k}$$

After producing the Fourier transform $\mathbf{r}_\omega = i\omega^{-1}\mathbf{v}_\omega$, we get the same solution as for the Drude model (A.1), but with a different effective frequency–dependent mean-free path $\tau_{k\omega}$. In crossed fields $\mathbf{H} = H\mathbf{e}_z$, ignoring $\Omega\tau_{k\omega} \ll 1$

$$\mathbf{j}_\omega = \frac{n e^2 \tau_k(\omega)}{m} \left\{\mathbf{E} + [\mathbf{E} \times \boldsymbol{\Omega} \tau_\omega]\right\}, \qquad \tau_k(\omega) = \frac{i\omega}{\omega^2 - \omega_0^2 + i\omega/\tau}$$

Finally, conductivity and dielectric permittivity corresponding to the optical transition at ω_k are

$$\varepsilon_k = 1 + \frac{4\pi i}{\omega}\sigma = 1 - \frac{\omega_p^2}{\omega^2 - \omega_0^2 + i\omega/\tau_k} \left[1 - i\Omega\tau_k(\omega) \cdot \varsigma_2\right],$$

where $\omega_p^2 = 4\pi n e^2/m$ is plasma frequency, for free electrons $\omega_p^2 \simeq 2\pi \times 10^3$ THz.

Finally, in any materials, both are present: polarization of itinerant electrons and bound electrons, so total polarization is a sum of the Drude contribution and all the Lorentz contributions.

$$\varepsilon = \varepsilon_\infty - \sum_{\omega_k} \frac{\omega_{p,k}^2}{\omega^2 - \omega_0^2 + i\omega/\tau_k} \left[1 - i\Omega_k \tau_k(\omega) \cdot \varsigma_2\right]$$

Here, the Drude term is included in the sum as the $\omega_0 = 0$ term, and we have also assumed that effective electron masses are different for each oscillator; hence, plasma and cyclotron frequencies are all independent.

For simplicity, let us consider the clean limit $\tau \to \infty$, then

$$\varepsilon = \varepsilon_\infty - \sum_{\omega_k} \frac{\omega_{p,k}^2}{\omega^2 - \omega_0^2} \left[1 + \frac{\omega\Omega_k}{\omega^2 - \omega_0^2} \cdot \varsigma_2\right]$$

For Drude and Lorentz transitions for which $\omega_0 \ll \omega$, we are left with

$$\varepsilon \approx \varepsilon_\infty - \frac{\omega_p^2}{\omega^2} \left[1 + \frac{\Omega}{\omega} \cdot \varsigma_2\right], \qquad \Omega = \frac{|e|H}{mc}.$$

A.3 Kubo formula

A microscopic framework for computing the optical conductivity of a material is provided by the Kubo formula from linear response theory.

$$\mathbf{j}^{(1)}(t) = \frac{ie}{\hbar} \sum_s \int \frac{d\mathbf{p}}{(2\pi\hbar)^2} f(\varepsilon_{s,\mathbf{p}}) \left\langle s, \mathbf{p} \left| \int_0^t [\hat{V}_I(\tau), \hat{\mathbf{v}}_I(t)] d\tau \right| s, \mathbf{p} \right\rangle$$

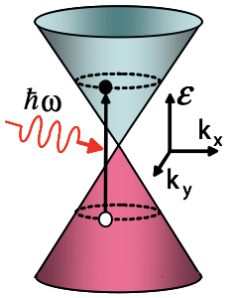

Figure A.1: Interband optical transition in graphene

Staring at this humongous formula for long does not really help in understanding the physics behind it. It's even harder to explain how to apply this formula to real-life materials, since they all possess a highly complex system of energy bands and Brillouin zone geometry.

Instead, for educational purposes, let us perform a calculation of optical conductivity using the toy model of a 2-band system: disorder-free graphene at $T = 0$ in the tight-binding approximation. Following the calculation step-by-step allows one to understand the physical meaning behind each term in the Kubo formula and gives general intuition about the quantum nature of optical conductivity.

A.3.1 Optical conductivity of graphene

Electrons in graphene are described by an effective Hamiltonian

$$\hat{H}_0 = v(\hat{\sigma}_x\hat{p}_x + \hat{\sigma}_y\hat{p}_y) = v\begin{pmatrix} 0 & \hat{p}_x - i\hat{p}_y \\ \hat{p}_x + i\hat{p}_y & 0 \end{pmatrix} \tag{A.3}$$

Here $v \sim 10^6$ m/s is Fermi velocity, Pauli matrices $\hat{\sigma}_i$ represent sub–lattice degree of freedom, and $\hat{\mathbf{p}}$ is momentum operator (see Fig. A.1).

Wavefunctions of (A.3) are plane waves with correct eigenvector (we sometimes omit $\hbar$ and use momentum and wavenumber interchangeably)

$$\psi_{s,\mathbf{q}}(\mathbf{x}) \equiv \langle \mathbf{x} \,|s,\mathbf{q}\rangle = e^{i\mathbf{q}\mathbf{x}}\mathbf{u}_{s,\mathbf{q}} \qquad \mathbf{u}_{s,\mathbf{k}} = \frac{1}{\sqrt{2}}\begin{pmatrix} \exp -\frac{i}{2}\varphi_{\mathbf{k}} \\ s\exp\frac{i}{2}\varphi_{\mathbf{k}} \end{pmatrix} \quad \tan\varphi_{\mathbf{k}} = \frac{k_y}{k_x}$$

Let's check that the eigenfunctions are normalized correctly. First, we compute

$$\mathbf{u}^\dagger_{s',\mathbf{k}'}\mathbf{u}_{s,\mathbf{k}} = \frac{1}{2}\left[e^{\frac{i}{2}(\varphi_{\mathbf{k}'}-\varphi_{\mathbf{k}})} + s's e^{\frac{i}{2}(\varphi_{\mathbf{k}}-\varphi_{\mathbf{k}'})}\right] = \begin{cases} \cos\frac{\varphi_{\mathbf{k}'}-\varphi_{\mathbf{k}}}{2}, & s' = s, \\ i\sin\frac{\varphi_{\mathbf{k}'}-\varphi_{\mathbf{k}}}{2}, & s' \neq s. \end{cases}$$

Hence $\mathbf{u}^\dagger_{s',\mathbf{k}}\mathbf{u}_{s,\mathbf{k}} = \delta_{s's}$. Next for eigenfunctions $\psi_{\mathbf{k}}$ we have $\langle s',\mathbf{k}' \,|s,\mathbf{k}\rangle = \mathbf{u}^\dagger_{s',\mathbf{k}'}\mathbf{u}_{s,\mathbf{k}}\langle \mathbf{k}' \,|\mathbf{k}\rangle$. We adopt a convention

$$\langle \mathbf{k}' \,|\mathbf{k}\rangle = \int d\mathbf{x}\, e^{i(\mathbf{k}-\mathbf{k}')\mathbf{x}} = (2\pi)^2\delta(\mathbf{k}'-\mathbf{k}).$$

Velocity operator Let's calculate matrix elements of velocity operator $\hat{\mathbf{v}} = v\hat{\boldsymbol{\sigma}}$. First, we note that the operator $\hat{\mathbf{v}}$ is diagonal in position–momentum space. For completeness, we compute three components of vector $\mathbf{v}$ even though z–component is of no use in this problem.

$$\mathbf{u}^\dagger_{s',\mathbf{k}}\sigma_x\mathbf{u}_{s,\mathbf{k}} = \frac{1}{2}\begin{pmatrix} e^{-\frac{i}{2}\varphi_{\mathbf{k}}} \\ s'e^{\frac{i}{2}\varphi_{\mathbf{k}}} \end{pmatrix}^\dagger \begin{pmatrix} se^{\frac{i}{2}\varphi_{\mathbf{k}}} \\ e^{-\frac{i}{2}\varphi_{\mathbf{k}}} \end{pmatrix} = \frac{1}{2}(se^{i\varphi_{\mathbf{k}}} + s'e^{-i\varphi_{\mathbf{k}}})$$

$$\mathbf{u}^\dagger_{s',\mathbf{k}}\sigma_y\mathbf{u}_{s,\mathbf{k}} = \frac{i}{2}\begin{pmatrix} e^{-\frac{i}{2}\varphi_{\mathbf{k}}} \\ s'e^{\frac{i}{2}\varphi_{\mathbf{k}}} \end{pmatrix}^\dagger \begin{pmatrix} -se^{\frac{i}{2}\varphi_{\mathbf{k}}} \\ e^{-\frac{i}{2}\varphi_{\mathbf{k}}} \end{pmatrix} = \frac{1}{2i}(se^{i\varphi_{\mathbf{k}}} - s'e^{-i\varphi_{\mathbf{k}}})$$

$$\mathbf{u}^\dagger_{s',\mathbf{k}}\sigma_z\mathbf{u}_{s,\mathbf{k}} = \frac{1}{2}\begin{pmatrix} e^{-\frac{i}{2}\varphi_{\mathbf{k}}} \\ s'e^{\frac{i}{2}\varphi_{\mathbf{k}}} \end{pmatrix}^\dagger \begin{pmatrix} e^{-\frac{i}{2}\varphi_{\mathbf{k}}} \\ -se^{\frac{i}{2}\varphi_{\mathbf{k}}} \end{pmatrix} = \frac{1}{2}(1 - s's) \equiv \langle s' \,|\, s_x \,|s\rangle \equiv \delta_{s'\bar{s}}$$

Combining all into one formula, we get the same expression as [107, (5)].

$$\langle s', \mathbf{k}| \mathbf{v} |s, \mathbf{k}\rangle = \frac{v}{2}\begin{pmatrix} se^{i\varphi_{\mathbf{k}}} + s'e^{-i\varphi_{\mathbf{k}}} \\ -ise^{i\varphi_{\mathbf{k}}} + is'e^{-i\varphi_{\mathbf{k}}} \\ 1 - s's \end{pmatrix}$$

$$\hat{\mathbf{v}} = \int d\mathbf{k} \frac{|\mathbf{k}\rangle\langle\mathbf{k}|}{(2\pi)^2 S}\frac{v}{|\mathbf{k}|}\begin{pmatrix} \mathbf{k} & |\mathbf{k}|\mathbf{e}_z + i[\mathbf{e}_z \times \mathbf{k}] \\ |\mathbf{k}|\mathbf{e}_z - i[\mathbf{e}_z \times \mathbf{k}] & -\mathbf{k} \end{pmatrix}$$

Same expression in a short form (from now on, we ignore z–component of velocity operator)

$$\langle \mathbf{k}'| \hat{\mathbf{v}} |\mathbf{k}\rangle = v\left(\frac{\mathbf{k}}{|\mathbf{k}|}\hat{s}_z + \frac{[\mathbf{e}_z \times \mathbf{k}]}{|\mathbf{k}|}\hat{s}_y + \mathbf{e}_z\hat{s}_x\right) \cdot \langle \mathbf{k}' |\mathbf{k}\rangle$$

Position operator Let's also calculate the matrix elements of the position operator. We can employ identity $\hat{\mathbf{v}} = \frac{i}{\hbar}[\hat{H}_0, \hat{\mathbf{r}}]$ and find (here $\hbar\omega_{\mathbf{k}} = v|\mathbf{k}|$, so that $\varepsilon_{s,\hbar\mathbf{k}} = s\hbar\omega_{\mathbf{k}}$)

$$\begin{aligned}\langle s', \mathbf{k}'| \hat{\mathbf{r}} |s, \mathbf{k}\rangle &= -i\frac{\langle s', \mathbf{k}'| \hat{\mathbf{v}} |s, \mathbf{k}\rangle}{s'\omega_{\mathbf{k}'} - s\omega_{\mathbf{k}}} \\ &= \frac{v}{|\mathbf{k}|}\left[-i\mathbf{k}\frac{\delta_{s's}}{\omega_{\mathbf{k}'} - \omega_{\mathbf{k}}} + [\mathbf{e}_z \times \mathbf{k}]\frac{\delta_{s'\bar{s}}}{2\omega_{\mathbf{k}}}\right]\langle \mathbf{k}' |\mathbf{k}\rangle \end{aligned} \tag{A.4}$$

The first term is irregular; let's see if we can find an alternative expression for the matrix elements of $\hat{\mathbf{r}}$.

$$\langle s', \mathbf{k}'| \hat{\mathbf{r}} |s, \mathbf{k}\rangle = \mathbf{u}^{\dagger}_{s'\mathbf{k}'}\mathbf{u}_{s\mathbf{k}}\int d\mathbf{r}\, e^{i(\mathbf{k}-\mathbf{k}')\mathbf{r}}\mathbf{r} = (2\pi)^2 i\mathbf{u}^{\dagger}_{s'\mathbf{k}'}\mathbf{u}_{s\mathbf{k}}\nabla_{\mathbf{k}'}\delta(\mathbf{k}' - \mathbf{k})$$

This expression should be treated as functional. We first compute

$$\delta(\mathbf{k}' - \mathbf{k})\nabla_{\mathbf{k}'}\mathbf{u}^{\dagger}_{s'\mathbf{k}'}\mathbf{u}_{s\mathbf{k}} = \delta(\mathbf{k}' - \mathbf{k})\delta_{s'\bar{s}}\frac{i}{2}\nabla_{\mathbf{k}'}\varphi_{\mathbf{k}'}$$

$$\partial_\mu\varphi_{\mathbf{k}} = \frac{1}{1 + (k_y/k_x)^2}\left[\frac{k_x\delta_{\mu,2}}{k_x^2} - \frac{k_y\delta_{\mu,1}}{k_x^2}\right] = \frac{[\mathbf{e}_z \times \mathbf{k}]_\mu}{k^2}.$$

Now we simplify the expression for the derivative of δ–function using integration by parts.

$$\begin{aligned}\langle s', \mathbf{k}'| \hat{\mathbf{r}} |s, \mathbf{k}\rangle &= i\mathbf{u}^{\dagger}_{s'\mathbf{k}'}\mathbf{u}_{s\mathbf{k}}\nabla_{\mathbf{k}'}\langle \mathbf{k}' |\mathbf{k}\rangle \\ &= \frac{[\mathbf{e}_z \times \mathbf{k}]}{2k^2}\delta_{s'\bar{s}}\langle \mathbf{k}' |\mathbf{k}\rangle - i\delta_{s's}\langle \mathbf{k}' |\mathbf{k}\rangle \nabla_{\mathbf{k}'}(\dots) \end{aligned} \tag{A.5}$$

We see that expressions (A.4) and (A.5) agree if we differentiate a function that doesn't depend on momentum direction $f = f(|\mathbf{k}|)$.

Kubo formula We consider an electric field at frequency ω as perturbation which is turned on at $t = 0$.

$$\hat{V}(t) = \theta(t)|e|(\mathbf{E}\cdot\hat{\mathbf{r}})\cos\omega t = \hat{W}\theta(t)\cos\omega t, \quad \hat{W} = |e|(\mathbf{E}\cdot\hat{\mathbf{r}})$$

The wavefunction can be found perturbatively as (in the interaction picture)

$$|s,\mathbf{k}\rangle_t^I = \left[\hat{\mathbb{1}} - \frac{i}{\hbar}\int \hat{V}_I(\tau)d\tau + \dots\right]|s,\mathbf{k}\rangle_{t=0}^{(0)}$$

Next, we want to calculate the expectation value of the current operator

$$\mathbf{j} = e\sum_{s,\mathbf{k}} f(s\hbar\omega_{\mathbf{k}})\,\langle s,\mathbf{k}|_t^I\,\hat{\mathbf{v}}_I(t)\,|s,\mathbf{k}\rangle_t^I$$

The zeroth-order term should be zero since there is no current in the absence of a field; indeed, the integral over the directions of $\mathbf{k}$ gives zero. First–order is provided by the Kubo formula.

$$\begin{aligned}
\mathbf{j}^{(1)} &= \frac{ie}{\hbar}\sum_s\int\frac{d\mathbf{k}}{(2\pi)^2}f_{s,\mathbf{k}}\,\langle s,\mathbf{k}|\int_0^t[\hat{V}_I(\tau),\hat{\mathbf{v}}_I(t)]d\tau\,|s,\mathbf{k}\rangle \\
&= \frac{ie}{\hbar}\sum_{s,\sigma}\int\frac{d\mathbf{k}d\mathbf{q}}{(2\pi)^4 S}f_{s,\mathbf{k}}\int^t\Big[\langle s,\mathbf{k}|\hat{W}|\sigma,\mathbf{q}\rangle\langle\sigma,\mathbf{q}|\hat{\mathbf{v}}|s,\mathbf{k}\rangle e^{i(\omega_{s,\mathbf{k}}-\omega_{\sigma,\mathbf{q}})(\tau-t)} - \\
&\qquad - \langle s,\mathbf{k}|\hat{\mathbf{v}}|\sigma,\mathbf{q}\rangle\langle\sigma,\mathbf{q}|\hat{W}|s,\mathbf{k}\rangle e^{i(\omega_{\sigma,\mathbf{q}}-\omega_{s,\mathbf{k}})(\tau-t)}\Big]\cos\omega\tau\,d\tau \\
&= \frac{e}{2\hbar}\sum_{s,\sigma,\pm}\int\frac{d\mathbf{k}d\mathbf{q}}{(2\pi)^4 S}f_{s,\mathbf{k}}\left[\frac{\langle s,\mathbf{k}|\hat{W}|\sigma,\mathbf{q}\rangle\langle\sigma,\mathbf{q}|\hat{\mathbf{v}}|s,\mathbf{k}\rangle}{\omega_{s,\mathbf{k}}-\omega_{\sigma,\mathbf{q}}\pm\omega} - \frac{\langle s,\mathbf{k}|\hat{\mathbf{v}}|\sigma,\mathbf{q}\rangle\langle\sigma,\mathbf{q}|\hat{W}|s,\mathbf{k}\rangle}{\omega_{\sigma,\mathbf{q}}-\omega_{s,\mathbf{k}}\pm\omega}\right]e^{\pm i\omega t} \\
&= \frac{e}{2\hbar}\sum_{s,\sigma,\pm}\int\frac{d\mathbf{k}}{(2\pi)^2}f_{s,\mathbf{k}}\left[\frac{\langle s|\hat{W}_{\mathbf{k}}|\sigma\rangle\langle\sigma|\hat{\mathbf{v}}_{\mathbf{k}}|s\rangle}{\omega_{s,\mathbf{k}}-\omega_{\sigma,\mathbf{k}}\pm\omega} - \frac{\langle s|\hat{\mathbf{v}}_{\mathbf{k}}|\sigma\rangle\langle\sigma|\hat{W}_{\mathbf{k}}|s\rangle}{\omega_{\sigma,\mathbf{k}}-\omega_{s,\mathbf{k}}\pm\omega}\right]e^{\pm i\omega t}
\end{aligned}$$

After integration over $\mathbf{q}$ we are left with an extra δ–function at 0 argument, which gives sample area $(2\pi)^2\delta(\mathbf{k}=0) = S$ in the current normalization convention. We will now split this expression into two contributions $\mathbf{j} = \mathbf{j}_{\mathrm{s}} + \mathbf{j}_{\mathrm{a}}$, which correspond to $\sigma = s$ and $\sigma = \bar{s} \equiv -s$ respectively. Let's consider the symmetric part. We see that it's zero at charge neutrality.

$$\mathbf{j}_{\mathrm{s}} = \frac{e}{\hbar}E_\alpha\int_{-\infty}^{\infty}\frac{kdk}{4\pi\omega}\frac{\partial f_{\mathbf{k}}}{\partial k}\sin\omega t = 0.$$

Next,

$$\begin{aligned}
\mathbf{j}_{\mathrm{a}} &= \frac{e}{2\hbar}\sum_s \int \frac{d\mathbf{k}}{(2\pi)^2} f_{s,\mathbf{k}} \sum_{\pm} \left[\frac{\langle s|\,\hat{W}_{\mathbf{k}}\,|\bar{s}\rangle\,\langle \bar{s}|\,\hat{\mathbf{v}}_{\mathbf{k}}\,|s\rangle}{2s\omega_{\mathbf{k}} \pm \omega} - \frac{\langle s|\,\hat{\mathbf{v}}_{\mathbf{k}}\,|\bar{s}\rangle\,\langle \bar{s}|\,\hat{W}_{\mathbf{k}}\,|s\rangle}{-2s\omega_{\mathbf{q}} \pm \omega} \right] e^{\pm i\omega t} \\
&= \frac{e^2}{2\hbar} E_\alpha \sum_s \int \frac{d\mathbf{k}}{(2\pi)^2} f_{s,\mathbf{k}} \frac{iv^2}{s\omega_{\mathbf{k}}} \frac{\mathbf{k}_\perp k_\perp^\alpha}{k^2} \frac{-4s\omega_{\mathbf{k}}}{4\omega_{\mathbf{k}}^2 - \omega^2} \cos\omega t \\
&= -2i\frac{v^2e^2}{\hbar} E_\alpha \sum_s \int \frac{d\mathbf{k}}{(2\pi)^2} f_{s,\mathbf{k}} \frac{\mathbf{k}_\perp k_\perp^\alpha}{k^2} \frac{\cos\omega t}{4\omega_{\mathbf{k}}^2 - \omega^2} \\
&= -i\frac{v^2e^2}{2\pi\hbar}\mathbf{E} \int_{-\infty}^{\infty} kdk \frac{f(\hbar v k)}{4\omega_{\mathbf{k}}^2 - \omega^2} \cos\omega t \\
&= \frac{e^2}{\hbar}\frac{\mathbf{E}}{2\pi i} \int_0^{\infty} \frac{\varepsilon d\varepsilon}{4\varepsilon^2 - \omega^2} \cos\omega t
\end{aligned}$$

This integral should be regularized such that it obeys causality $\omega = \omega + i0$, then half–residual at $\varepsilon = \frac{\omega}{2}$ is what we are left with.

$$\mathbf{j}_{\mathrm{a}} = \frac{e^2}{4\hbar}\mathbf{E}\cos\omega t$$

We've obtained a beautiful result known as *universal optical conductivity*.

$$\sigma(\omega) = \frac{e^2}{4\hbar}. \tag{A.6}$$

Remarkably, this result holds for real graphene as long as $\omega \gg \tau^{-1}, T$ [108].

Transmittance We can use the result (A.6) to calculate optical transmittance of 2D graphene [109]. Full system of equations

$$\begin{aligned}
\nabla\cdot\mathbf{E} &= 4\pi\rho & \nabla\cdot\mathbf{B} &= 0 \\
\nabla\times\mathbf{B} &= \frac{4\pi}{c}\mathbf{j} + \frac{1}{c}\frac{\partial}{\partial t}\mathbf{E} & \nabla\times\mathbf{E} &= -\frac{1}{c}\frac{\partial}{\partial t}\mathbf{B} \\
\partial_t\rho + \nabla\cdot\mathbf{j} &= 0 & \mathbf{j} &= \sigma_0\delta(z)\mathbf{E}, \quad \sigma_0 = \frac{e^2}{4\hbar}.
\end{aligned}$$

Here $\mathbf{j}$ is the linear current density and ρ is the surface charge density. Propagation of electromagnetic waves is described by

$$-\frac{1}{c^2}\frac{\partial^2}{\partial t^2}\mathbf{E} + \nabla^2\mathbf{E} - \nabla(\nabla\cdot\mathbf{E}) = \frac{4\pi}{c^2}\frac{\partial}{\partial t}\mathbf{j}.$$

Let's choose x axis along the direction of electric field $\mathbf{E} = (E_x(z), 0, 0)e^{-i\omega t}$. For normal incidence $\nabla\cdot\mathbf{E} = 0$, hence $\rho = 0$ and $\nabla\cdot\mathbf{j} = 0$. Electric field above the membrane is the sum of incident and

reflected waves $E_x(z>0) = E^{(i)}e^{-ikz} + E^{(r)}e^{ikz}$, while below the flake of graphene we have only transmitted wave $E_x(z<0) = E^{(t)}e^{-ikz}$. Magnitude of wavevector is the same for all three waves because they satisfy the same wave equation and have identical frequency $\omega = ck$.

$$\frac{\omega^2}{c^2}E_x + \frac{d^2}{dz^2}E_x = -i\omega\frac{4\pi}{c^2}\delta(z)\sigma_0 E_x(0).$$

First of all, we see that the field is continuous since $\delta(z)$ is proportional to the second derivative.

$$E^{(i)} + E^{(r)} = E^{(t)} = E_x(0).$$

Next, integrating over z

$$\left.\frac{dE_x}{dz}\right|_{-0}^{+0} = -ikE^{(i)} + ikE^{(r)} + ikE^{(t)} = -ik\frac{4\pi}{c}\sigma_0 E_x(0).$$

Solving for transmission amplitude

$$t = \frac{E^{(t)}}{E^{(i)}} = \left(1 + 2\pi\frac{\sigma_0}{c}\right)^{-1} = \left(1 + \frac{\pi}{2}\alpha\right)^{-1}.$$

Finally, transmittance is $T = |t|^2 \approx 1 - \pi\alpha$ with $\alpha = e^2/\hbar c \simeq \frac{1}{137}$ standing for fine–structure constant.

Appendix B

Polarimetry

B.1 Mueller calculus

Suppose light of unknown polarization is coming from the source, and we would like to measure how much of the light is unpolarized, how much is linearly polarized, and how much is circularly polarized. Mueller calculus can answer these questions. Stokes parameters are used to describe polarization of the light. They are defined in such a way that they can be extracted from intensity measurements. Unlike amplitude coefficients, Stokes parameters are purely real and do not contain information about light phase.

Stokes vector of elliptically polarized light with major axis at angle ψ to horizontal and ellipticity χ is given by

$$\mathbf{S} = \begin{pmatrix} I \\ Q \\ U \\ V \end{pmatrix} = \begin{pmatrix} I_{\text{total}} \\ I_{\text{pol}} \cos 2\chi \cos 2\psi \\ I_{\text{pol}} \cos 2\chi \sin 2\psi \\ I_{\text{pol}} \sin 2\chi \end{pmatrix}$$

For linearly polarized light $\varepsilon = 0$. If additional unpolarized light is present, it will increase the value of I, but the values of Q, U, V will be untouched since they have the meaning of intensity differences between different polarization components, while the unpolarized part is always assumed to be uniform without loss of generality.

Fully polarized Jones vector can be converted to Stokes vector according to

$$\mathbf{E} = \begin{pmatrix} E_x \\ E_y \end{pmatrix} = \begin{pmatrix} E_{0x} e^{i\phi_x} \\ E_{0y} e^{i\phi_y} \end{pmatrix} \quad \mapsto \quad \mathbf{S} = \begin{pmatrix} E_{0x}^2 + E_{0y}^2 \\ E_{0x}^2 - E_{0y}^2 \\ 2E_{0x}E_{0y}\cos(\phi_x - \phi_y) \\ 2E_{0x}E_{0y}\sin(\phi_x - \phi_y) \end{pmatrix} \tag{B.1}$$

Sometimes opposite conventions for the sign of $S_3 = V$ are used.

B.2 Measuring Stokes parameters

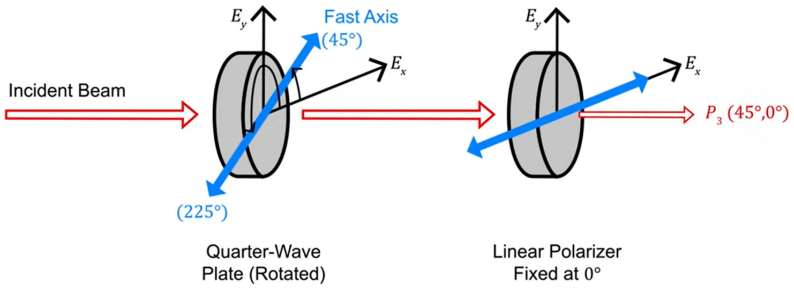

Figure B.1: Rotating quarter–waveplate method

Stokes parameters can be measured using a so-called rotating quarter-wave plate (QWP) method. Let's say light passes through QWP with slow axis oriented at angle η to horizontal plane and then passes through linear polarizer oriented at angle ξ, which is usually assumed to be zero (without loss of generality) and η is measured as the angle between QWP and polarizer.

Light traveling along slow axis (x) of QWP acquires additional phase $\Delta\varphi = \frac{\omega}{c}\Delta n \cdot \Delta z = \frac{\pi}{2}$, where Δz is the thickness of QWP and $\Delta n = n_e - n_o$ is its birefringence. The Jones matrix of QWP is given by

$$Q = e^{i\frac{\pi}{4}\sigma_z} = \begin{pmatrix} e^{i\frac{\pi}{4}} & 0 \\ 0 & e^{-i\frac{\pi}{4}} \end{pmatrix} \qquad R_\eta = e^{-i\eta\sigma_y} = \begin{pmatrix} \cos\eta & -\sin\eta \\ \sin\eta & \cos\eta \end{pmatrix}$$

We could use adjoint action formula $R_{-\eta}\sigma_z R_\eta = \sigma_z \cos 2\eta - \sigma_x \sin 2\eta$ to produce rotation

$$\begin{aligned} Q_\eta = R_\eta Q R_{-\eta} &= \cos\frac{\pi}{4} + iR_\eta\sigma_z R_{-\eta}\sin\frac{\pi}{4} \\ &= \frac{1}{\sqrt{2}} + \frac{i}{\sqrt{2}}(\sigma_z\cos 2\eta + \sigma_x \sin 2\eta) \\ &= \frac{1}{\sqrt{2}}\begin{pmatrix} 1 + i\cos 2\eta & i\sin 2\eta \\ i\sin 2\eta & 1 - i\cos 2\eta \end{pmatrix} \end{aligned}$$

Next, we can find Mueller matrix for a quarter–wave plate with slow axis at angle η according to (compare to general retarder matrix with fast axis at angle θ)

$$\mathbb{Q}_\eta = A(Q_\eta \otimes Q_\eta^*)A^{-1} = \begin{pmatrix} 1 & 0 & 0 & 0 \\ 0 & \cos^2 2\eta & \frac{1}{2}\sin 4\eta & -\sin 2\eta \\ 0 & \frac{1}{2}\sin 4\eta & \sin^2 2\eta & \cos 2\eta \\ 0 & \sin 2\eta & -\cos 2\eta & 0 \end{pmatrix} \qquad A = \begin{pmatrix} 1 & 0 & 0 & 1 \\ 1 & 0 & 0 & -1 \\ 0 & 1 & 1 & 0 \\ 0 & i & -i & 0 \end{pmatrix}$$

Similarly, for polarizer P at an angle ξ Jones matrix is

$$P_\xi = R_\xi P R_{-\xi} = \frac{1}{2} + \frac{1}{2} R_\xi \sigma_z R_{-\xi} = \frac{1}{2} + \frac{1}{2}\left(\sigma_z \cos 2\xi + \sigma_x \sin 2\xi\right)$$

which in Mueller representation looks like (compare to general polarizer matrix at angle θ)

$$\mathbb{P}_\xi = A(P_\xi \otimes P_\xi^*)A^{-1} = \frac{1}{2}\begin{pmatrix} 1 & \cos 2\xi & \sin 2\xi & 0 \\ \cos 2\xi & \cos^2 2\xi & \frac{1}{2}\sin 4\xi & 0 \\ \sin 2\xi & \frac{1}{2}\sin 4\xi & \sin^2 2\xi & 0 \\ 0 & 0 & 0 & 0 \end{pmatrix}$$

Passing through both the QWP and the polarizer is described by the product

$$T_{\xi\eta} = P_\xi Q_\eta = \frac{1}{\sqrt{2}} P_\xi + \frac{1}{2} Q_\eta - \frac{1}{\sqrt{2}} + \frac{i}{2\sqrt{2}}\left[\cos 2(\eta - \xi) + i\sigma_y \sin 2(\eta - \xi)\right]$$
$$2\sqrt{2} T_{\xi\eta} = 1 + i\cos 2(\eta - \xi) + \sigma_x\left[i\sin 2\eta + \sin 2\xi\right] - \sigma_y\left[\sin 2(\eta - \xi)\right] + \sigma_z\left[i\cos 2\eta + \cos 2\xi\right]$$

Since the formula becomes cumbersome, let us consider two limiting cases: $\xi = 0$ and $\xi = \frac{\pi}{2}$. Total intensity of transmitted light, which initially had Stokes coefficients (I, Q, U, V) is

$$\xi = 0: \qquad 2I_{\text{final}} = \left(I + \frac{Q}{2}\right) - V\sin 2\eta + \frac{Q}{2}\cos 4\eta + \frac{U}{2}\sin 4\eta,$$
$$\xi = \frac{\pi}{2}: \qquad 2I_{\text{final}} = \left(I - \frac{Q}{2}\right) + V\sin 2\eta - \frac{Q}{2}\cos 4\eta - \frac{U}{2}\sin 4\eta.$$

Here η is orientation of slow axis of QWP, if we're measuring fast axis instead, simple replacement $\eta \mapsto \eta \pm \frac{\pi}{2}$ will result in change of $\operatorname{sgn} V$.

$$\xi = 0: \qquad 2I_{\text{final}} = \left(I + \frac{Q}{2}\right) + V\sin 2\eta + \frac{Q}{2}\cos 4\eta + \frac{U}{2}\sin 4\eta,$$
$$\xi = \frac{\pi}{2}: \qquad 2I_{\text{final}} = \left(I - \frac{Q}{2}\right) - V\sin 2\eta - \frac{Q}{2}\cos 4\eta - \frac{U}{2}\sin 4\eta. \tag{B.2}$$

B.3 Examples

Let's focus on the case of a vertically oriented polarizer and η being the angle of the fast axis of QWP, i.e., use equation (B.2).

B.3.1 Linearly polarized light

Suppose incident light is fully polarized with polarization angle θ. Then according to (B.1)

$$\mathbf{E} = \begin{pmatrix} \cos\theta \\ \sin\theta \end{pmatrix} \qquad \mathbf{S} = \begin{pmatrix} 1 \\ \cos 2\theta \\ \sin 2\theta \\ 0 \end{pmatrix} \qquad 2I(\eta) = \left(1 - \frac{\cos 2\theta}{2}\right) - \frac{\cos 2\theta}{2}\cos 4\eta - \frac{\sin 2\theta}{2}\sin 4\eta.$$

B.3.2 Sum of two decoherent components

Consider light traveling along polarization–maintaining fiber. It enters the fiber linearly polarized at 45 degrees, and the signal is split equally between fast and slow modes of the fiber patch, which have refractive indices of $n_y = 1.4492$ and $n_x = 1.4496$, respectively. Further assume that SLED emitted this light with vacuum-wavelength $\lambda_0 = 1550$ nm and FWHM spectral width $\Delta\lambda_0 = 50$ nm, so that it has frequency $f = \omega/2\pi = c/\lambda_0 \simeq 200$ THz. In a medium such as fiber with refractive index $n = 1.4494$, the wavelength is effectively shorter $\lambda_n = \lambda/n$, while the frequency is the same as in vacuum. Now, since such a light wave packet consists of waves with different frequencies (i.e., different energies) which do not interfere with each other, it has a finite coherence time τ_φ. This time can be estimated from the following argument: if after time τ_φ wave components from the edge of the spectrum $\omega \pm \frac{\Delta\omega}{2}$ are single period apart, then the sum over all frequencies in between will average out to zero. From here $\Delta\omega\tau_\varphi \sim 2\pi$ or $\Delta f\tau_\varphi \sim 1$. Similarly, one can define the coherence length of $l_\varphi = v\tau_\varphi$. Since $\Delta f/f \approx \Delta\lambda_0/\lambda_0 = \Delta\lambda_n/\lambda_n$ we can express coherence length as

$$l_\varphi = \frac{\lambda_0^2}{n\Delta\lambda_0} = 33\ \mu\text{m},$$

Or, in other words, it has a coherence time given by

$$\tau_\varphi = \frac{\lambda_0^2}{c\Delta\lambda_0} = 160\ \text{fs}.$$

Alternatively, we could also define phase difference, which leads to decoherence.

$$\phi_\varphi = 2\pi \cdot \frac{f}{\Delta f} = 2\pi \cdot \frac{\lambda_0}{\Delta\lambda_0} \simeq 31 \cdot 2\pi.$$

In our case birefringence is $\delta n = 4.2 \cdot 10^{-4}$, so they will acquire phase difference $\delta\phi = \phi_x - \phi_y \sim \phi_\varphi$ after traveling for

$$L = \frac{k}{\delta k} l_\varphi = \frac{n}{\delta n} l_\varphi = 3451 \cdot l_\varphi = \frac{\lambda_0^2}{\delta n \cdot \Delta\lambda_0} = 114 \text{ mm}.$$

Suppose incident light consists of two perpendicular decoherent components (which will happen after traveling along a polarization-maintaining fiber for more than 10 cm as described above). Their Stokes vector is the sum of two vectors.

$$\mathbf{S} = \frac{1}{2}\begin{pmatrix}1\\1\\0\\0\end{pmatrix} + \frac{1}{2}\begin{pmatrix}1\\-1\\0\\0\end{pmatrix} = \begin{pmatrix}1\\0\\0\\0\end{pmatrix} \qquad 2I(\eta) = 1.$$

Note that this is different from coherent sum, which would result in fully linearly polarized light oriented at 45 degrees.

B.3.3 Testing sample QWP

Assume we pass light through a circulator (with a fast axis blocking, i.e., a built-in polarizer) and then send it to the sample through a fiber patch. Before reflecting off the sample, the laser beam goes through a collimator, a quarter-wave plate, and a lens. How would the intensity of reflected light (on port 3 of the circulator) depend on the orientation of the QWP?

$$Q_\eta^2 = i\begin{pmatrix}\cos 2\eta & \sin 2\eta\\ \sin 2\eta & -\cos 2\eta\end{pmatrix}$$

If we send in linearly polarized light (along the slow axis, i.e., x), the intensity at the detector is going to be

$$I(\eta) = \left|\hat{x}^T Q_\eta^2 \hat{x}\right|^2 = \cos^2 2\eta = \frac{1+\cos 4\eta}{2}$$

In reality, there is an overall damping factor due to insertion loss. Additionally, finite polarization extinction ratio (two modes mix with each other inside the fiber) and back reflections (between the fiber and collimator) lead to a non-zero value.

Now, assume that we place a polarizer at 45 degrees, so that an equal amount of light is sent along the fast and slow axes of the polarization-maintaining fiber. When they reach the quarter-wave plate, they do not interfere; hence, they should be considered independently. However, on the way back, two components that travel in opposite directions will interfere. The easiest way to see that only off-diagonal terms should be summed as amplitudes is to introduce a fiber matrix $F_\phi = \text{diag}(1, e^\phi)$, which describes fiber birefringence, and then look at which terms have the same

phase.

$$\begin{aligned} I(\eta) &= |J_{11}|^2 + |J_{12} + J_{21}|^2 + |J_{22}|^2, \qquad J = \frac{1}{\sqrt{2}} Q_\eta^2 \frac{1}{\sqrt{2}}, \\ &= \left| \frac{\cos 2\eta}{2} \right|^2 + \left| \frac{\sin 2\eta}{2} + \frac{\sin 2\eta}{2} \right|^2 + \left| -\frac{\cos 2\eta}{2} \right|^2 \\ &= \frac{3 - \cos 4\eta}{4}. \end{aligned}$$

If we place an intensity modulator on one of the arms, it will introduce a large insertion loss α_0^2 along the slow (x) axis. Note that α_0 describes reduction in amplitude, while α_0^2 describes reduction in intensity.

$$\begin{aligned} I(\eta) &= |\alpha_0^2 J_{11}|^2 + |\alpha_0 J_{12} + \alpha_0 J_{21}|^2 + |J_{22}|^2, \qquad J = \frac{1}{\sqrt{2}} Q_\eta^2 \frac{1}{\sqrt{2}}, \\ &= \alpha_0^4 \left| \frac{\cos 2\eta}{2} \right|^2 + \alpha_0^2 \left| \frac{\sin 2\eta}{2} + \frac{\sin 2\eta}{2} \right|^2 + \left| -\frac{\cos 2\eta}{2} \right|^2 \\ &= \frac{(1 + 4\alpha_0^2 + \alpha_0^4) + (1 + \alpha_0^4 - 4\alpha_0^2) \cos 4\eta}{8}. \end{aligned}$$

Bibliography

[1] Jing Xia. *Optical studies of broken time-reversal symmetry in solids using Sagnac interferometry*. PhD thesis, Stanford University, September 2008.

[2] Hovnatan Karapetyan. *Magneto-optical studies of high-temperature superconductors using Sagnac interferometry*. PhD thesis, Stanford University, June 2013.

[3] Alexander D. Fried. *Measurements of Nonreciprocity in Materials With a Sagnac Interferometer*. PhD thesis, Stanford University, July 2014.

[4] R. Elizabeth Schemm. *Optical Characterization of Time Reversal Symmetry Breaking States in Heavy Fermion Superconductors*. PhD thesis, Stanford University, August 2014.

[5] Camron Farhang. *Investigation of Time-Reversal Symmetry Breaking in Emerging Topological Phases with Sagnac Interferometry*. PhD thesis, UC Irvine, 2024.

[6] Evgenii Mikhailovich Lifshitz and Lev Petrovich Pitaevskii. *Statistical physics: Theory of the condensed state*, volume 9. Elsevier, 2013.

[7] D. N. Basov, Richard D. Averitt, Dirk van der Marel, Martin Dressel, and Kristjan Haule. Electrodynamics of correlated electron materials. *Rev. Mod. Phys.*, 83:471–541, Jun 2011.

[8] Patrick A. Lee, Naoto Nagaosa, and Xiao-Gang Wen. Doping a mott insulator: Physics of high-temperature superconductivity. *Rev. Mod. Phys.*, 78:17–85, Jan 2006.

[9] Eduardo Fradkin, Steven A. Kivelson, and John M. Tranquada. Colloquium: Theory of intertwined orders in high temperature superconductors. *Rev. Mod. Phys.*, 87:457–482, May 2015.

[10] Jonathan A. Sobota, Yu He, and Zhi-Xun Shen. Angle-resolved photoemission studies of quantum materials. *Rev. Mod. Phys.*, 93:025006, May 2021.

[11] Yuan Cao, Valla Fatemi, Shiang Fang, Kenji Watanabe, Takashi Taniguchi, Efthimios Kaxiras, and Pablo Jarillo-Herrero. Unconventional superconductivity in magic-angle graphene superlattices. *Nature*, 556(7699):43–50, 2018.

[12] Allan H MacDonald. Bilayer graphene's wicked, twisted road. *Physics*, 12:12, 2019.

[13] B.D. White, J.D. Thompson, and M.B. Maple. Unconventional superconductivity in heavy-fermion compounds. *Physica C: Superconductivity and its Applications*, 514:246–278, 2015. Superconducting Materials: Conventional, Unconventional and Undetermined.

[14] J. W. Chen, S. E. Lambert, M. B. Maple, Z. Fisk, J. L. Smith, G. R. Stewart, and J. O. Willis. Upper critical magnetic field of the heavy-fermion superconductor upt_3. *Phys. Rev. B*, 30:1583–1585, Aug 1984.

[15] P. E. Sulewski, A. J. Sievers, M. B. Maple, M. S. Torikachvili, J. L. Smith, and Z. Fisk. Far-infrared absorptivity of upt_3. *Phys. Rev. B*, 38:5338–5352, Sep 1988.

[16] L. Taillefer, R. Newbury, G.G. Lonzarich, Z. Fisk, and J.L. Smith. Direct observation of heavy quasiparticles in upt3 via the dhva effect. *Journal of Magnetism and Magnetic Materials*, 63-64:372–376, 1987.

[17] L. Taillefer and G. G. Lonzarich. Heavy-fermion quasiparticles in upt_3. *Phys. Rev. Lett.*, 60:1570–1573, Apr 1988.

[18] Sheng Ran, I-Lin Liu, Yun Suk Eo, Daniel J. Campbell, Paul M. Neves, Wesley T. Fuhrman, Shanta R. Saha, Christopher Eckberg, Hyunsoo Kim, David Graf, Fedor Balakirev, John Singleton, Johnpierre Paglione, and Nicholas P. Butch. Extreme magnetic field-boosted superconductivity. *Nature Physics*, 15(12):1250–1254, 2019.

[19] Rafael M Fernandes and Andrey V Chubukov. Low-energy microscopic models for iron-based superconductors: a review. *Reports on Progress in Physics*, 80(1):014503, nov 2016.

[20] Danfeng Li, Kyuho Lee, Bai Yang Wang, Motoki Osada, Samuel Crossley, Hye Ryoung Lee, Yi Cui, Yasuyuki Hikita, and Harold Y. Hwang. Superconductivity in an infinite-layer nickelate. *Nature*, 572(7771):624–627, Aug 2019.

[21] A. S. Botana and M. R. Norman. Similarities and differences between $lanio_2$ and $cacuo_2$ and implications for superconductivity. *Phys. Rev. X*, 10:011024, Feb 2020.

[22] Yi Cui, Cong Li, Qing Li, Xiyu Zhu, Ze Hu, Yi-feng Yang, Jinshan Zhang, Rong Yu, Hai-Hu Wen, and Weiqiang Yu. Nmr evidence of antiferromagnetic spin fluctuations in nd0. 85sr0. 15nio2. *Chinese Physics Letters*, 38(6):067401, 2021.

[23] H. Lu, M. Rossi, A. Nag, M. Osada, D. F. Li, K. Lee, B. Y. Wang, M. Garcia-Fernandez, S. Agrestini, Z. X. Shen, E. M. Been, B. Moritz, T. P. Devereaux, J. Zaanen, H. Y. Hwang, Ke-Jin Zhou, and W. S. Lee. Magnetic excitations in infinite-layer nickelates. *Science*, 373(6551):213–216, 2021.

[24] Hai Lin, Dariusz Jakub Gawryluk, Yannick Maximilian Klein, Shangxiong Huangfu, Ekaterina Pomjakushina, Fabian von Rohr, and Andreas Schilling. Universal spin-glass behaviour in bulk lanio2, prnio2 and ndnio2. *New Journal of Physics*, 24(1):013022, jan 2022.

[25] R. A. Ortiz, P. Puphal, M. Klett, F. Hotz, R. K. Kremer, H. Trepka, M. Hemmida, H.-A. Krug von Nidda, M. Isobe, R. Khasanov, H. Luetkens, P. Hansmann, B. Keimer, T. Schäfer, and M. Hepting. Magnetic correlations in infinite-layer nickelates: An experimental and theoretical multimethod study. *Phys. Rev. Res.*, 4:023093, May 2022.

[26] P. Puphal, B. Wehinger, J. Nuss, K. Küster, U. Starke, G. Garbarino, B. Keimer, M. Isobe, and M. Hepting. Synthesis and physical properties of $lanio_2$ crystals. *Phys. Rev. Mater.*, 7:014804, Jan 2023.

[27] Philipp Werner and Shintaro Hoshino. Nickelate superconductors: Multiorbital nature and spin freezing. *Phys. Rev. B*, 101:041104, Jan 2020.

[28] Qing Li, Chengping He, Jin Si, Xiyu Zhu, Yue Zhang, and Hai-Hu Wen. Absence of superconductivity in bulk nd1- x sr x nio2. *Communications Materials*, 1(1):16, 2020.

[29] Jennifer Fowlie, Marios Hadjimichael, Maria M Martins, Danfeng Li, Motoki Osada, Bai Yang Wang, Kyuho Lee, Yonghun Lee, Zaher Salman, Thomas Prokscha, et al. Intrinsic magnetism in superconducting infinite-layer nickelates. *Nature Physics*, 18(9):1043–1047, 2022.

[30] Ruby A Shi, Bai Yang Wang, Yusuke Iguchi, Motoki Osada, Kyuho Lee, Berit H Goodge, Lena F Kourkoutis, Harold Y Hwang, and Kathryn A Moler. Scanning squid study of ferromagnetism and superconductivity in infinite-layer nickelates. *Physical Review Materials*, 8(2):024802, 2024.

[31] Brenden R. Ortiz, Lídia C. Gomes, Jennifer R. Morey, Michal Winiarski, Mitchell Bordelon, John S. Mangum, Iain W. H. Oswald, Jose A. Rodriguez-Rivera, James R. Neilson, Stephen D. Wilson, Elif Ertekin, Tyrel M. McQueen, and Eric S. Toberer. New kagome prototype materials: discovery of kv_3sb_5, rbv_3sb_5, and csv_3sb_5. *Phys. Rev. Mater.*, 3:094407, Sep 2019.

[32] Hasitha W Suriya Arachchige, William R Meier, Madalynn Marshall, Takahiro Matsuoka, Rui Xue, Michael A McGuire, Raphael P Hermann, Huibo Cao, and David Mandrus. Charge density wave in kagome lattice intermetallic scv 6 sn 6. *Physical Review Letters*, 129(21):216402, 2022.

[33] Brenden R. Ortiz, Samuel M. L. Teicher, Yong Hu, Julia L. Zuo, Paul M. Sarte, Emily C. Schueller, A. M. Milinda Abeykoon, Matthew J. Krogstad, Stephan Rosenkranz, Raymond Osborn, Ram Seshadri, Leon Balents, Junfeng He, and Stephen D. Wilson. CsV_3Sb_5: A $\mathbb{Z}_2$ topological kagomé metal with a superconducting ground state. *Phys. Rev. Lett.*, 125:247002, Dec 2020.

[34] Stephen D. Wilson and Brenden R. Ortiz. Av3sb5 kagome superconductors. *Nature Reviews Materials*, 9(6):420–432, Jun 2024.

[35] Xilin Feng, Kun Jiang, Ziqiang Wang, and Jiangping Hu. Chiral flux phase in the kagomé superconductor AV_3Sb_5. *Science Bulletin*, 66(14):1384–1388, 2021.

[36] M. Michael Denner, Ronny Thomale, and Titus Neupert. Analysis of charge order in the kagome metal AV_3Sb_5 ($A = \mathrm{K}, \mathrm{Rb}, \mathrm{Cs}$). *Phys. Rev. Lett.*, 127:217601, Nov 2021.

[37] Heqiu Li, Yong Baek Kim, and Hae-Young Kee. Intertwined van hove singularities as a mechanism for loop current order in kagome metals. *Phys. Rev. Lett.*, 132:146501, Apr 2024.

[38] Zhiwei Wang, Yu-Xiao Jiang, Jia-Xin Yin, Yongkai Li, Guan-Yong Wang, Hai-Li Huang, Sen Shao, Jinjin Liu, Peng Zhu, Nana Shumiya, Md Shafayat Hossain, Hongxiong Liu, Youguo Shi, Junxi Duan, Xiang Li, Guoqing Chang, Pengcheng Dai, Zijin Ye, Gang Xu, Yanchao Wang, Hao Zheng, Jinfeng Jia, M. Zahid Hasan, and Yugui Yao. Electronic nature of chiral charge order in the kagomé superconductor CsV_3Sb_5. *Phys. Rev. B*, 104:075148, Aug 2021.

[39] Yu-Xiao Jiang, Jia-Xin Yin, M. Michael Denner, Nana Shumiya, Brenden R. Ortiz, Gang Xu, Zurab Guguchia, Junyi He, Md Shafayat Hossain, Xiaoxiong Liu, Jacob Ruff, Linus Kautzsch, Songtian S. Zhang, Guoqing Chang, Ilya Belopolski, Qi Zhang, Tyler A. Cochran, Daniel Multer, Maksim Litskevich, Zi-Jia Cheng, Xian P. Yang, Ziqiang Wang, Ronny Thomale, Titus Neupert, Stephen D. Wilson, and M. Zahid Hasan. Unconventional chiral charge order in kagomé superconductor KV_3Sb_5. *Nature Materials*, 20(10):1353–1357, Oct 2021.

[40] Nana Shumiya, Md. Shafayat Hossain, Jia-Xin Yin, Yu-Xiao Jiang, Brenden R. Ortiz, Hongxiong Liu, Youguo Shi, Qiangwei Yin, Hechang Lei, Songtian S. Zhang, Guoqing Chang, Qi Zhang, Tyler A. Cochran, Daniel Multer, Maksim Litskevich, Zi-Jia Cheng, Xian P. Yang, Zurab Guguchia, Stephen D. Wilson, and M. Zahid Hasan. Intrinsic nature of chiral charge order in the kagomé superconductor RbV_3Sb_5. *Phys. Rev. B*, 104:035131, Jul 2021.

[41] Huazhou Li, Siyuan Wan, Han Li, Qing Li, Qiangqiang Gu, Huan Yang, Yongkai Li, Zhiwei Wang, Yugui Yao, and Hai-Hu Wen. No observation of chiral flux current in the topological kagome metal csv_3sb_5. *Phys. Rev. B*, 105:045102, Jan 2022.

[42] Hong Li, He Zhao, Brenden R. Ortiz, Takamori Park, Mengxing Ye, Leon Balents, Ziqiang Wang, Stephen D. Wilson, and Ilija Zeljkovic. Rotation symmetry breaking in the normal state of a kagome superconductor kv3sb5. *Nature Physics*, 18(3):265–270, Mar 2022.

[43] Yuqing Xing, Seokjin Bae, Ethan Ritz, Fan Yang, Turan Birol, Andrea N. Capa Salinas, Brenden R. Ortiz, Stephen D. Wilson, Ziqiang Wang, Rafael M. Fernandes, and Vidya Madhavan. Optical manipulation of the charge-density-wave state in rbv3sb5. *Nature*, 631(8019):60–66, Jul 2024.

[44] Rustem Khasanov, Debarchan Das, Ritu Gupta, Charles Mielke, Matthias Elender, Qiangwei Yin, Zhijun Tu, Chunsheng Gong, Hechang Lei, Ethan T. Ritz, Rafael M. Fernandes, Turan Birol, Zurab Guguchia, and Hubertus Luetkens. Time-reversal symmetry broken by charge order in csv_3sb_5. *Phys. Rev. Research*, 4:023244, Jun 2022.

[45] Zhaoyang Shan, Pabitra K. Biswas, Sudeep K. Ghosh, T. Tula, Adrian D. Hillier, Devashibhai Adroja, Stephen Cottrell, Guang-Han Cao, Yi Liu, Xiaofeng Xu, Yu Song, Huiqiu Yuan, and Michael Smidman. Muon spin relaxation study of the layered kagome superconductor csv_3sb_5. *Phys. Rev. Res.*, 4:033145, Aug 2022.

[46] Z Guguchia, DJ Gawryluk, Soohyeon Shin, Z Hao, C Mielke III, D Das, I Plokhikh, L Liborio, J Kane Shenton, Y Hu, et al. Hidden magnetism uncovered in a charge ordered bilayer kagome material scv6sn6. *Nature communications*, 14(1):7796, 2023.

[47] Eric M Kenney, Brenden R Ortiz, Chennan Wang, Stephen D Wilson, and Michael J Graf. Absence of local moments in the kagome metal kv3sb5 as determined by muon spin spectroscopy. *Journal of Physics: Condensed Matter*, 33(23):235801, may 2021.

[48] F. H. Yu, T. Wu, Z. Y. Wang, B. Lei, W. Z. Zhuo, J. J. Ying, and X. H. Chen. Concurrence of anomalous hall effect and charge density wave in a superconducting topological kagomé metal. *Phys. Rev. B*, 104:L041103, Jul 2021.

[49] Shuo-Ying Yang, Yaojia Wang, Brenden R. Ortiz, Defa Liu, Jacob Gayles, Elena Derunova, Rafael Gonzalez-Hernandez, Libor Šmejkal, Yulin Chen, Stuart S. P. Parkin, Stephen D. Wilson, Eric S. Toberer, Tyrel McQueen, and Mazhar N. Ali. Giant, unconventional anomalous hall effect in the metallic frustrated magnet candidate, KV_3Sb_5. *Science Advances*, 6(31):eabb6003, 2020.

[50] Changjiang Yi, Xiaolong Feng, Nitesh Kumar, Claudia Felser, and Chandra Shekhar. Tuning charge density wave of kagome metal scv6sn6. *New Journal of Physics*, 26(5):052001, may 2024.

[51] Shirin Mozaffari, William R. Meier, Richa P. Madhogaria, Nikolai Peshcherenko, Seoung-Hun Kang, John W. Villanova, Hasitha W. Suriya Arachchige, Guoxin Zheng, Yuan Zhu, Kuan-Wen Chen, Kaila Jenkins, Dechen Zhang, Aaron Chan, Lu Li, Mina Yoon, Yang Zhang, and David G. Mandrus. Universal sublinear resistivity in vanadium kagome materials hosting charge density waves. *Phys. Rev. B*, 110:035135, Jul 2024.

[52] S Liu, M Roppongi, M Kimata, K Ishihara, R Grasset, M Konczykowski, BR Ortiz, SD Wilson, K Yoshimi, T Shibauchi, et al. Impact of tiny fermi pockets with extremely high mobility on the hall anomaly in the kagome metal csv _3 sb _5. *arXiv preprint arXiv:2503.15849*, 2025.

[53] A. E. Koshelev, R. Chapai, D. Y. Chung, J. F. Mitchell, and U. Welp. Origin of anomalous magnetotransport in kagome superconductors $a\mathrm{v_3sb_5}$ (a = K,rb,cs). *Phys. Rev. B*, 110:024512, Jul 2024.

[54] Yishuai Xu, Zhuoliang Ni, Yizhou Liu, Brenden R. Ortiz, Qinwen Deng, Stephen D. Wilson, Binghai Yan, Leon Balents, and Liang Wu. Three-state nematicity and magneto-optical kerr effect in the charge density waves in kagome superconductors. *Nature Physics*, 18(12):1470–1475, Dec 2022.

[55] Qiong Wu, Z. X. Wang, Q. M. Liu, R. S. Li, S. X. Xu, Q. W. Yin, C. S. Gong, Z. J. Tu, H. C. Lei, T. Dong, and N. L. Wang. Simultaneous formation of two-fold rotation symmetry with charge order in the kagome superconductor $\mathrm{csv_3sb_5}$ by optical polarization rotation measurement. *Phys. Rev. B*, 106:205109, Nov 2022.

[56] David R. Saykin, Camron Farhang, Erik D. Kountz, Dong Chen, Brenden R. Ortiz, Chandra Shekhar, Claudia Felser, Stephen D. Wilson, Ronny Thomale, Jing Xia, and Aharon Kapitulnik. High resolution polar kerr effect studies of $\mathrm{csv_3sb_5}$: Tests for time-reversal symmetry breaking below the charge-order transition. *Phys. Rev. Lett.*, 131:016901, Jul 2023.

[57] Camron Farhang, Jingyuan Wang, Brenden R. Ortiz, Stephen D. Wilson, and Jing Xia. Unconventional specular optical rotation in the charge ordered state of kagome metal csv3sb5. *Nature Communications*, 14(1):5326, Sep 2023.

[58] Chunyu Guo, Carsten Putzke, Sofia Konyzheva, Xiangwei Huang, Martin Gutierrez-Amigo, Ion Errea, Dong Chen, Maia G. Vergniory, Claudia Felser, Mark H. Fischer, Titus Neupert, and Philip J. W. Moll. Switchable chiral transport in charge-ordered kagome metal csv3sb5. *Nature*, 611(7936):461–466, Nov 2022.

[59] Chunyu Guo, Glenn Wagner, Carsten Putzke, Dong Chen, Kaize Wang, Ling Zhang, Martin Gutierrez-Amigo, Ion Errea, Maia G. Vergniory, Claudia Felser, Mark H. Fischer, Titus Neupert, and Philip J. W. Moll. Correlated order at the tipping point in the kagome metal csv3sb5. *Nature Physics*, 20(4):579–584, Apr 2024.

[60] Hao-Tian Liu, Junkang Huang, Tao Zhou, and Wen Huang. Constraints on the orbital flux phase in $a\mathrm{v_3sb_5}$ from the polar kerr effect. *Phys. Rev. B*, 111:L041109, Jan 2025.

[61] Jiaqi Cai, Eric Anderson, Chong Wang, Xiaowei Zhang, Xiaoyu Liu, William Holtzmann, Yinong Zhang, Fengren Fan, Takashi Taniguchi, Kenji Watanabe, Ying Ran, Ting Cao, Liang Fu, Di Xiao, Wang Yao, and Xiaodong Xu. Signatures of fractional quantum anomalous hall states in twisted mote2. *Nature*, 622(7981):63–68, 2023.

[62] Lev Davidovich Landau, John Stewart Bell, MJ Kearsley, LP Pitaevskii, EM Lifshitz, and JB Sykes. *Electrodynamics of continuous media*, volume 8. elsevier, 2013.

[63] FI Fyodorov. *Theory of Gyrotropy*. Minsk, 1976.

[64] P. S. Pershan. Magneto-optical effects. *Journal of Applied Physics*, 38(3):1482–1490, 1967.

[65] Pavan Hosur, A. Kapitulnik, S. A. Kivelson, J. Orenstein, and S. Raghu. Kerr effect as evidence of gyrotropic order in the cuprates. *Phys. Rev. B*, 87:115116, Mar 2013.

[66] Gregory N. Henderson, Thomas K. Gaylord, and Elias N. Glytsis. Electromagnetic analogies to general-hamiltonian effective-mass electron wave propagation in semiconductors with spatially varying effective mass and potential energy. *Phys. Rev. B*, 45:8404–8407, Apr 1992.

[67] Jeanne Riga and Rebecca Seviour. Electromagnetic analogs of quantum mechanical tunneling. *Journal of Applied Physics*, 132(20):200901, 11 2022.

[68] Aharon Kapitulnik. Notes on constraints for the observation of polar kerr effect in complex materials. *Physica B: Condensed Matter*, 460:151–158, 2015. Special Issue on Electronic Crystals (ECRYS-2014).

[69] Jing Xia, Peter T. Beyersdorf, M. M. Fejer, and Aharon Kapitulnik. Modified sagnac interferometer for high-sensitivity magneto-optic measurements at cryogenic temperatures. *Applied Physics Letters*, 89(6):062508, 2006.

[70] A. Kapitulnik, J. S. Dodge, and M. M. Fejer. High-resolution magneto-optic measurements with a sagnac interferometer (invited). *Journal of Applied Physics*, 75(10):6872–6877, 05 1994.

[71] S. Spielman, K. Fesler, C. B. Eom, T. H. Geballe, M. M. Fejer, and A. Kapitulnik. Test for nonreciprocal circular birefringence in $yba_2cu_3o_7$ thin films as evidence for broken time-reversal symmetry. *Phys. Rev. Lett.*, 65:123–126, Jul 1990.

[72] Steven Russel Spielman. *OOptical tests for broken time-reversal symmetry in cuprate superconductors*. PhD thesis, Stanford University, June 1992.

[73] Jing Xia, W. Siemons, G. Koster, M. R. Beasley, and A. Kapitulnik. Critical thickness for itinerant ferromagnetism in ultrathin films of $SrRuO_3$. *Phys. Rev. B*, 79:140407(R), Apr 2009.

[74] Jing Xia, V. Shelukhin, M. Karpovski, A. Kapitulnik, and A. Palevski. Inverse proximity effect in superconductor-ferromagnet bilayer structures. *Phys. Rev. Lett.*, 102:087004, Feb 2009.

[75] Jing Xia, Yoshiteru Maeno, Peter T. Beyersdorf, M. M. Fejer, and Aharon Kapitulnik. High resolution polar kerr effect measurements of sr_2ruo_4: Evidence for broken time-reversal symmetry in the superconducting state. *Phys. Rev. Lett.*, 97:167002, Oct 2006.

[76] E. M. Levenson-Falk, E. R. Schemm, Y. Aoki, M. B. Maple, and A. Kapitulnik. Polar kerr effect from time-reversal symmetry breaking in the heavy-fermion superconductor $pros_4sb_{12}$. *Phys. Rev. Lett.*, 120:187004, May 2018.

[77] E. R. Schemm, W. J. Gannon, C. M. Wishne, W. P. Halperin, and A. Kapitulnik. Observation of broken time-reversal symmetry in the heavy-fermion superconductor UPt_3. *Science*, 345(6193):190–193, JUL 2014.

[78] I. M. Hayes, D. S. Wei, T. Metz, J. Zhang, Y. S. Eo, S. Ran, S. R. Saha, J. Collini, N. P. Butch, D. F. Agterberg, A. Kapitulnik, and J. Paglione. Multicomponent superconducting order parameter in UTe_2. *Science*, 373(6556):797–801, 2021.

[79] Di S. Wei, David Saykin, Oliver Y. Miller, Sheng Ran, Shanta R. Saha, Daniel F. Agterberg, Jörg Schmalian, Nicholas P. Butch, Johnpierre Paglione, and Aharon Kapitulnik. Interplay between magnetism and superconductivity in ute_2. *Phys. Rev. B*, 105:024521, Jan 2022.

[80] Charles Kittel and Paul McEuen. *Introduction to solid state physics*. John Wiley & Sons, 2018.

[81] Amit Mondal, Riju Dey, Andreja Jelen, Primož Koželj, Sandip Kumar Kuila, Rahul Pan, Stanislav Vrtnik, Jože Luzar, Magdalena Wencka, Julia Petrović, Peter Mihor, Zvonko Jagličić, Anton Meden, Partha Pratim Jana, and Janez Dolinšek. Double helix of icosahedra structure and spin glass magnetism of the co2.5zn17.5–xmnx (x = 0.4–3.5) pseudo-binary alloys. *Inorganic Chemistry*, 63(22):10251–10263, 2024.

[82] P. Koželj, S. Vrtnik, M. Krnel, A. Jelen, D. Gačnik, M. Wencka, Z. Jagličić, A. Meden, G. Dražić, F. Danoix, J. Ledieu, M. Feuerbacher, and J. Dolinšek. Spin-glass magnetism of the non-equiatomic cocrfemnni high-entropy alloy. *Journal of Magnetism and Magnetic Materials*, 523:167579, 2021.

[83] E. Vincent. *Ageing, Rejuvenation and Memory: The Example of Spin-Glasses*, pages 7–60. Springer Berlin Heidelberg, Berlin, Heidelberg, 2007.

[84] Eric Vincent. Spin glass experiments. In Tapash Chakraborty, editor, *Encyclopedia of Condensed Matter Physics (Second Edition)*, pages 371–387. Academic Press, Oxford, second edition edition, 2024.

[85] Helmut G. Katzgraber, Didier Hérisson, Michael Östh, Per Nordblad, Atsuko Ito, and Hiroko Aruga Katori. Finite versus zero-temperature hysteretic behavior of spin glasses: Experiment and theory. *Phys. Rev. B*, 76:092408, Sep 2007.

[86] Eric Vincent, Jacques Hammann, Miguel Ocio, Jean-Philippe Bouchaud, and Leticia F. Cugliandolo. Slow dynamics and aging in spin glasses. In Miguel Rubí and Conrado Pérez-Vicente, editors, *Complex Behaviour of Glassy Systems*, pages 184–219, Berlin, Heidelberg, 1997. Springer Berlin Heidelberg.

[87] F. Lefloch, J. Hammann, M. Ocio, and E. Vincent. Can aging phenomena discriminate between the droplet model and a hierarchical description in spin glasses? *Europhysics Letters*, 18(7):647, apr 1992.

[88] Marc Mézard, Giorgio Parisi, and Miguel Angel Virasoro. *Spin glass theory and beyond: An Introduction to the Replica Method and Its Applications*, volume 9. World Scientific Publishing Company, 1987.

[89] Daniel S. Fisher and David A. Huse. Equilibrium behavior of the spin-glass ordered phase. *Phys. Rev. B*, 38:386–411, Jul 1988.

[90] Daniel S. Fisher and David A. Huse. Nonequilibrium dynamics of spin glasses. *Phys. Rev. B*, 38:373–385, Jul 1988.

[91] M.B. Weissman, N.E. Israeloff, and G.B. Alers. Spin-glass fluctuation statistics: mesoscopic experiments in cumn. *Journal of Magnetism and Magnetic Materials*, 114(1):87–130, 1992.

[92] Viktor Stepanovich Dotsenko. Physics of the spin-glass state. *Uspekhi Fizicheskikh Nauk*, 163(6):1–37, 1993.

[93] David Sherrington and Scott Kirkpatrick. Solvable model of a spin-glass. *Phys. Rev. Lett.*, 35:1792–1796, Dec 1975.

[94] B. I. Halperin. The hunt for anyon superconductivity. In Yasuhiro Iye and Hiroshi Yasuoka, editors, *The Physics and Chemistry of Oxide Superconductors*, pages 439–450, Berlin, Heidelberg, 1992. Springer Berlin Heidelberg.

[95] Pieter M Oppeneer. *Theory of the magneto-optical Kerr effect in ferromagnetic compounds*. Habilitation thesis, Institut für Theoretische Physik Technische Universität Dresden, 1999.

[96] Kyuho Lee, Bai Yang Wang, Motoki Osada, Berit H. Goodge, Tiffany C. Wang, Yonghun Lee, Shannon Harvey, Woo Jin Kim, Yijun Yu, Chaitanya Murthy, Srinivas Raghu, Lena F. Kourkoutis, and Harold Y. Hwang. Linear-in-temperature resistivity for optimally superconducting (nd,sr)nio2. *Nature*, 619(7969):288–292, Jul 2023.

[97] Xiaolin Ren, Jiarui Li, Wei-Chih Chen, Qiang Gao, Joshua J Sanchez, Jordyn Hales, Hailan Luo, Fanny Rodolakis, Jessica L McChesney, Tao Xiang, et al. Possible strain-induced enhancement of the superconducting onset transition temperature in infinite-layer nickelates. *Communications Physics*, 6(1):341, 2023.

[98] Kyuho Lee, Berit H. Goodge, Danfeng Li, Motoki Osada, Bai Yang Wang, Yi Cui, Lena F. Kourkoutis, and Harold Y. Hwang. Aspects of the synthesis of thin film superconducting infinite-layer nickelates. *APL Materials*, 8(4):041107, 04 2020.

[99] Qiang Gao, Shiyu Fan, Qisi Wang, Jiarui Li, Xiaolin Ren, Izabela Biało, Annabella Drewanowski, Pascal Rothenbühler, Jaewon Choi, Ronny Sutarto, et al. Magnetic excitations in strained infinite-layer nickelate prnio2 films. *Nature Communications*, 15(1):5576, 2024.

[100] K.H.J. Buschow. Chapter 5 magneto-optical properties of alloys and intermetallic compounds. In *Handbook of Ferromagnetic Materials*, volume 4 of *Handbook of Ferromagnetic Materials*, pages 493–595. Elsevier, 1988.

[101] R. D. Gonzalez Betancourt, J. Zubáč, R. Gonzalez-Hernandez, K. Geishendorf, Z. Šobáň, G. Springholz, K. Olejník, L. Šmejkal, J. Sinova, T. Jungwirth, S. T. B. Goennenwein, A. Thomas, H. Reichlová, J. Železný, and D. Kriegner. Spontaneous anomalous hall effect arising from an unconventional compensated magnetic phase in a semiconductor. *Phys. Rev. Lett.*, 130:036702, Jan 2023.

[102] Xiaoxiang Zhou, Yongkai Li, Xinwei Fan, Jiahao Hao, Yaomin Dai, Zhiwei Wang, Yugui Yao, and Hai-Hu Wen. Origin of charge density wave in the kagome metal csv_3sb_5 as revealed by optical spectroscopy. *Phys. Rev. B*, 104:L041101, Jul 2021.

[103] E. Uykur, B. R. Ortiz, O. Iakutkina, M. Wenzel, S. D. Wilson, M. Dressel, and A. A. Tsirlin. Low-energy optical properties of the nonmagnetic kagomé metal CsV_3Sb_5. *Phys. Rev. B*, 104:045130, Jul 2021.

[104] Qinwen Deng, Zhuoliang Ni, Brenden Ortiz, Stephen Wilson, Binghai Yan, Leon Balents, and Liang Wu. Evidence of time-reversal and rotational symmetry breaking in the charge density wave states in kagome superconductors. In *APS March Meeting Abstracts*, volume 2024, pages S07–001, 2024.

[105] K. B. Lyons, J. Kwo, J. F. Dillon, G. P. Espinosa, M. McGlashan-Powell, A. P. Ramirez, and L. F. Schneemeyer. Search for circular dichroism in high-t_c superconductors. *Phys. Rev. Lett.*, 64:2949–2952, Jun 1990.

[106] Taylor W. Lawrence, A. Szöke, and R. B. Laughlin. Absence of circular dichroism in high-temperature superconductors. *Phys. Rev. Lett.*, 69:1439–1442, Aug 1992.

[107] L. A. Falkovsky and A. A. Varlamov. Space-time dispersion of graphene conductivity. *The European Physical Journal B*, 56:281–284, 2007.

[108] A. B. Kuzmenko, E. van Heumen, F. Carbone, and D. van der Marel. Universal optical conductance of graphite. *Phys. Rev. Lett.*, 100:117401, Mar 2008.

[109] L. A. Falkovsky. Optical properties of graphene. *Journal of Physics: Conference Series*, 129(1):012004, oct 2008.